

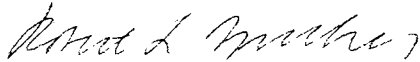
# **A Mixed-Penalty Contact Finite Element Formulation for Biphasic Soft Tissues**

by

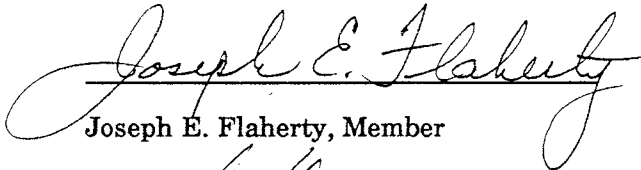
**Peter S. Donzelli**

A Thesis Submitted to the Graduate  
Faculty of Rensselaer Polytechnic Institute  
In Partial Fulfillment of the  
Requirements of the Degree of  
**DOCTOR OF PHILOSOPHY**  
Major Subject: Mechanical Engineering

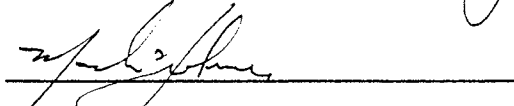
Approved by the  
Examining Committee:



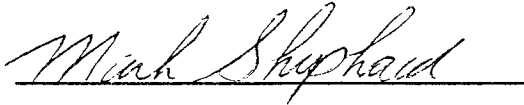
Robert L. Spilker, Thesis Advisor



Joseph E. Flaherty, Member



Mark H. Holmes, Member



Mark S. Shephard, Member

Rensselaer Polytechnic Institute

Troy, New York

April 1995

(for Graduation May 1995)

© Copyright 1995

by

Peter S. Donzelli

All Rights Reserved

# Table of Contents

	Page
List of Tables.....	viii
List of Figures.....	ix
Acknowledgments.....	xiv
Abstract .....	xvi
Chapter I: Introduction.....	1
Prologue.....	1
Tissue Modeling .....	2
Cartilage Structure.....	3
Mechanical Models.....	4
Tissue Contact Modeling.....	6
Numerical Solution Procedures.....	8
The Finite Element Method.....	9
Contact Problems.....	10
Summary .....	13
Chapter II: Governing Equations for Multi-Body Biphasic Contact .....	16

Introduction.....	16
The Biphasic Theory.....	16
Derivation of the Equations.....	19
Continuity of Solid Displacement.....	20
Balance of Mass.....	23
Balance of Linear Momentum .....	26
Balance of Energy .....	27
Constitutive Assumptions and the Entropy Inequality .....	28
Reduction to Frictionless Contact .....	29
Summary .....	32
<b>Chapter III: Alternate Contact Formulations .....</b>	<b>36</b>
Introduction.....	36
Methods of Applying Constraints .....	37
Penalty Methods.....	37
Lagrange Multipliers .....	40
Augmented Lagrangians.....	43
Finite Element Equations for Elastic Contact .....	46

<b>Chapter V: Contact Surface Calculations .....</b>	<b>81</b>
Introduction.....	81
Closest Point Projection .....	82
Surface Discretization.....	86
Detecting Contact or Release.....	88
Element Matrix Calculations .....	90
Contact Iterations .....	93
<b>Chapter VI: Two Dimensional Examples .....</b>	<b>95</b>
Introduction.....	95
Validation Examples.....	95
Unconfined Compression.....	96
Hertz Contact .....	102
Biphasic Indentation .....	108
Clinical Demonstrations .....	111
Gleno-Humeral Contact.....	111
Tibio-Femoral Contact.....	116
<b>Chapter VII: Summary and Concluding Remarks.....</b>	<b>123</b>

Penalty Element .....	47
Lagrange Multiplier Element.....	49
Augmented Lagrangian Element .....	50
Hybrid Contact Elements .....	52
<b>Selection of the Biphasic Element .....</b>	<b>53</b>
Selecting the Element Formulation.....	53
Selecting the Contact Treatment .....	56
<b>Chapter IV: The Mixed-Penalty Lagrange Multiplier Formulation .....</b>	<b>58</b>
<b>Introduction.....</b>	<b>58</b>
<b>Weighted Residual Statement.....</b>	<b>58</b>
Preliminaries.....	59
Choice of Trial and Test Spaces .....	61
Development of the Weak Form.....	62
<b>Finite Element Matrix Equations.....</b>	<b>63</b>
Element Interpolations.....	66
Element Matrices .....	72
Quadratic Velocity Triangle .....	78

Summary .....	123
Comments on Element Performance .....	124
Future Directions .....	127
References.....	130
Appendix A: Implicit Time Integration.....	154
Appendix B: Symbolic Elastic Contact Calculations .....	163





# List of Tables

	Page
Table 6.1. Number of active contactor segments at each iteration of the contact surface for a range of settings of the tolerance parameter.....	106
Table 6.2. Average material and geometric properties for human cartilage in an axisymmetric model of the gleno-humeral joint, from [133].....	112
Table 6.3. Geometric parameters for two axisymmetric models of three-body meniscus-femur-tibia contact. Values are given in mm.....	119



# List of Figures

	Page
Fig. 2.1 Spatial and material domains for a biphasic continuum. The spatial and material coordinate systems are chosen to coincide.....	18
Fig. 2.2 Spatial domain for the derivation of multi-body biphasic contact equations.....	20
Fig. 2.3 Convention for the definition of the normal and tangent vectors at a point on the contact surface.....	21
Fig. 2.4 Decomposition of the traction vector at a point on Body A with respect to the normal and tangent vectors of Body A.....	22
Fig. 3.1 Solution to a single-variable constrained problem by the penalty method.....	39
Fig. 3.2 Penalty functional for a single-variable constrained problem and two different values of the penalty parameter, $\beta$ .....	40
Fig. 3.3 Lagrange functional, $J_L$ , plotted in the region of the solution.....	42
Fig. 3.4 Convergence of the augmented Lagrange functional with iteration for a range of penalties.....	44
Fig. 3.5 Convergence of the augmented Lagrange multiplier with iteration for a range of penalties.....	45
Fig. 5.1. Definition of the gap function and its sign on a contactor surface.....	83

Fig 5.2. Finite element mesh of four triangles with the topological entities identified. A sample of the upward and downward pointers for edges and vertices is given at right.....	85
Fig. 5.3. Section of a finite element mesh composed of three model regions. An appropriate selection of the contactor and target surfaces is indicated. ....	87
Fig. 5.4. Section of a finite element mesh indicating the projection of quadrature points to the target surface. A contactor segment in $\Omega^1$ is coupled to multiple target segments in different regions.....	91
Fig. 5.5. Algorithm for contact surface iterations.....	94
Fig. 6.1. Geometry and boundary conditions for the frictionless unconfined compression problem.....	97
Fig. 6.2. Finite element mesh and boundary conditions for the unconfined compression problem.....	97
Fig. 6.3. Radial solid and fluid velocities at the half-height, point 'P', for the unconfined compression test. ....	98
Fig. 6.4. Axial solid and fluid velocities along the contact surface at $t = 50s$ for the unconfined compression test. ....	99
Fig. 6.5. Solid stress and fluid pressure along the contact surface at $t = 50s$ for the unconfined compression test. ....	100
Fig. 6.6. Solid and fluid normal traction along the contact surface compared with the multipliers at $t = 50s$ for the unconfined compression test.....	100

Fig. 6.7. Solid stress, fluid stress and pressure along the contact surface at $t = 50s$ for the unconfined compression test with discontinuous volume fraction. ....	102
Fig. 6.8. Model geometry for the plane strain Hertz contact problem. ....	103
Fig. 6.9. Finite element mesh for the plane strain Hertz contact problem.....	103
Fig. 6.10. Axial solid stress at several iterations of the contact surface for a total load of 4 N in the plane strain Hertz contact problem.....	104
Fig. 6.11. Deformed surface geometry for a total load of 4 N in the plane strain Hertz contact problem.....	106
Fig. 6.12. Axial solid stress distributions for several applied loads in the plane strain Hertz contact problem.....	107
Fig. 6.13. Normal traction distributions for biphasic indentation after 100 seconds of creep. Lines are the integral transform solution and symbols are the finite element result. ....	109
Fig. 6.14. Deformed surface for biphasic indentation after 100 seconds of creep. ....	109
Fig. 6.15. Shaded contour of maximum principal stress in kPa for biphasic indentation. Solutions are on a 5 $\times$ deformed mesh after 100 seconds of creep. The relative velocity field is indicated by arrows.....	110
Fig 6.16. Model geometry and finite element mesh for the axisymmetric GHJ. ....	112
Fig. 6.17. Normal tractions verses radial coordinate after one second of creep for points along the glenoid surface.....	113

Fig. 6.18. Shaded contour of the maximum principal elastic stress in kPa in the GHJ after one second of creep. Magnitude and direction of the in-plane principal stresses indicated by arrows.....	114
Fig. 6.19. Shaded contour of the minimum principal elastic stress in kPa in the GHJ after one second of creep.....	115
Fig. 6.20. Tibial surface of the knee showing the menisci and several major ligaments, from [51]. .....	116
Fig. 6.21. Parametric geometry for axisymmetric, three-body meniscus-femur-tibia contact.....	118
Fig. 6.22. Axial compressive strain in percent at $t = 1s$ for axisymmetric, three-body meniscus-femur-tibia contact.....	120
Fig. 6.23. Fluid pressure in kPa at $t = 1s$ for axisymmetric, three-body meniscus-femur-tibia contact.....	121
Fig. A.1. Amplification factor for the generalized trapezoidal rule for various values of the integration parameter, $\omega$ (reproduced from [66]).....	155
Fig. A.2. Illustration of a rigid block under displacement control penetrating a deformable surface. ....	157
Fig. A.3. Velocity along surface A (Eq. (A.5)) for different values of the integration parameter.....	159
Fig. A.4. Normal solid velocity along the contact surface for the biphasic indentation problem: (a) $t = \Delta t$ , $\omega = 1.0$ , (b) $t = 2\Delta t$ , $\omega = 1.0$ , (c) $t = 2\Delta t$ , $\omega = 0.5$ .....	161

Fig. B.1. Node-to-node (left) and node-to-element (right) meshes used in MAPLE testing of contact elements.....	164
Fig. B.2. Normal tractions and Lagrange multipliers for a linearly varying displacement applied to the node-to-node mesh of six-node triangles.....	166
Fig. B.3. Normal tractions and Lagrange multipliers for a linear displacement applied to the node-to-element mesh of six-node triangles.....	167





# Acknowledgments

I still find it hard to believe that I have come to the point where I can write this page. My life has been a continuous educational process to this point, and I can say with complete honesty that I have enjoyed every aspect of that education, both inside and outside of the classroom. There are many people who should receive credit here for their contributions to my education. In the last six years, however, it has been my advisor, Bob Spilker, who has given me the most encouragement. Beyond the immediate research goals, he is truly interested in preparing his students for their careers as researchers and educators, and is willing to devote that extra effort to realize that goal. My work is multidisciplinary and I am grateful to my other committee members for their interest in this project. Joe Flaherty in Computer Science, Mark Holmes in Applied Mathematics and Mark Shephard in Engineering have always been available for discussion and have provided invaluable advice during the course of this research. I also wish to thank the faculty and students at the Orthopaedics Research Laboratory at Columbia University for their time and effort in defining clinical problems to solve and in correlating our results to theirs.

I am lucky to have had a work environment that is both academically stimulating and fun. Francis Suh, Mark Vermilyea and Bob Chan have long since completed their work at RPI, but I continue to enjoy their friendship. Their patience in answering the questions of a new graduate student was admirable; I hope that has rubbed off on me. Edgard Almeida, Sharon Tabolt and Bill Dunbar are always willing to listen to my questions or discuss the subtleties of computational biomechanics. It is through these interactions that I have learned the most while at RPI.

I owe my family a tremendous thanks. Their support and love has allowed me to

reach this point. This degree is due as much to their efforts over the last 28 years as to my own. And, of course, I must also thank Michelle. Her friendship has made my life much more enjoyable. Having a partner with whom I can share my work and my leisure has been wonderful.

Support of the National Science Foundation (ECS-9024235 and ASC-9318184) and the National Institute of Health (AR-38728) is gratefully acknowledged.

# Abstract

As a key step in developing a complete computational model of diarthrodial joint mechanics, this thesis presents a finite element formulation and implementation for contact between hydrated soft tissues. The biphasic theory of Mow and co-workers is chosen as the continuum model which governs cartilage mechanics. Boundary conditions for contact surfaces have been developed by Hou *et al.* by considering a surface of material discontinuity within the continuum. These differential equations and boundary conditions, together with inequality constraints to define the contact surface, form the strong form of the problem. Currently, a fully linear form of the biphasic theory is used and frictionless contact is assumed.

A weighted residual approach is used to develop a form of the equations suitable for numerical approximation. A penalty form of the mixture continuity relation, following Spilker and Maxian, and the momentum equations for each phase are introduced into the weighted residual. Lagrange multipliers are defined on the contact surface and reflect the appropriate continuity of solid and fluid normal traction. Four equations for the multipliers and two expressing kinematic continuity are added to the weighted residual. Standard procedures result in a weak form of the weighted residual, which is then approximated by the finite element method. Quadratic interpolations are selected for velocity and displacement within an element, as well as for the multipliers on the contact surface. A linear interpolation for pressure, independent from element to element, is used.

Part of the solution procedure is to determine the correct contact surface; two tools are required to accomplish this in the finite element setting. First is an algorithm which

discretizes the contact surface and provides a coordinate system in which to perform the required surface integrals. Second is an iterative scheme which recognizes regions of the contact surface exhibiting non-physical behaviour, and modifies the surface definition. These algorithms have been evaluated only with the present two-dimensional element, but are readily extensible to three dimensions. Two types of example problems are presented: those that validate the formulation of the element and those that demonstrate its applicability to clinically relevant geometries.

# Chapter I: Introduction

## Prologue

There is no machine that can compare to the human body. As a mechanical engineer, it is disheartening to realize that there is no man-made pump that can function continuously for eight decades without maintenance, as does the human heart. Or that today's machines can not provide the amazing degree of motor control that allows our musculoskeletal system to perform complex tasks. Even modern electronics can not simulate the feedback control mechanisms to control grip strength or walking. When we look to each component of the body though, we recognize the most basic mechanical or electrical systems, evolved to perform its respective task with the utmost efficiency.

There are instances where the body fails, however, and we turn to technology to return an individual to a functional lifestyle. Successful designs are available to replace the heart, limbs and diarthrodial joints. For engineers to create these designs, they must first understand the biological counterpart, and how that normally functions in the body. Recently, many researchers have turned to computational models to gain a greater understanding of the biomechanics of the human body. These models can provide a wealth of information that can not be measured with experiments. In addition, it is often more practical to do parametric studies with computational models than with animal specimens.

With our population steadily aging, more and more adults are afflicted with osteoarthritis (OA). This is a degenerative disease affecting the articular cartilage in joints. When functioning normally, this cartilage provides a nearly frictionless bearing surface for the articulating bones [85,89]. As OA progresses, the cartilage changes

mechanically, biochemically and structurally [93], compromising its performance. Overall, its causes are not fully understood, but hypothesis have been put forth suggesting that repeated stressing of the cartilage can eventually lead to its degeneration [102]. In severe cases of OA, it may become necessary to replace the joint with a prosthetic to relieve the intense pain that is caused by normal movements.

There are two problems posed to the engineers who study joint biomechanics. First is to understand cartilage as an engineering material, and second is to use that knowledge in designing a device which replicates the function of a normal joint. This research is concerned with the first point; specifically with understanding the mechanical response of articular cartilage layers in contact. Numerical simulation of joint biomechanics is one tool that can be used to evaluate cartilage mechanics. This numerical simulation has two parts: the mathematical model of articular cartilage and the numerical solution of the complex boundary value problem resulting from the mathematical model.

## **Tissue Modeling**

It is not just the modern engineer who is drawn to studying the body. Aristotle, daVinci and Galileo have written on such topics as the anatomy of muscles and their relation to motion, and on the strength of bones [10,86]. It has not been until this century, though, that researchers have tried to develop mathematical models for tissue mechanics. Some of the first tissues studied were muscles and blood vessels, as described in the review by Fung [47]. More recently, attention has turned to modeling articular cartilage. Researchers recognized very early that articular cartilage played an important role in joint lubrication [32,92]. From there it became important to quantify the material properties, and describe the structure and mechanical response of cartilage.

## Cartilage Structure

Articular cartilage is a smooth, white substance lining the contacting surfaces of bones. It is typically rather thin, with up to about six millimeters lining some human joints [14,135]. Cartilage is composed primarily of water, collagen, proteoglycan molecules, cells and ions. As with most biologic materials, there is a high variability in the relative percentages of the constituents among different subjects, joints or sites within a given joint. In addition the material shows variation in composition through its thickness, which, when cartilage is viewed as an engineering material, optimize it for its intended function.

Up to 85% of the wet weight of cartilage is water [84], though the material has the general appearance of a solid. This interstitial fluid is the medium in which charged ions are suspended, and whose flow through the tissue provides nutrients to cells [95]. Much of the water is electrochemically bound to high-molecular-weight proteoglycans, and is not free to flow within cartilage. The charged nature of cartilage plays significant roles in its function, and has motivated the use of mathematical models to describe these effects [79].

The second major constituent is collagen fibers, ranging between 60 and 70% of the dry weight of cartilage [4,5]. There are four readily recognized zones of collagen fiber orientation: the surface, middle, deep and calcified zones [100]. In the surface zone fibers are oriented tangent to the surface, in a weave pattern. The middle zone of cartilage has no preferred orientation of the fibers. Toward the bottom layers, fibers begin to orient themselves normal to the subchondral bone, and to form larger bundles. Collagen fibers in the calcified zone provide the attachment mechanism for cartilage to bone [95,162]. Other hydrated soft tissues, such as meniscus, have different fiber orientations. The same surface zone fiber network is observed, but the central core of meniscus has predominantly

radial bundles of fibers. These have a significant stiffening effect on the meniscus *in vivo* [1,101].

Proteoglycans (PG's) make up the majority of the remaining cartilage structure, from 20 to 30% of the dry weight [103]. These are very large protein aggregates, bonded to an hyaluronic acid core [54]. The molecules have an overall negative charge due to the fixed charges of carboxyl and sulfate groups on the protein chains. Also, in cartilage PG's are intertwined with themselves and the collagen fibers [103]. These charges have the effect of trapping some of the interstitial water within the coiled PG's, and of causing a Donnan osmotic swelling pressure [79]. As one changes the ionic concentration of the interstitial fluid the density of unbalanced fixed charges changes, and the cartilage responds with changes in the swelling pressure.

### **Mechanical Models**

The first cartilage experiments showed that the tissue's response is time dependent. In observing the recovery of cartilage after indentation, Elmore and co-workers deduced that fluid exuded during the creep phase is later imbibed through the surface [44]. Despite these observations, the first attempts to quantify a 'compressive modulus' for cartilage were based on elastic theories. Using the indentation test and Hertz's theory for contact of infinite elastic bodies, Hirsch [60] defined a Young's modulus for cartilage. Later work by Sokoloff [132] assumed the cartilage to be incompressible, and used the elastic punch solution to determine a Young's modulus. Recognizing the time-dependent nature of the indentation, both an instantaneous and an equilibrium value of the modulus were reported. To account for the finite thickness of the cartilage, Hayes *et al.* [55] developed an integral solution to the indentation of a thin cartilage layer bonded to subchondral bone.



The next major class of cartilage models assumed the material to be a viscoelastic solid, which could account for the observed creep response. One of the first viscoelastic models was proposed by Hayes and Mockros [56]. Using spring and dashpot models, they were able to determine material constants from indentation data. The quasi-linear viscoelastic theory was successful for describing cartilage behaviour, as well as for other tissues [48,163]. Some discrepancies were reported, however, when high-strain-rate tests were performed.

While many researchers recognized the importance of the internal fluid flow in the performance of articular cartilage, they were slow to incorporate this behaviour into a continuum model for tissue mechanics. A theory for soft hydrated tissues was presented by Torzilli and Mow [151,152] and was based on an extended Hamilton's Principle. Expressions for the internal and kinetic energy and conservative and non-conservative forces were developed for the tissue, as well as constraints on the total mass and entropy. Governing equations were developed from a variation of the Hamiltonian. In a later model, following principles from the analysis of mixtures [29,36], Mow and co-workers were able to develop the Biphasic Theory. A continuum description of the tissue was used for this formulation, and refinements were made to the previous mass and entropy constraints before the theory was published by Mow and Lai [98] and Mow *et al.* [96].

Since then, the biphasic theory has been widely accepted as a means to model cartilage, and has been adopted by many other researchers in biomechanics (*i.e.* [15,30,46]). The theory has also been extended to include the nonlinearities observed in tissue mechanics, including finite deformation [78,97], strain-dependent permeability [63,80,81], transversely hyperelastic solid phase mechanics [34] or viscoelastic solid phase mechanics [87,119]. Based on the biochemical composition of cartilage, it is apparent that

the charged macromolecules contribute significantly to the deformational behaviour of the tissue. Recently, Lai *et al.* have published their Triphasic Theory [79] which treats fixed charges in the tissue as a third phase in the mixture.

## Tissue Contact Modeling

Numerous models to describe contact of articular cartilage have been developed, but each has either restricted attention to elastic models, or has not been of the general applicability of the finite element formulation presented here. Among the many finite element formulations for joint contact is the work by Schreppers *et al.* [118] and Tissakht, Ahmed and co-workers [148-150]. The first group used a commercial finite element program to solve quasi-static, elastic models of axisymmetric femur-meniscus-tibia contact. Parametric variations were conducted to evaluate the effects of cartilage stiffness, cartilage surface curvature and fiber reinforcement in the meniscus. They recognized that fluid flow within the cartilage would play an important role for dynamic simulations. Tissakht and Ahmed developed three-dimensional, transversely isotropic, elastic finite element models of the meniscus to investigate the effects of tibial rotation [149]. Loading was distributed over the meniscal surface in accordance with measured pressure distributions [3]. Later a nonlinear, axisymmetric model was used, including transverse isotropy of the meniscus and treating the material as incompressible [148]. In a further refinement of the model, comparisons were made between isotropic, transversely isotropic, composite and poroelastic (both isotropic and transversely isotropic) representations of the meniscus [150]. These models treat cartilage as rigid and do not address its elastic or biphasic properties. They report significant variation in the solution depending on which model was used, but do not comment on the importance of the cartilage layers to fluid flow or the overall response.

Some researchers have used analytic methods to develop models for elastic articular contact. Eberhardt and co-workers have a small strain model of elastic spheres contacting to model cartilage lining the ends of bones [41-43]. Solutions are based on elasticity theory and result in integral equations which are solved numerically. The authors predict some stress behaviour which is consistent with failure modes in osteoarthritis, while other results contradict experimental observations. They conclude that nonlinear effects must be included, as well as inhomogeneity and interstitial fluid in the tissue. Blankevoort *et al.* have a unique model derived from geometry, measured through stereophotogrammetry, and measured kinematics and kinetics of the knee [27]. A mathematical simulation of the joint's motion was conducted where ligaments were modeled with nonlinear properties, and cartilage was variously described as rigid, linear elastic or nonlinear elastic. The authors found that different material models for cartilage did not affect joint kinematics, though differences in joint laxity were observed.

Hale, Rudert and Brown [53] augmented the linear biphasic penalty element developed by Spilker *et al.* [143] with algorithms to model contact by a rigid, impermeable, spherical indenter under displacement control. This amounts to enforcing the correct time-dependent velocity boundary conditions on an increasing area of the tissue surface. They assumed perfectly adhesive contact between the tissue and indenter. Results compared favorably with experiments, and the code was used with a least-squares algorithm to determine material properties. Shrive *et al.* presented solutions from a commercial finite element program used to model ball-in-socket contact of poroelastic materials [124]. The authors used a free-draining, or zero pressure, boundary condition outside the region of contact, but used an impermeable condition within the contact zone. This would preclude fluid transport across the contact surface and hydrodynamic lubrication [40,99].

Hou *et al.* used their biphasic contact boundary conditions to develop an analytic model of squeeze-film lubrication [65]. They determined that when load is transferred to a biphasic material through a fluid film, it is distributed between the phases according to the volume fractions. Recently Ateshian and co-workers have published analytic solutions to frictionless biphasic contact problems. An asymptotic solution to the problem of a rigid, impermeable sphere indenting a thin biphasic layer was presented in 1994 [13]. The ratio of tissue thickness to contact area was used as a small parameter for the asymptotic expansion. Results showed that radial deformation was significantly greater than axial deformation, and that pressure dominated elastic stress. More recently, a solution based on an integral transform method has been developed [73]. This has the same qualitative results, though it is not subject to the small parameter constraint of the previous work. Steady state solutions have also been developed for an impermeable sphere translating with constant velocity across a biphasic layer [11]. These results are of particular importance in understanding lubrication problems.

## Numerical Solution Procedures

As the biphasic theory matures, it is applied to more and more complex problems. There are only limited cases where the coupled, nonlinear differential equations of the theory can be solved analytically, for example confined [96] and unconfined [8] compression and indentation [88]. While there is tremendous insight to be gained into cartilage mechanics from these analytic solutions, it is generally impossible to analyze the physiological geometries presented by diarthrodial joints. This has lead researchers to numerical solution techniques for partial differential equations, and in particular to the finite element method.

## The Finite Element Method

The finite element method is a robust technique that can be applied to any system of differential equations. It is premised on defining the domain of interest as the union of a finite number of geometrically regular elements, characterized by some length,  $h$ . Within each element, a polynomial interpolation of degree  $p$  is assumed for the unknown solution function. This interpolation is defined as the sum of unknown coefficients multiplied by corresponding shape functions, and then substituted into a weak form derived from the governing equations. Once the appropriate continuity is satisfied between elements by an assembly operation, an algebraic system of equations results for the unknown coefficients. The finite element solution will be the projection of the true solution onto the space of polynomials of degree  $p$ . Furthermore, the method guarantees, with some mathematical restrictions, that as  $h \rightarrow 0$  or  $p \rightarrow \infty$  the finite element solution will converge to the true solution. Details about all aspects of the method are available, for example, in the texts by Zienkiewicz and Taylor [165], Hughes [66] or Strang and Fix [144].

Finite element formulations for mixtures began in the field of soil mechanics where Biot's poroelastic theory [25,26] is used to describe the response. Ghaboussi and Wilson developed a formulation for the dynamic loading of soils [50]. Simon and co-workers have been concerned with different aspects of the numerical simulation of the dynamic response of soils [129-131] and soft tissues [127,128]. They have evaluated a number of displacement-based and mixed formulations, and have looked at higher-order finite element interpolations. Prevost has developed nonlinear finite element formulations for the dynamic response of soils also based on Biot's poroelastic theory [115,116].

Oomens and co-workers have applied mixture theories to the mechanics of skin

[111,112]. Wayne *et al.* developed a rectangular displacement-pressure element for the biphasic theory that included material nonlinearities [159]. This was applied to problems in the mechanics of cartilage healing processes. Suh *et al.* developed a nonlinear biphasic element that included finite deformation, strain-dependent permeability and an hyperelastic solid phase constitutive law [146]. This is a four-node rectangular element which uses a penalty approach to treat the incompressibility constraint. Spilker and Maxian developed a mixed-penalty element for two-dimensional, linear analysis with a six node triangle [139]. Vermilyea and Spilker used the hybrid approach to develop two- and three-dimensional simplex elements for the biphasic theory [156]. These elements do not require a user-specified penalty parameter to enforce the incompressibility constraint. Donzelli and co-workers extended the mixed-penalty formulation to include an  $h$ -adaptive mesh enrichment scheme [39]. In any physiologically relevant geometry automatic control of the discretization error will be essential, as is not possible to anticipate *a priori* the location of spatial gradients. Almeida and Spilker have developed nonlinear, three-dimensional elements based on the mixed-penalty and velocity-pressure formulations [7]. These elements include a transversely isotropic solid phase constitutive law, which admits anisotropic behaviour in tension and compression [6].

## Contact Problems

Contact finite element formulations for linearly elastic and nonlinear materials, with and without friction, have been in use for nearly as long as the finite element method itself. They fall into the more general category of constraints applied to the finite element method, such as the constrained medial problems of incompressible solid or fluid mechanics. The text by Johnson [72] gives an extensive treatment of the contact problem in solid mechanics. Aspects of the numerical solution of contact problems by the finite

element method is the subject the book by Kikuchi and Oden [75]. They give a complete discussion of the mathematical formalism behind contact finite elements, which leads them to a discussion of error estimates and the Babuska-Brezzi conditions for constrained problems.

Kubomura [76] developed a contact finite element by introducing displacement and traction constraints into the hybrid stress functional for geometrically nonlinear elastic materials. A contact element with traction degrees of freedom was developed and utilized to perform integrals over an assumed contact surface. Iterative procedures to determine the contact region and friction conditions (*i.e.* sliding or sticking friction) were necessary. Other authors have investigated contact using complementary principles as well. Tseng [154] used a mixed element with two displacements and three stresses at each node such that the contact conditions can be approximated directly. Kwak [77] formulated a three-dimensional, nonlinear complementary problem for frictional contact and an incremental analysis.

Frictional node-to-node contact was considered by Gaertner [49]. Triangular elements with nodal unknowns corresponding to tangential and normal displacement, rigid rotation, tangential strain, and normal and tangential stress were developed. Desai and co-workers [38] developed thin-layer elements that incorporated observed frictional behaviour to analyze contact problems in geomechanics. This element, whose constitutive law is written in terms of incremental quantities, eliminates the need for explicit constraints on the finite element equations, as they are included in the stress-strain law. An  $n$ -body contact algorithm was developed by Cheng [33] where impenetrability constraints are handled via a penalty parameter and static condensation is applied to eliminate all but the displacement degrees of freedom on the interfaces.

Contact finite element formulations for metal forming [21,28] often involve an elastic workpiece and a rigid die. In these cases contactor nodes are constrained to be on a known surface (the die) and the process of determining the extent of contact is somewhat simplified. Dynamic contact, or contact-impact, has been treated by several authors, including Wriggers [164], Ayari [17] and Belytschko [24]. An added effort is made to develop efficient computational algorithms in these strongly nonlinear, time-dependent problems. Wriggers proposes a frictional law from which a matrix form of the virtual work of the contact forces can be added directly to the finite element equations. This leads to a contact formulation in terms of displacement only, and no explicit constraint equations are introduced. The authors note that for some frictional laws, the method can be identified as a penalty method. Ayari used 'fictitious forces' to counteract any mutual penetration between elements on the contact surface and Belytschko enforces impenetrability by examining the radii of 'pinballs' inscribed in the finite elements along with either penalty functions or Lagrange multipliers. He also notes that for an explicit central difference integration of the semi-discretized equations, the contact surface and Lagrange multipliers (interface tractions) can be determined without iteration.

Since the contact problem is a surface phenomenon, some researchers have turned to the boundary element method [147] or mixed FEM-BEM procedures [158]. The former authors claim a savings in computation time as only the boundary of the domain need be discretized, and the size of the resulting flexibility matrix equations are dependent only on the number of nodes in contact. In addition, iterations of the boundary element analysis and contact analysis are not directly coupled, *i.e.*, the two may be performed in succession. The latter author uses fundamental surface integral solutions in the region of contact, matched with finite element solutions away from this region. This is based on the premise that the finite element solution is most accurate away from the point of loading, and cannot



capture the gradients present in that region.

Recently, researchers have embraced the method of perturbed or augmented Lagrangians as a computationally efficient means to enforce constraints on the finite element method. Weiss *et al.* [161] have developed an element for incompressible elasticity that enforces the constraint by means of an augmented Lagrangian. Simo and co-workers have applied the method to contact formulations. They first present the method as a way to regularize the ill-conditioned system that results from a Lagrange multiplier approach [126]. In the same publication, they present a unique treatment of the contact surface kinematics by contact *segments*. Simo and Laursen have extended that formulation to include frictional effects on the contact surface [125]. Laursen and Oancea have indicated how the convergence characteristics of the augmented Lagrangian formulation render it superior to either penalty methods or Lagrange multipliers [82]. The advantage is that with finite penalties, there is nearly exact satisfaction of the constraint. On the other hand, it is not necessary to optimally choose the penalty to guarantee convergence. Heegaard has developed a large displacement, frictional sliding contact element for elastic materials using the augmented Lagrangian approach [57,58]. He has applied this element to the problem of patello-femoral contact, and has made comparisons of the numerical procedure to experimental results.

## Summary

Chapter II gives a summary presentation of the biphasic theory and the derivation of the governing equations and contact continuity relations. Derivations are carried out under the assumption of small deformations and linear constitutive laws. The contact continuity relations are then manipulated to introduce the assumption of frictionless

contact.

Chapter III presents alternate means of enforcing constraint equations with the finite element method. Often this subject is treated from the viewpoint of variational calculus and energy principles. For the biphasic equations, weighted residual methods are more appropriate as a means of generating the finite element equations, and the differences between the two are presented. Before a particular method is selected to enforce the contact conditions, finite element equations for elastic contact elements are presented. Each has advantages and disadvantages, and can provide insight into the numerical performance of the biphasic contact element. Various formulations for biphasic finite elements are also evaluated to choose that which is most efficient for the present implementation.

Chapter IV contains a complete derivation of the mixed-penalty biphasic contact finite element. This element is built upon the element of Spilker and Maxian [139], and introduces contact constraints with Lagrange multiplier-like variables. The weighted residual formulation is presented, and the general form of the finite element matrices is derived. The chapter concludes by specializing the interpolations to the six-node triangle.

Contact finite element formulations are nonlinear since the surface of contact is unknown in advance. A significant part of this research is devoted to discretizing the contact surface and assessing whether points on that surface should be included in the contact calculations. An iterative procedure, which modifies the contact surface during the solution phase, is defined to determine the correct solution to this nonlinear problem. A description of these algorithms is given in Chapter V.

Results are presented in Chapter VI. Several problems with known solutions were

solved to validate the formulation. These results demonstrate that the contact continuity is properly enforced and that the discretization algorithms are robust. Demonstrations of clinically relevant problems are also presented. With only the two dimensional element implemented, only plane strain or axisymmetric problems can be solved. The glenohumeral joint and the knee joint are chosen as axisymmetric models to demonstrate the clinical applications of the biphasic contact finite element.

Chapter VII summarizes the contributions of this thesis to the field of computational biomechanics. There are, of course, many ways in which the research can be extended in the future. An indication of the necessary extensions for three-dimensional, nonlinear or sliding contact formulations is given. There is also a discussion of the range of applicability of the biphasic contact finite element.



## Chapter II: Governing Equations for Multi-Body Biphasic Contact

### Introduction

This research is based upon the biphasic theory of Mow and co-workers [96]. A fully linear form of the governing biphasic equations is used for this development, where small strains are assumed, the solid phase is governed by a linear constitutive law, tissue permeability is constant and volume fractions of the solid and fluid phase do not change with deformation. Correlations of theoretical results with one-dimensional confined compression tests suggest that these assumptions are valid in a wide range of problems, including up to nearly 30% compressive strain in the solid matrix [96].

Governing differential equations for the theory are derived from integral statements of balance of mass, momentum and energy. Contact boundary conditions are found in the same way, but with integrals performed over a volume having a surface (interface) of discontinuity, as first reported for the biphasic theory by Hou *et al.* [64]. This results in the theoretically correct statement of traction continuity and relative flow across the interface. In solving a contact problem by the finite element method the solution procedure is nonlinear, since the contact area is unknown in advance, and iterations must be performed. This is true even in the case of fully linear constitutive relations and small strains. Additional restrictions beyond the contact boundary conditions must be imposed to recover an unique solution to this nonlinear problem.

### The Biphasic Theory

In the biphasic theory for soft hydrated tissues, materials are considered to be a

continuum mixture of solid and fluid, representative of the collagen-proteoglycan matrix and interstitial water, respectively. Based on the observed structure of cartilage, several simplifying assumptions were used by Mow, *et al.* in their presentation of the theory [96]. First, both the solid and fluid phases are inert, and do not undergo any chemical changes or interactions. Each phase is considered incompressible, which gives rise to mass conservation statements for each phase, as well as for the mixture. For biological materials it is reasonable to assume isothermal deformations and no heat supply. Inertial terms are not included in this formulation and it is assumed that no energy is lost by convection across the contact surface [64].

For the binary continuum mixture, each phase simultaneously occupies the same spatial volume. As a matter of convenience the boundary of the continuum is considered to be the boundary of the solid phase, and relative flow of the fluid across that boundary is allowed. The motion of each constituent is governed by a deformation function,  $\chi$ , defined by the relation

$$\mathbf{x}^\alpha(t) = \mathbf{x}(t) = \chi^\alpha(\mathbf{X}^\alpha, t), \quad \alpha = s, f, \quad (2.1)$$

where the solid and fluid phases are indicated by the superscripts 's' or 'f', respectively,  $\mathbf{x}$  is the spatial position of both phases at time  $t$  and  $\mathbf{X}^\alpha$  are their material positions. Displacements for the particles are defined from the motion in the standard way,

$$\mathbf{u}^\alpha(t) = \mathbf{x}(t) - \mathbf{X}^\alpha, \quad \alpha = s, f. \quad (2.2)$$

These concepts are illustrated in Fig. 2.1, which follows material points  $\mathbf{X}^s$  and  $\mathbf{X}^f$  from their reference state at  $t = 0$  to their common spatial location,  $\mathbf{x}$ , at  $t > 0$ . Velocities are defined as the material time derivative of the displacement, holding the phase material position fixed.

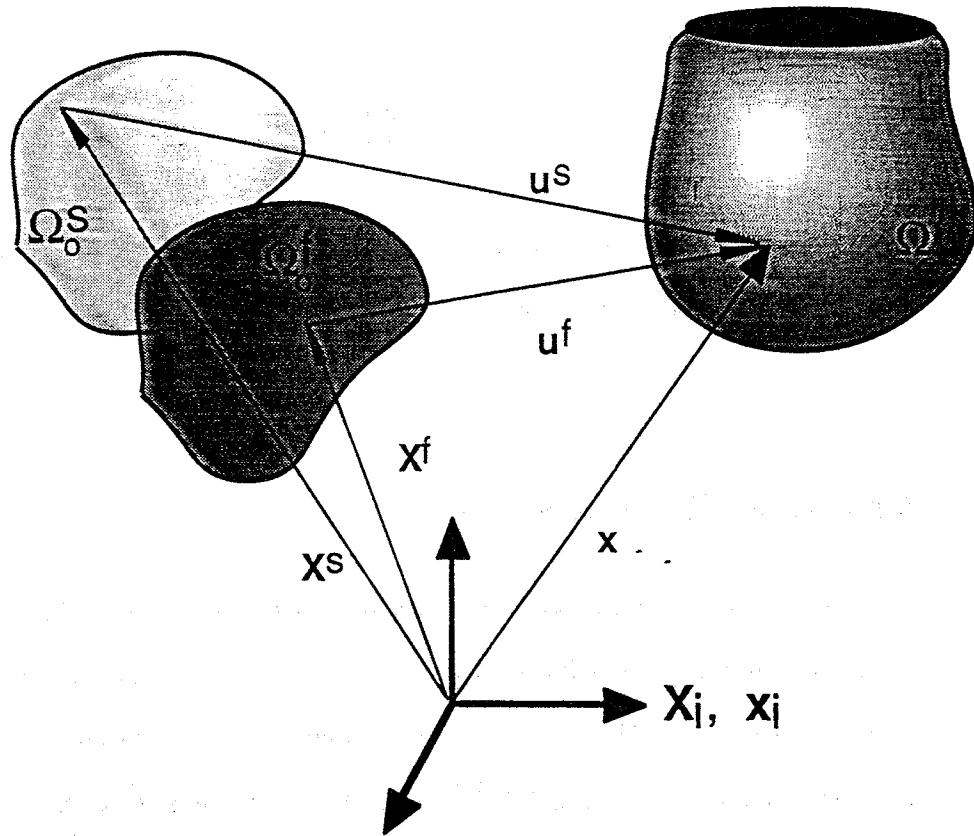


Fig. 2.1 Spatial and material domains for a biphasic continuum. The spatial and material coordinate systems are chosen to coincide.

In mixture theory, two densities can be defined for each phase, the true density and the apparent density. True density is the mass of a constituent per unit volume of that constituent,

$$\rho_T^\alpha = \frac{dm^\alpha}{dV^\alpha}, \quad \alpha = s, f, \quad (2.3)$$

and apparent density is the mass per unit volume of the mixture,

$$\rho^\alpha = \frac{dm^\alpha}{dV}, \quad \alpha = s, f. \quad (2.4)$$

When a phase is intrinsically incompressible, its true density is constant. Volume

fractions for each phase are defined as

$$\phi^\alpha = \frac{dV^\alpha}{dV}, \quad \alpha = s, f, \quad (2.5)$$

and since the mixture is saturated,  $\phi^s + \phi^f = 1$ . As a result of Eq. (2.5), the true and apparent densities are related by

$$\rho^\alpha = \rho_T^\alpha \phi^\alpha, \quad \alpha = s, f. \quad (2.6)$$

## Derivation of the Equations

This derivation considers two continuum bodies, denoted body 'A' and body 'B'. Extensions to multiple-body contact are straightforward and are treated within the numerical procedure. The contact surface is defined by the relation  $\Gamma_c \equiv \Omega^A \cap \Omega^B$  and the fact that it must satisfy  $\Gamma_c \subset \mathcal{R}^{n_{sd}-1}$  with  $\Omega^A \subset \mathcal{R}^{n_{sd}}$  and  $\Omega^B \subset \mathcal{R}^{n_{sd}}$ , where  $n_{sd}$  is the number of spatial dimensions in the problem. At times, to emphasize terms associated with either body 'A' or body 'B', the notation  $\Gamma_c \cap \Omega^A$  will be used, although this intersection merely recovers the contact surface. Standard indicial notation is used, so summation is implied by the repeated indices  $i, j, k$  or  $m$ . Subscripts represent components and range  $1, 2 \dots n_{sd}$ ; superscripts 'A' and 'B' refer to the body with which a given quantity is associated.

Figure 2.2 depicts the geometry for this derivation at some time  $t > 0$ , along with its reference coordinate system. Physical parameters of the continuum may experience discontinuities across the surface  $\Gamma_c$ . Typically, the balance laws of continuum mechanics are posed in integral form, then reduced to differential form through an application of the Divergence Theorem. The resulting differential equations are valid in the domain of the integral. Due to possible discontinuities, the integral forms of the



balance laws will result in both differential equations for the domain and jump conditions at any interfaces between dissimilar materials. Derivations in the subsequent sections follow the presentation by Hou *et al.* [64], with material also taken from the publication on the biphasic theory for soft hydrated tissues by Mow *et al.* [96].

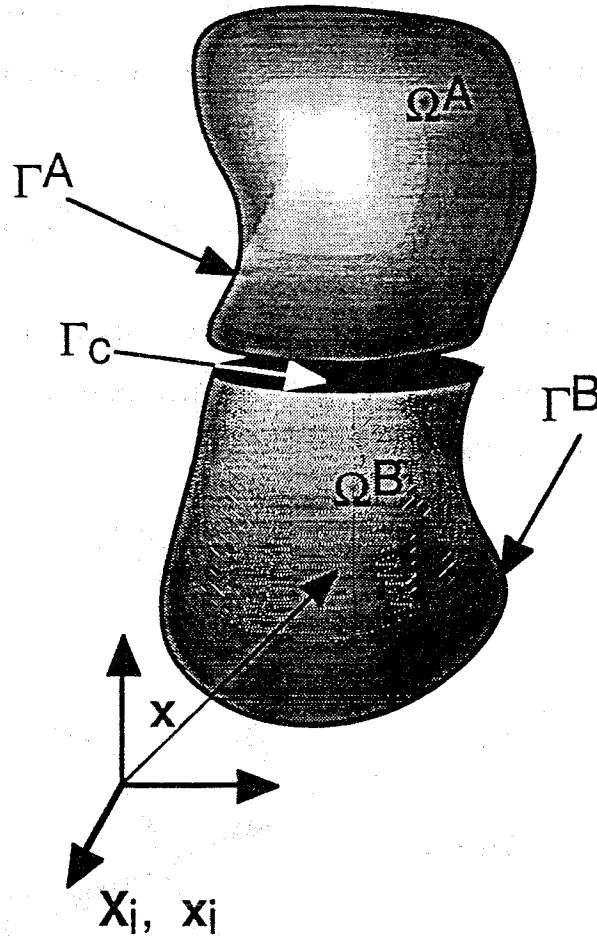


Fig. 2.2 Spatial domain for the derivation of multi-body biphasic contact equations.

### Continuity of Solid Displacement

Continuity of solid displacement does not result from the balance laws, but does provide a required continuity relation for well-posedness of the system of equations. A

biphasic material is defined as a continuum mixture of solid and fluid components and the extent of this material is defined by the boundary of the solid phase. For this reason it is reasonable to require that points in persistent contact will have the same normal solid displacement and normal solid velocity. Sliding parallel to the interface is allowed, so there is no restriction on the tangential component of velocity. To allow for points that are not in contact at the initial time, this constraint is written in terms of the initial position,  $\mathbf{X}$ , and the displacement,  $\mathbf{u}$ ,

$$\left[ (u_i^{sA} + X_i^{sA}) - (u_i^{sB} + X_i^{sB}) \right] n_i = 0, \quad (2.7)$$

where  $\mathbf{n}$  is a unique normal vector on the surface. By the indicial notation convention, Eq. (2.7) is a scalar equation. The time derivative of Eq. (2.7) also implies that normal solid velocity is continuous,

$$v_i^{sA} n_i = v_i^{sB} n_i. \quad (2.8)$$

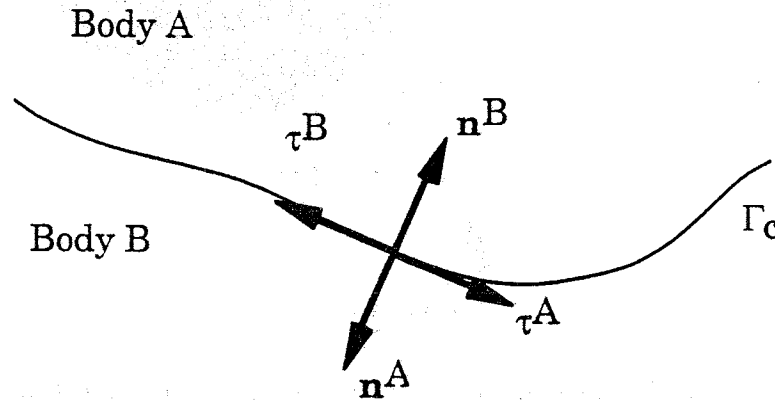


Fig. 2.3 Convention for the definition of the normal and tangent vectors at a point on the contact surface.

On the interface, tangent and normal vectors can be defined for each body in contact, as in Fig. 2.3. With this definition, any vector quantity at the surface can be decomposed into components in these directions, with respect to either the coordinate

system of side 'A' or of side 'B'. Figure 2.4 illustrates the decomposition for a traction vector for the case  $n_{sd} = 2$ .

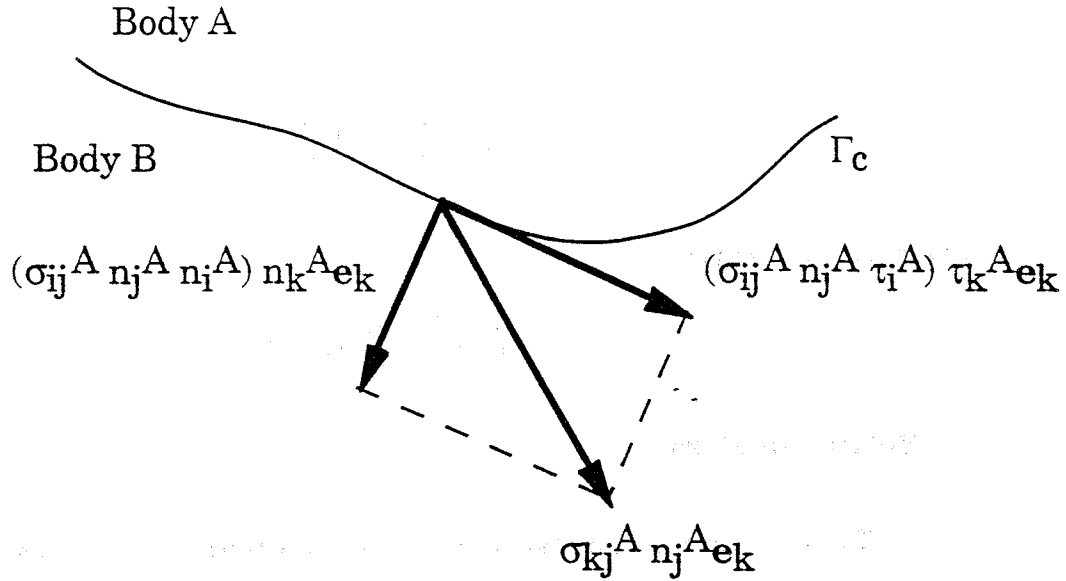


Fig. 2.4 Decomposition of the traction vector at a point on Body A with respect to the normal and tangent vectors of Body A.

In Figs. 2.3 and 2.4,  $\mathbf{n}$  is an unit outward normal vector,  $\boldsymbol{\tau}$  an unit tangent vector and  $\mathbf{e}_k$  are the standard unit coordinate vectors. For the two dimensional case,  $\boldsymbol{\tau}$  is defined such that  $\mathbf{n} \times \boldsymbol{\tau} = \mathbf{e}_3$  and  $\mathbf{n} \cdot \boldsymbol{\tau} = 0$ . In three dimensions, a triad of surface coordinates is defined such that  $\mathbf{n}$  is again the unit outward normal vector,  $\mathbf{n} \cdot \boldsymbol{\tau}^1 = 0$  and  $\mathbf{n} \times \boldsymbol{\tau}^1 = \boldsymbol{\tau}^2$ . In the derivations that follow, vectors will be decomposed in two-dimensional space, though analogous derivations (with identical results for the frictionless case) could be done for three dimensions. It is apparent from Fig. 2.3 that

$$\mathbf{n}^A = -\mathbf{n}^B \quad (2.9a)$$

and

$$\boldsymbol{\tau}^A = -\boldsymbol{\tau}^B. \quad (2.9b)$$

Hence, Eq. (2.8), can be written as either

$$v_i^{sA} n_i^A = v_i^{sB} n_i^A, \quad (2.10a)$$

or

$$v_i^{sA} n_i^B = v_i^{sB} n_i^B, \quad (2.10b)$$

or the more convenient form

$$v_i^{sA} n_i^A + v_i^{sB} n_i^B = 0. \quad (2.11)$$

### Balance of Mass

To begin, an integral statement of the conservation of mass for the mixture is written,

$$\frac{d}{dt} \int_{\Omega} (\rho^s + \rho^f) d\Omega = - \int_{\Gamma} \rho^f (v_i^f - v_i^s) n_i d\Gamma. \quad (2.12)$$

Equation (2.12) is the mixture equivalent of the familiar mass balance and states that the time rate of change of mass in the spatial volume is equal to the mass flux across all boundaries. Observe that relative flow terms are included, since the fluid can move with respect to the solid. Next, any possible discontinuities are accounted for by separating integrals into portions over each body, and their boundaries.

$$\begin{aligned} & \frac{d}{dt} \int_{\Omega^A} (\rho^{sA} + \rho^{fA}) d\Omega + \frac{d}{dt} \int_{\Omega^B} (\rho^{sB} + \rho^{fB}) d\Omega = \\ & = - \int_{\Gamma^A \cup \Gamma_c} \rho^{fA} (v_i^{fA} - v_i^{sA}) n_i d\Gamma - \int_{\Gamma^B \cup \Gamma_c} \rho^{fB} (v_i^{fB} - v_i^{sB}) n_i d\Gamma + \end{aligned}$$

$$+ \int_{\Gamma_c} \rho^A f^A (v_i^A - v_i^S) n_i^A d\Gamma + \int_{\Gamma_c} \rho^B f^B (v_i^B - v_i^S) n_i^B d\Gamma \quad (2.13)$$

An application of Reynold's Transport Theorem yields

$$\begin{aligned} & \int_{\Omega^A} \left[ \frac{\partial \rho^S A}{\partial t} + (\rho^S A v_i^S)_{,i} + \frac{\partial \rho^f A}{\partial t} + (\rho^f A v_i^f)_{,i} \right] d\Omega + \\ & + \int_{\Omega^B} \left[ \frac{\partial \rho^S B}{\partial t} + (\rho^S B v_i^S)_{,i} + \frac{\partial \rho^f B}{\partial t} + (\rho^f B v_i^f)_{,i} \right] d\Omega = \\ & = \int_{\Gamma_c} \rho^A f^A (v_i^A - v_i^S) n_i^A d\Gamma + \int_{\Gamma_c} \rho^B f^B (v_i^B - v_i^S) n_i^B d\Gamma, \end{aligned} \quad (2.14)$$

which is valid for an arbitrary domain, thus producing three equations, one each from the integrals in  $\Omega^A$ ,  $\Omega^B$  and on  $\Gamma_c$ . In indicial notation, the comma indicates differentiation with respect to the components which follow. The relations in square brackets in the first two lines of Eq. (2.14) represent mixture continuity on either side of the surface of discontinuity. These may be combined as a mixture continuity relation to be satisfied in the domain  $\Omega = \Omega^A \cup \Omega^B$ ,

$$\frac{\partial(\rho^S + \rho^f)}{\partial t} + (\rho^S v_i^S + \rho^f v_i^f)_{,i} = 0. \quad (2.15a)$$

The third line of Eq. (2.14) yields a contact boundary condition to be satisfied on the surface  $\Gamma_c$ ,

$$\rho^A f^A (v_i^A - v_i^S) n_i^A + \rho^B f^B (v_i^B - v_i^S) n_i^B = 0. \quad (2.15b)$$

It is often more convenient to work with volume fractions rather than with densities. To accomplish this observe that Eq. (2.15a) can also be obtained by summing the

continuity relations for each phase, obtained by applying the above principles to each phase [96], which are

$$\frac{\partial(\rho^\alpha)}{\partial t} + (\rho^\alpha v_i^\alpha)_{,i} = 0, \quad \alpha=s,f. \quad (2.16)$$

Substituting Eq. (2.6) and invoking the assumption of intrinsic incompressibility for each phase this becomes

$$\frac{\partial(\phi^\alpha)}{\partial t} + (\phi^\alpha v_i^\alpha)_{,i} = 0, \quad \alpha=s,f. \quad (2.17)$$

In the linear model, volume fractions are assumed to be independent of deformation, so the time derivative vanishes. Thus, for the linear model, an alternate form of the mixture continuity relation is

$$(\phi^s v_i^s + \phi^f v_i^f)_{,i} = 0. \quad (2.18)$$

A similar reduction is performed for the contact boundary condition. Substituting Eq. (2.6) into Eq. (2.15b), and recognizing that the true density of the fluid phase does not experience a discontinuity across  $\Gamma_c$ , one arrives at

$$\phi^f v_i^f (v_i^f - v_i^s) n_i^A + \phi^f v_i^f (v_i^f - v_i^s) n_i^B = 0. \quad (2.19)$$

Now employing the continuity of solid velocity, Eq. (2.11), and the condition of a saturated mixture, Eq. (2.19) simplifies to

$$(\phi^f v_i^f + \phi^s v_i^s) n_i^A + (\phi^f v_i^f + \phi^s v_i^s) n_i^B = 0. \quad (2.20a)$$

For points in persistent contact, this can be expressed equivalently in terms of displacement and reference position,

$$\begin{aligned}
& \left( \phi^f A (u_i^f A + X_i^f A) + \phi^s A (u_i^s A + X_i^s A) \right) n_i^A + \\
& + \left( \phi^f B (u_i^f B + X_i^f B) + \phi^s B (u_i^s B + X_i^s B) \right) n_i^B = 0,
\end{aligned} \tag{2.20b}$$

where the time derivative of Eq. (2.20b) gives Eq. (2.20a).

### Balance of Linear Momentum

A similar set of steps is followed for the balance of linear momentum, which is written as,

$$\begin{aligned}
& \frac{d}{dt} \int_{\Omega} (\rho^s v_i^s + \rho^f v_i^f) d\Omega = - \int_{\Gamma} \rho^f v_i^f (v_j^f - v_j^s) n_j d\Gamma + \\
& + \int_{\Gamma} (\sigma_{ij}^f + \sigma_{ij}^s) n_j d\Gamma + \int_{\Omega} (T_i^f + T_i^s) d\Omega + \int_{\Omega} (\Pi_i^f + \Pi_i^s) d\Omega,
\end{aligned} \tag{2.21}$$

where  $\sigma^\alpha$  is the Cauchy stress tensor for the  $\alpha$  phase,  $T^\alpha$  are external body forces and  $\Pi^\alpha$  are vectors of momentum supply of one phase to the other. Since the momentum supply is balanced between the two phase, the vectors  $\Pi^s$  and  $\Pi^f$  are equal and opposite. Equation (2.21) states that the time rate of change of momentum in the domain is balanced by the momentum flux through the boundary, surface tractions and body forces. Again the integrals are separated into terms in each body and on the boundaries. After applying Reynold's Transport Theorem the mixture momentum equation,

$$\begin{aligned}
& (\sigma_{ijj}^f + \sigma_{ijj}^s) = \\
& = -T_i^f - T_i^s + \rho^s \frac{\partial v_i^s}{\partial t} + \rho^s v_i^s v_{jj}^s + \rho^f \frac{\partial v_i^f}{\partial t} + \rho^f v_i^f v_{jj}^f,
\end{aligned} \tag{2.22a}$$

and a third contact boundary condition,

$$\begin{aligned}
& (\sigma_{ij}^{sA} + \sigma_{ij}^{fA}) n_j^A + (\sigma_{ij}^{sB} + \sigma_{ij}^{fB}) n_j^B = \\
& = \rho^f v_i^f (v_j^f - v_j^s) n_j^A + \rho^f v_i^f (v_j^f - v_j^s) n_j^B, \quad (2.22b)
\end{aligned}$$

result. The momentum exchange does not appear in Eq. (2.22a), but it does appear in the momentum equations for each phase, which are [96]

$$\sigma_{ijj}^\alpha + \Pi_i^\alpha = -T_i^\alpha + \rho^\alpha \frac{\partial v_i^\alpha}{\partial t} + \rho^\alpha v_i^\alpha v_{jj}^\alpha, \quad \alpha = s, f, \quad (2.23)$$

and which readily sum to Eq. (2.22a). In the absence of body forces and inertial terms, and by invoking the assumption that no energy is lost due to convection on the contact surface, the right hand side of each of Eqns. (2.22-23) can be set to zero.

### Balance of Energy

The energy balance for the mixture is expressed as

$$\begin{aligned}
& \frac{\partial}{\partial t} \int_{\Omega} \left( e^f + \frac{1}{2} \rho^f v_i^f v_i^f + e^s + \frac{1}{2} \rho^s v_i^s v_i^s \right) d\Omega = - \int_{\Gamma} \rho^f \left( e^f + \frac{1}{2} v_i^f v_i^f \right) (v_j^f - v_j^s) n_j d\Gamma + \\
& + \int_{\Gamma} (v_i^f \sigma_{ij}^{ff} + v_i^s \sigma_{ij}^{ss}) n_j d\Gamma + \int_{\Omega} (T_i^f v_i^f + T_i^s v_i^s) d\Omega - \int_{\Gamma} (h_i^f + h_i^s) n_i d\Gamma + \\
& + \int_{\Omega} (\Pi_i^f v_i^f + \Pi_i^s v_i^s) d\Omega + \int_{\Omega} (\tilde{e}^f + \tilde{e}^s) d\Omega, \quad (2.24)
\end{aligned}$$

where  $e^\alpha$  is the internal energy density,  $h^\alpha$  is the heat flux and  $\tilde{e}^\alpha$  is the internal energy supply for the  $\alpha$  phase. Again, applying Reynold's Transport Theorem, the differential form of the energy equation is

$$(\sigma_{ijj}^{ss})_{,i} - \rho^s \left( \frac{\partial e^s}{\partial t} + v_i^s e_{,i}^s \right) + (\sigma_{ijj}^{ff})_{,i} - \rho^f \left( \frac{\partial e^f}{\partial t} + v_i^f e_{,i}^f \right) =$$



$$\begin{aligned}
&= h_{i,i}^f - T_i^f v_i^f + \frac{1}{2} \rho^f \left( \frac{\partial}{\partial t} v_j^f v_j^f + v_i^f (v_j^f v_j^f)_{,i} \right) + \\
&+ h_{i,i}^s - T_i^s v_i^s + \frac{1}{2} \rho^s \left( \frac{\partial}{\partial t} v_j^s v_j^s + v_i^s (v_j^s v_j^s)_{,i} \right)
\end{aligned} \tag{2.25a}$$

and the fourth contact boundary condition is

$$\begin{aligned}
&\sigma_{ij}^{sA} v_j^{sA} n_i^A + \sigma_{ij}^{fA} v_j^{fA} n_i^A + \sigma_{ij}^{sB} v_j^{sB} n_i^B + \sigma_{ij}^{fB} v_j^{fB} n_i^B = \\
&= (h_i^{sA} + h_i^{fA}) n_i^A + \rho^{fA} \left( e^{fA} + \frac{1}{2} v_j^{fA} v_j^{fA} \right) v_i^{fA} - v_i^{sA} n_i^A + \\
&+ (h_i^{sB} + h_i^{fB}) n_i^B + \rho^{fB} \left( e^{fB} + \frac{1}{2} v_j^{fB} v_j^{fB} \right) v_i^{fB} - v_i^{sB} n_i^B.
\end{aligned} \tag{2.25b}$$

Using the assumptions of isothermal deformation, no body forces and no convective losses, the right hand sides of Eqns. (2.25a,b) become zero.

### Constitutive Assumptions and the Entropy Inequality

A significant part of the effort in developing a continuum theory for tissue mechanics has been spent in defining the correct constitutive relations. One can postulate any form for the constitutive relations, but then they must be evaluated *a posteriori* to determine if they are admissible. In particular, they must provide reasonable physical behaviour and must be mathematically correct. There are several principles in continuum mechanics which are used for this determination. First, the solution must be objective, that is, it must be the same when measured from different frames of reference. Second, it must satisfy the Clausius-Duhem inequality, also known as the entropy inequality [153]. Third, the governing equations must be well-posed when the constitutive relation is implemented, and must not admit any non-physical behaviour.

There are three constitutive relations required for the biphasic theory: solid stress,

fluid stress and momentum exchange. For the linear theory, a set of constitutive laws satisfying the above criteria were proposed by Mow *et al.* in 1980 [96]. Since this thesis is concerned with evaluating new contact elements, the complete derivation of the constitutive relations is not presented; they are summarized at the end of this chapter. Note that the contact boundary conditions as they have been derived in this section are not explicitly dependent on the constitutive laws. Thus, the present contact finite element will be applicable when more advanced material models are used.

Current research in constitutive modeling is predominantly focused on nonlinear relations. In particular, solid stress is known to be nonlinearly dependent on deformation, anisotropic with respect to orientation and anisotropic with respect to tension and compression [7,35]. Tissue permeability, and hence momentum exchange, are exponentially dependent on deformation [61,62]. It will be essential to model these effects when physiological problems in diarthrodial joint mechanics are studied, but they are not included in the present evaluation of contact finite elements.

## Reduction to Frictionless Contact

While the four contact boundary conditions derived above are sufficient to define a well-posed mathematical problem, they are not well-suited to numerical analysis by the finite element method. In particular, Eq. (2.25b), which contains products of kinematic and kinetic quantities, would be difficult to implement in the numerical procedure. Simple algebraic manipulations will result in an equivalent set of contact boundary conditions which are similar in form to those for single phase solid mechanics. At the same time, the assumption of frictionless contact will be introduced into the relations.

Experimental studies with articular cartilage indicate that the coefficient of

friction is extremely low [85,89], thus the present formulation will include this assumption in the contact boundary conditions. For frictionless contact, the tangential components of traction will be zero. Beginning with the momentum jump condition, Eq. (2.22b), the right hand side is set to zero by invoking the modeling assumptions presented with that equation, then the total stress,  $\sigma_{ij}^T$ , is defined to be the sum of the solid and fluid stresses. Now the vector equation is written in terms of its components in the normal and tangential directions:

$$(\sigma_{ij}^{TA} n_j^A n_i^A) n_k^A + (\sigma_{ij}^{TA} n_j^A \tau_i^A) \tau_k^A + (\sigma_{ij}^{TB} n_j^B n_i^B) n_k^B + (\sigma_{ij}^{TB} n_j^B \tau_i^B) \tau_k^B = 0. \quad (2.26)$$

Using the relation between the normal and tangent vectors on opposite sides of the interface this becomes,

$$\left[ (\sigma_{ij}^{TA} n_j^A n_i^A) - (\sigma_{ij}^{TB} n_j^B n_i^B) \right] n_k^A + \left[ (\sigma_{ij}^{TA} n_j^A \tau_i^A) - (\sigma_{ij}^{TB} n_j^B \tau_i^B) \right] \tau_k^A = 0. \quad (2.27)$$

Eliminating the tangential components of traction, one obtains a scalar equation relating the normal components,

$$(\sigma_{ij}^{sA} + \sigma_{ij}^{fA}) n_j^A n_i^A - (\sigma_{ij}^{sB} + \sigma_{ij}^{fB}) n_j^B n_i^B = 0. \quad (2.28)$$

Similar reductions are performed in the energy jump equation, Eq. (2.25b), after having set the right hand side to zero. Now expand the traction and velocity vectors in terms of components in the normal and tangential directions. For just the first term, this takes the form:

$$\sigma_{ij}^{sA} n_i^A v_j^A = \left[ (\sigma_{ki}^{sA} n_i^A n_k^A) n_j^A + (\sigma_{ki}^{sA} n_i^A \tau_k^A) \tau_j^A \right] \left[ (v_m^{sA} n_m^A) n_j^A + (v_m^{sA} \tau_m^A) \tau_j^A \right] \quad (2.29)$$

Note that the terms in parentheses are scalar magnitudes and recall that the inner product  $\mathbf{n}^A \cdot \mathbf{n}^A = 1$ , while  $\mathbf{n}^A \cdot \boldsymbol{\tau}^A = 0$ . Performing the multiplication on the right hand side of

Eq. (2.29) results in a scalar equation,

$$\sigma_{ij}^{sA} n_i v_j^{sA} = (\sigma_{ki}^{sA} n_i n_k) (v_m^{sA} n_m) + (\sigma_{ki}^{sA} n_i \tau_k) (v_m^{sA} \tau_m). \quad (2.30)$$

Tangential components of traction on the interface are assumed to be zero, so similar manipulations for the three remaining terms in Eq. (2.25b) yields,

$$\begin{aligned} & (\sigma_{ki}^{sA} n_i n_k) (v_m^{sA} n_m) + (\sigma_{ki}^{fA} n_i n_k) (v_m^{fA} n_m) + \\ & + (\sigma_{ki}^{sB} n_i n_k) (v_m^{sB} n_m) + (\sigma_{ki}^{fB} n_i n_k) (v_m^{fB} n_m) = 0. \end{aligned} \quad (2.31)$$

From the above, Eqns. (2.7) or (2.11), (2.20), (2.28) and (2.31) form a set of interface conditions for biphasic-biphasic, frictionless contact, and are valid in the limiting cases of solid or fluid on either side of the interface. These derivations apply when the fluid (either the fluid phase of a biphasic tissue or a pure fluid material) is inviscid, since any inertia terms have been neglected. These equations can be further manipulated before they are used in the numerical procedure. Apply Eq. (2.11) to Eq. (2.31), and note the change in the dummy indices,

$$\begin{aligned} & v_m^{sA} n_m \left[ (\sigma_{ik}^{sA} n_i n_k) - (\sigma_{ik}^{sB} n_i n_k) \right] + \\ & + (\sigma_{ik}^{fA} n_i n_k) (v_m^{fA} n_m) + (\sigma_{ik}^{fB} n_i n_k) (v_m^{fB} n_m) = 0. \end{aligned} \quad (2.32)$$

Equation (2.28) can be used to eliminate the solid stress, and after multiplying by  $(\phi^{sA} - \phi^{sB})$ , Eq. (2.19) is used to eliminate solid velocity,

$$\begin{aligned} & \left[ \phi^{fA} (v_i^{fA} n_i) + \phi^{fB} (v_i^{fB} n_i) \right] \left[ (\sigma_{ik}^{fA} n_i n_k) - (\sigma_{ik}^{fB} n_i n_k) \right] + \\ & + (\phi^{sA} - \phi^{sB}) \left[ (\sigma_{ik}^{fA} n_i n_k) (v_m^{fA} n_m) + (\sigma_{ik}^{fB} n_i n_k) (v_m^{fB} n_m) \right] = 0. \end{aligned} \quad (2.33)$$

Expanding this equation and using the relation  $\phi^s = 1 - \phi^f$  results in

$$\frac{(\sigma_{ik}^{fA} n_i^A n_k^A)}{\phi^{fA}} - \frac{(\sigma_{ik}^{fB} n_i^B n_k^B)}{\phi^{fB}} = 0. \quad (2.34)$$

Note that in the case of a pure solid this equation is not applicable. In the final finite element matrix equations, though, one observes that there is no division by either  $\phi^s$  or  $\phi^f$ . Also, for  $\phi^{sA} = \phi^{sB}$ , this equation is consistent with the interface conditions, namely that normal solid velocity, normal fluid velocity, normal solid traction and normal fluid traction are continuous. These are trivially obtained from Eqns. (2.11), (2.20), (2.28) and (2.31) when the solid volume fractions are equal.

A second reduced kinetic interface condition can also be obtained by using Eq. (2.34) in Eq. (2.32),

$$\begin{aligned} & \phi^{fA} (v_m^{sA} n_m^A) \left[ (\sigma_{ik}^{sA} n_i^A n_k^A) - (\sigma_{ik}^{sB} n_i^B n_k^B) \right] + \\ & + (\sigma_{ik}^{fA} n_i^A n_k^A) \left[ \phi^{fA} (v_i^{fA} n_i^A) + \phi^{fB} (v_i^{fB} n_i^B) \right] = 0. \end{aligned} \quad (2.35)$$

Substituting from Eq. (2.19) then Eq. (2.32) the following will result,

$$(\sigma_{ik}^{sA} n_i^A n_k^A) - (\sigma_{ik}^{sB} n_i^B n_k^B) - \frac{\phi^{sA}}{\phi^{fA}} (\sigma_{ik}^{fA} n_i^A n_k^A) + \frac{\phi^{sB}}{\phi^{fB}} (\sigma_{ik}^{fB} n_i^B n_k^B) = 0. \quad (2.36)$$

## Summary

The system of differential equations to which the finite element method will be applied are the continuity relation for the mixture,

$$(\phi^s v_i^s + \phi^f v_i^f)_{,i} = 0, \quad (2.37)$$

and the momentum equations for the solid and fluid phases,

$$\sigma_{ij,j}^\alpha + \Pi_i^\alpha = 0, \quad \alpha = s, f. \quad (2.38)$$

There are three constitutive laws to govern the momentum exchange and stress-strain behaviour:

$$\Pi_i^s = -\Pi_i^f = p \phi_{,i}^s + K(v_i^f \cdot v_i^s), \quad (2.39a)$$

$$\sigma_{ij}^s = -\phi^s p \delta_{ij} + D_{ijkl}^s \varepsilon_{km}^s, \quad (2.39b)$$

$$\sigma_{ij}^f = -\phi^f p \delta_{ij} + D_{ijkl}^f \varepsilon_{km}^f, \quad (2.39c)$$

where  $K = \frac{\phi^f{}^2}{\kappa}$  [81],  $\kappa$  is the tissue permeability,  $p$  is the interstitial pressure,  $\varepsilon^s$  is solid strain and  $\dot{\varepsilon}^f$  is fluid strain rate. These are derived with the previously stated assumptions on small deformations, constant permeability and volume fractions constant in time. The fourth rank tensors  $D^\alpha$  admit orthotropic behaviour, but are not dependent on deformation. By ignoring viscous effects of the fluid when deriving the contact conditions, non-zero values of  $D^f$  are precluded. The four frictionless contact continuity relations are

$$(u_i^{sA} + X_i^{sA}) n_i^A + (u_i^{sB} + X_i^{sB}) n_i^B = 0, \quad (2.40a)$$

$$\begin{aligned} & \left( \phi^{fA} (u_i^{fA} + X_i^{fA}) + \phi^{sA} (u_i^{sA} + X_i^{sA}) \right) n_i^A + \\ & + \left( \phi^{fB} (u_i^{fB} + X_i^{fB}) + \phi^{sB} (u_i^{sB} + X_i^{sB}) \right) n_i^B = 0. \end{aligned} \quad (2.40b)$$

$$\frac{(\sigma_{ik}^{fA} n_i^A n_k^A)}{\phi^{fA}} - \frac{(\sigma_{ik}^{fB} n_i^B n_k^B)}{\phi^{fB}} = 0, \quad (2.40c)$$

$$(\sigma_{ik}^{sA} n_i^A n_k^A) - (\sigma_{ik}^{sB} n_i^B n_k^B) - \frac{\phi^{sA}}{\phi^{fA}} (\sigma_{ik}^{fA} n_i^A n_k^A) + \frac{\phi^{sB}}{\phi^{fB}} (\sigma_{ik}^{fB} n_i^B n_k^B) = 0. \quad (2.40d)$$

Interpreted with respect to the linear constitutive relations, Eqns. (2.39), the above represent continuity of normal solid velocity, continuity of normal relative fluid flow, continuity of

pressure and continuity of normal elastic traction. There are two kinematic, or essential, boundary conditions

$$v_i^s = \bar{v}_i^s \text{ on } \Gamma_{v_i^s}, \quad (2.41a)$$

$$v_i^f = \bar{v}_i^f \text{ on } \Gamma_{v_i^f}, \quad (2.41b)$$

and two kinetic, or natural, boundary conditions

$$\sigma_{ij}^s n_j = t_i^s = \bar{t}_i^s \text{ on } \Gamma_{t_i^s}, \quad (2.42a)$$

$$\sigma_{ij}^f n_j = t_i^f = \bar{t}_i^f \text{ on } \Gamma_{t_i^f}. \quad (2.42b)$$

Initial conditions are also required for this first order differential system in time, and so displacement and velocity are chosen to be zero at  $t = 0$ . There are three additional relations required to uniquely determine the correct contact area. The Kuhn-Tucker conditions of optimality [52] for a contact problem state that anywhere on the material boundary:

$$\|g(s)\| \geq 0, \quad (2.43a)$$

$$t^T(s) \cdot n(s) \leq 0, \quad (2.43b)$$

$$\|g(s)\| t^T(s) \cdot n(s) = 0, \quad (2.43c)$$

where  $g(s)$  is closest point projection to an opposing surface,  $t^T(s)$  is the total traction vector and  $s$  is a surface coordinate. These are also the familiar boundary inequalities that result from the Signorini problem for linear elasticity, as reported by Kikuchi and Oden [75]. These relations are intuitive, since a free surface must be traction-free and have a

positive distance to an opposing surface, and since bodies in contact must experience a compressive surface traction.



# Chapter III: Alternate Contact Formulations

## Introduction

Contact problems in elasticity are posed as differential equations subject to constraints. Often the constraints are inequalities, as in the case of the Signorini problem (see Eqns. (2.43)). In general, the resulting system of equations is very complex, and there are few problems for which analytic solutions exist [72]. One of the common approaches for analytic solution is to define the action of one body on the other as an unknown distribution of traction. The Boussinesq solution can be applied to find the displacement field, and then the integral of traction is equated to the applied load to complete the solution. This was the approach taken by Hertz when he published the first contact solutions [59]. For a numerical solution by the finite element method, this approach is not feasible.

The alternative is to develop an approximation of the governing differential equations together with their constraints. Often there are complications when solving constrained problems by the finite element method, as is the case with elements for incompressible elasticity (see, for example, [19,90,109]). Before choosing a biphasic contact finite element, it is instructive to look at contact elements for single phase elasticity. This chapter presents a brief overview of the common methods of applying constraints in the finite element method, and evaluates the resulting contact elements for accuracy and computational efficiency. With an understanding of these tools and a knowledge of the existing biphasic elements, a choice is made for the biphasic contact finite element formulation.

## Methods of Applying Constraints

The interface boundary conditions, Eqns. (2.40), derived in the previous chapter are constraints to be applied to the governing equations. For the biphasic theory these are equality constraints that relate the primary variables (velocity and displacement), or their derivatives (stresses), to one another. In the finite element method, relations among the primary variables can be treated by special assembly operations for elements on the contact surface when there is node-to-node contact. It would be an unusually restrictive assumption, however, to have node-to-node contact at all times. Furthermore, conditions on the stresses can not be treated in this manner for a displacement-based element.

There are numerous ways in which to enforce constraints on the finite element equations, but the two most common would be Lagrange multipliers and penalty function methods. Each of those methods has its advantages and disadvantages. The method of augmented Lagrangians combines their best features into a single, robust algorithm. Because of the close association between finite element methods and variational calculus, it is natural to describe the constraint process in terms of energy functionals, though the conclusions reached in this chapter can be extrapolated directly to the weighted residual method applied to a system of differential equations. For a more complete discussion of finite element formulations for variational principles, and the constraint operations, the reader is referred to chapter nine of the text by Zienkiewicz and Taylor [165].

### Penalty Methods

A penalty method approximates the constraint, without increasing the number of unknowns in the problem. For example, given a functional,

$$I(\mathbf{x}) = \int_{\Omega} E(\mathbf{f}, \mathbf{f}_{\mathbf{x}}) d\Omega, \quad (3.1a)$$

and a scalar-valued, algebraic constraint to be enforced pointwise on the surface  $\Gamma$ ,

$$G(\mathbf{f}, \mathbf{f}_{\mathbf{x}}) = 0 \quad \text{on } \Gamma, \quad (3.1b)$$

the penalized functional can be written as

$$J_P(\mathbf{x}) = \int_{\Omega} E(\mathbf{f}, \mathbf{f}_{\mathbf{x}}) d\Omega + \beta \int_{\Gamma} G(\mathbf{f}, \mathbf{f}_{\mathbf{x}})^2 d\Gamma, \quad (3.2)$$

where  $\beta$  is a known, user-specified penalty parameter. Both the function  $\mathbf{f}$  and its derivative,  $\mathbf{f}_{\mathbf{x}}$ , are free to vary, and in the limit  $\beta \rightarrow \infty$ , the constraint on  $G$  is satisfied in the integral sense. The penalty parameter must be chosen to adequately constrain the problem, but not numerically overwhelm terms coming from the integral of  $E$ . There is often a wide range of values in which the penalty parameter can be chosen such that the constraints are satisfied without causing ill-conditioning. If the constraint were posed as either an integral or differential relation, the same principle applies.

A simple example will illustrate the approximate nature of the constraint satisfaction. Take as the functional a parabola  $I(x) = x^2$ , subject to the trivial, algebraic constraint that  $x = 1$ . The variation of the unconstrained functional yields

$$\delta I(x) = 2x \delta x = 0, \quad (3.3)$$

which has the obvious solution of a minimum at zero. The constrained functional is

$$J_P(x) = x^2 + \beta (x-1)^2, \quad (3.4)$$

and its variation is

$$\delta J_P(x) = 2x \delta x + 2\beta(x-1)\delta x = 0, \quad (3.5a)$$

yielding

$$x = \frac{\beta}{1+\beta}. \quad (3.5b)$$

Graphically, Fig. 3.1 illustrates that the solution of Eq. (3.5b) approaches the true value as the penalty number grows larger.

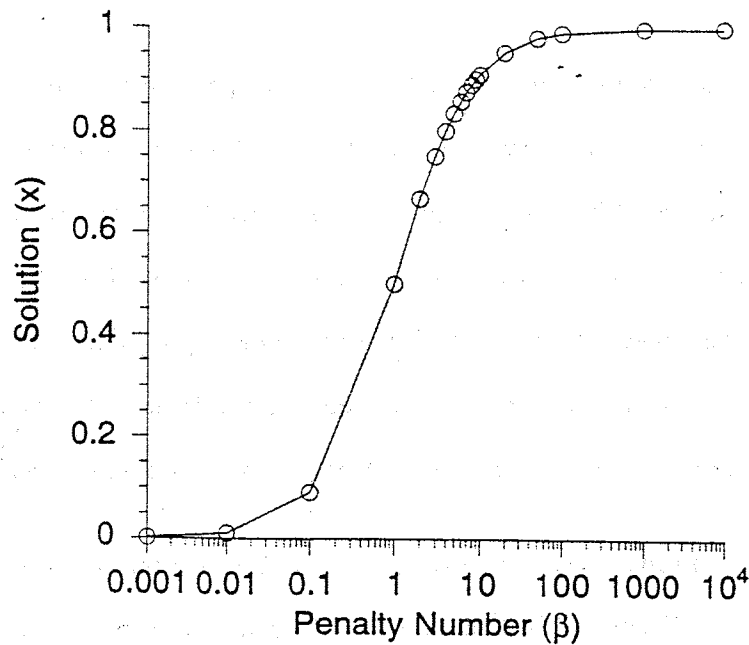


Fig. 3.1 Solution to a single-variable constrained problem by the penalty method.

Note that the solution converges to the correct answer from below. In the case of an inequality constraint, for example  $x \geq 1$ , an additional relation is necessary to define the region of feasible solutions. To see how the penalty function modifies the original functional, Fig. 3.2 plots the penalty functional, Eq. (3.4), *verses*  $x$  for two different values of  $\beta$ . One observes that the penalty method creates a convex function whose minimum is

approximately at the desired location. As the penalty number increases, the minimum shifts toward the true value and the convexity increases. This illustrates how ill-conditioning can result when the penalty number is too large, since minimizing a highly convex function can be numerically unstable.

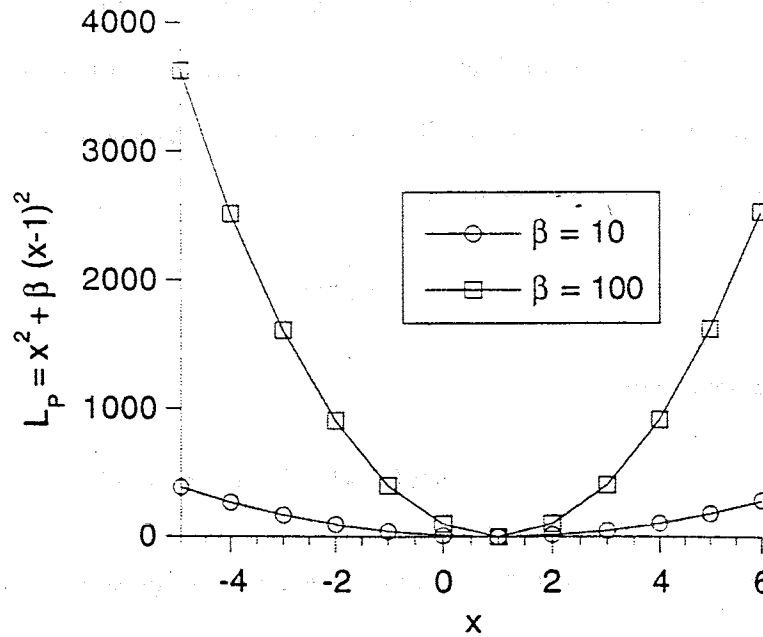


Fig. 3.2 Penalty functional for a single-variable constrained problem and two different values of the penalty parameter,  $\beta$ .

### Lagrange Multipliers

Lagrange multipliers introduce additional variables to enforce constraints on a set of equations. Equations (3.1) can be written with the Lagrange multiplier,  $\lambda$ , as

$$J_L(\mathbf{x}) = \int_{\Omega} E(\mathbf{f}, \mathbf{f}_{\mathbf{x}}) d\Omega - \int_{\Gamma} \lambda G(\mathbf{f}, \mathbf{f}_{\mathbf{x}}) d\Gamma. \quad (3.6)$$

The variation of  $J$  set equal to zero is the stationary condition of a modified functional, where  $f$ ,  $f_x$  and  $\lambda$  are free to vary. (For readers familiar with Lagrange multipliers, the choice of a negative sign preceding the constraint term may seem inappropriate, though still mathematically correct. This choice provides continuity of the discussion for the augmented Lagrangian method, described below.) This method will exactly enforce the integral form of the constraint, at the cost of an additional variable for each constraint equation. Often one can find a relation between the multipliers and physically relevant variables in the formulation. Returning to the single-variable example in the previous section, the Lagrange functional is

$$J_L(x) = x^2 - \lambda (x-1), \quad (3.7a)$$

and its variation is

$$\delta J_L(x) = 2x \delta x - \delta \lambda (x-1) - \lambda \delta x. \quad (3.7b)$$

The stationary condition results in a system of two equations:

$$x - 1 = 0, \quad (3.8a)$$

$$2x - \lambda = 0. \quad (3.8b)$$

Equation (3.8a) gives the correct value for  $x$ , and Eq. (3.8b) identifies  $\lambda$  as the slope of the unconstrained functional. As with the penalty method, Lagrange multipliers can be used with inequality constraints provided there is some limiting relation to define the feasible region. The advantage of Lagrange multipliers is that an exact solution can be had, but at the cost of one additional variable for each constraint.

Similar to penalty methods, there is some numerical ill-conditioning that can result; the system of equations is semi-definite. For a physical understanding of the indefinite nature of the equations, observe that the Lagrange multiplier approach transforms the minimization of a convex system with a constraint to a saddle point problem with a stationary point and no constraints. Graphically, this is depicted in Fig 3.3 which shows the Lagrange functional,  $J_L$ , in the region of the solution. When discretized with the finite element method, this type of stationary solution can cause some finite elements to fail. The study of this problem has lead to the Babuska-Brezzi condition [18], for which a concise discussion of the mathematics is given by Oden and Kikuchi [108].

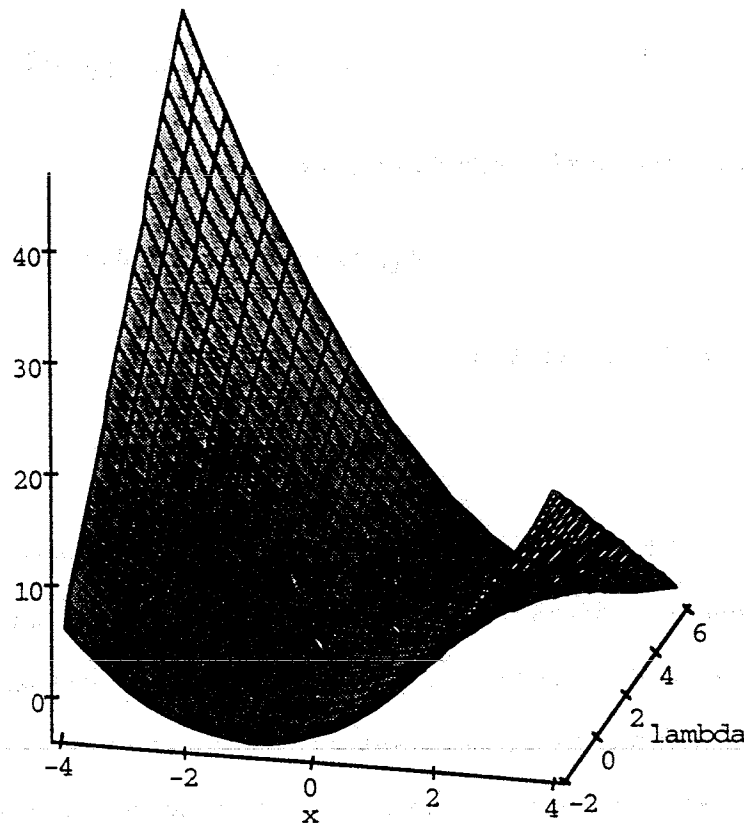


Fig. 3.3 Lagrange functional,  $J_L$ , plotted in the region of the solution.

## Augmented Lagrangians

Augmented Lagrangians include the best features of both the penalty and Lagrange multiplier methods. The augmented Lagrangian functional is created by including both a multiplier term and a penalty term,

$$J_{AL}(x) = \int_{\Omega} E(f, f_x) d\Omega - \int_{\Gamma} \lambda G(f, f_x) d\Gamma + \beta \int_{\Gamma} G(f, f_x)^2 d\Gamma. \quad (3.9)$$

As  $\beta$  tends to infinity, this functional will approximate the penalty functional, independent of the value of the multiplier. Thus, unlike the Lagrange multiplier formulation, the multiplier in Eq. (3.9) can be considered known, and not free to vary, without adversely affecting the solution. Applying this method to the model convex equation results in

$$J_{AL}(x) = x^2 - \lambda (x-1) + \beta (x-1)^2, \quad (3.10a)$$

whose variation with respect to  $x$  gives

$$\delta J_{AL}(x) = 2x \delta x - [\lambda - 2\beta(x-1)]\delta x. \quad (3.10b)$$

The equation for  $x$  is then

$$x = \frac{\lambda + 2\beta}{2 + 2\beta}. \quad (3.11)$$

This has the advantage that there are no additional variables introduced into the formulation, though some methodology to choose  $\lambda$  is required. Observe that in the limit  $\beta \rightarrow \infty$  Eq. (3.11) gives the correct solution for  $x$ , independent of  $\lambda$ . Also, when  $\lambda$  has the value indicated by Eq. (3.8b), the solution for  $x$  is correct, independent of  $\beta$ . This implies that even a poor choice of the penalty or multiplier will lead to the correct solution. The



power in augmented Lagrangian formulations is to use an iterative scheme to choose the multiplier. Comparing Eq. (3.7b) with Eq. (3.10b) suggests this iterative update for  $\lambda$  [52]:

$$\lambda^{(k+1)} = \lambda^{(k)} - 2\beta(x^{(k)} - 1), \quad (3.12a)$$

$$x^{(k)} = \frac{\lambda^{(k)} + 2\beta}{2 + 2\beta}, \quad (3.12b)$$

where  $k$  is the iteration counter.

The iterative solution process is depicted graphically in Figs. 3.4 and 3.5. The system of Eqns. (3.12) was solved using the MAPLE symbolic algebra package [31]. Ten iterations were performed for each of ten penalties in the range one through ten. An initial value of zero was used for the multiplier for each penalty. Note that this choice of penalty is significantly lower than those demonstrated in Fig. 3.1 to give accurate solutions.

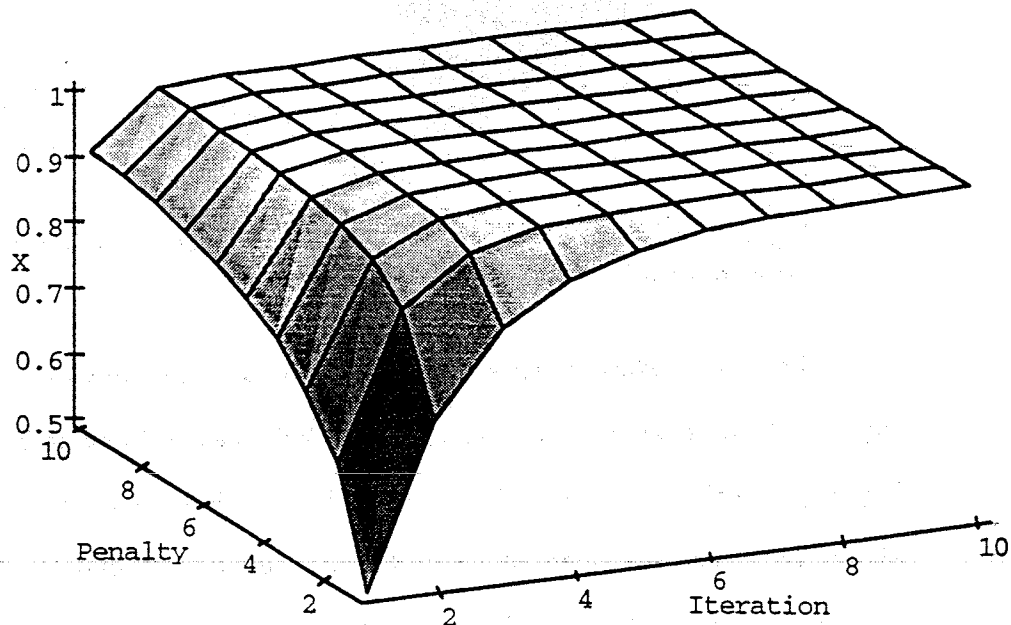


Fig. 3.4 Convergence of the augmented Lagrange functional with iteration for a range of penalties.

Figure 3.4 shows the solution value  $x^{(k)}$  plotted for the indicated range of penalties. With a penalty of one, the augmented Lagrange method will converge to within 1% of the correct solution in seven iterations, and for a penalty of ten this level of accuracy is achieved in just two iterations. For comparison, the penalty method is in error by 10% with a penalty of 10. A similar convergence is observed in Fig. 3.5 for the multiplier,  $\lambda^{(k)}$ .

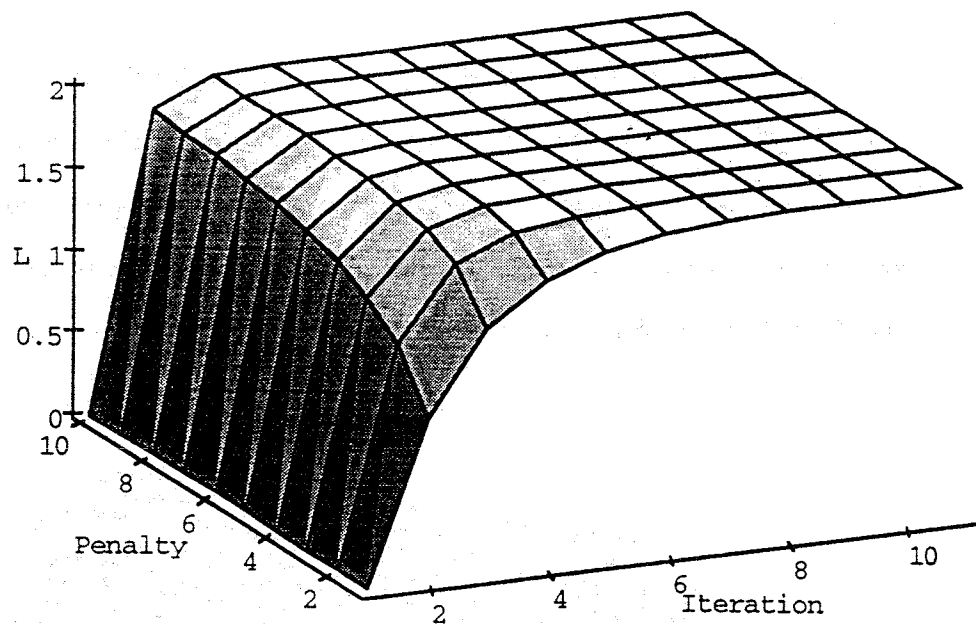


Fig. 3.5 Convergence of the augmented Lagrange multiplier with iteration for a range of penalties.

There are several theories that govern the convergence criteria for iterations of the augmented Lagrange method. Since the multipliers should approach the values of a pure Lagrange multiplier method, one could use them for the convergence check. Alternatively, an assessment of constraint violation is also possible. A third possibility is to examine the solution itself. Any of these criteria can be formulated as pointwise assessments, or in terms of some norm [82].

## Finite Element Equations for Elastic Contact

Using the concepts of the previous section, it is instructive to examine the finite element equations that result by applying contact constraints to the governing equations of linear elasticity. The biphasic contact finite element formulation will be selected by examining each of these formulations for computational efficiency and constraint satisfaction in the context of the linear biphasic theory. These formulations will begin with the statement of the potential energy for an elastic continuum,

$$\Pi(\mathbf{u}) = \frac{1}{2} \int_{\Omega} \boldsymbol{\varepsilon}^T \mathbf{D} \boldsymbol{\varepsilon} \, d\Omega - \int_{\Gamma_t} \mathbf{u}^T \bar{\mathbf{t}} \, d\Gamma, \quad (3.13)$$

and the Principal of Minimum Potential Energy which states that the desired displacement solution is the one which minimizes  $\Pi(\mathbf{u})$ . This variational formulation is equivalent to the following system of equations:

$$\nabla \sigma = 0 \quad \text{in } \Omega, \quad (3.14a)$$

$$\sigma \mathbf{n} = \bar{\mathbf{t}} \quad \text{on } \Gamma_t, \quad (3.14b)$$

where the constitutive relation, strain-displacement law and displacement boundary condition are assumed satisfied *a priori*. In addition, this section will consider the case of perfectly bonded contact, where there is no tangential motion on the contact surface. This condition would describe a solid, inhomogeneous body subjected to boundary tractions and/or displacements, or quasi-static indentation of a flat layer by a spherical punch, for example. Zienkiewicz and Taylor treat this problem for various mixed and hybrid formulations in chapter thirteen of their text [165]. For this case, the boundary conditions to satisfy on the surface  $\Gamma_c$  are

$$\mathbf{u}^A + \mathbf{x}^A - (\mathbf{u}^B + \mathbf{x}^B) = 0 \quad \text{on } \Gamma_c, \quad (3.15a)$$

$$\sigma^A \mathbf{n}^A + \sigma^B \mathbf{n}^B = 0 \quad \text{on } \Gamma_c, \quad (3.15b)$$

where Eq. (3.15a) indicates that there is no relative motion once points have come into contact and Eq. (3.15b) represents continuity of the traction vector.

### Penalty Element

A penalty contact formulation follows from Eqns. (3.2), (3.13) and (3.15a). As is common in variational formulations, the kinematic portion of the contact boundary conditions, Eq. (3.15a), is introduced into the functional, and the traction condition, Eq. (3.15b), results as a natural condition. The constrained functional is

$$\begin{aligned} \Pi_P(\mathbf{u}) = & \frac{1}{2} \int_{\Omega} \boldsymbol{\varepsilon}^T \mathbf{D} \boldsymbol{\varepsilon} \, d\Omega - \int_{\Gamma_t} \mathbf{u}^T \bar{\mathbf{t}} \, d\Gamma + \\ & + \beta \int_{\Gamma_c} (\mathbf{u}^A + \mathbf{x}^A - (\mathbf{u}^B + \mathbf{x}^B))^T (\mathbf{u}^A + \mathbf{x}^A - (\mathbf{u}^B + \mathbf{x}^B)) \, d\Gamma, \end{aligned} \quad (3.16)$$

which has as Euler equations Eqns. (3.14) and

$$\sigma^A \mathbf{n}^A = -\sigma^B \mathbf{n}^B = -2\beta (\mathbf{u}^A + \mathbf{x}^A - (\mathbf{u}^B + \mathbf{x}^B)) \quad \text{on } \Gamma_c. \quad (3.17)$$

Note that as  $\beta \rightarrow \infty$  the kinematic constraint from Eq. (3.15a) is satisfied, providing the stresses remain bounded. For finite values of the penalty number the contact traction is proportional to the violation of the constraint, that is, the gap between the contacting surfaces.

Introducing the strain-displacement relation, constitutive relation and a global displacement interpolation of the form

$$\mathbf{u} = \sum N_a \mathbf{q}_a \quad (3.18)$$

into Eq. (3.16), and then taking the variation with respect to displacement, results in the following matrix equations

$$\begin{bmatrix} \mathbf{K}^A + 2\beta \mathbf{Q}^{AA} & -2\beta \mathbf{Q}^{AB} \\ -2\beta \mathbf{Q}^{BA} & \mathbf{K}^B + 2\beta \mathbf{Q}^{BB} \end{bmatrix} \begin{Bmatrix} \mathbf{q}^A \\ \mathbf{q}^B \end{Bmatrix} = \begin{Bmatrix} \mathbf{f}^A \\ \mathbf{f}^B \end{Bmatrix} - 2\beta \begin{bmatrix} \mathbf{Q}^{AA} & \mathbf{Q}^{AB} \\ -\mathbf{Q}^{BA} & \mathbf{Q}^{BB} \end{bmatrix} \begin{Bmatrix} \mathbf{x}^A \\ \mathbf{x}^B \end{Bmatrix}. \quad (3.19)$$

The matrices  $\mathbf{K}$  and vectors  $\mathbf{f}$  are the familiar stiffness and force terms from linear elastostatics, while the contact matrices are given by

$$\mathbf{Q}^{\gamma\delta} = \int_{\Gamma_c} \mathbf{N}^\gamma \mathbf{T} \mathbf{N}^\delta d\Omega, \quad \gamma, \delta = A, B. \quad (3.20)$$

The additional forcing term arises from the initial separation of degrees of freedom on opposite sides of the contact surface.

It is important to recognize that the contact matrices are very sparse, since only a small fraction of the degrees of freedom lie on the contact surface. Because of this sparsity, and the contribution of the penalty number to diagonal elements in the left hand side matrix, numerical ill-conditioning can result in this formulation. A static condensation step, or an intelligent ordering of the degrees of freedom, would group the penalty contributions and provide a more efficient form of the matrix equations. Iterations must be performed to determine the correct contact surface, thus the system of equations will be solved repeatedly, updating the contact surface each time until the Kuhn-Tucker relations, Eqns. (2.43), are satisfied. While this formulation does not increase the number of unknowns in the problem, when a linear problem is considered with a direct solver, there is considerable additional effort in the solution step. This is in part due to the increased bandwidth profile introduced by the contact matrices, and also due to repeated formation and solution of the stiffness and contact matrices for each contact iteration.

### Lagrange Multiplier Element

In a similar fashion, the Lagrange multiplier contact formulation follows from Eqns. (3.7a), (3.13) and (3.15a). The constrained functional is

$$\Pi_P(\mathbf{u}) = \frac{1}{2} \int_{\Omega} \varepsilon^T \mathbf{D} \varepsilon \, d\Omega - \int_{\Gamma_t} \mathbf{u}^T \bar{\mathbf{t}} \, d\Gamma - \int_{\Gamma_c} \lambda^T (\mathbf{u}^A + \mathbf{X}^A - (\mathbf{u}^B + \mathbf{X}^B)) \, d\Gamma, \quad (3.21)$$

where  $\lambda$  is a vector of Lagrange multipliers of length  $n_{sd}$ . Rendering the functional stationary results in Eqns. (3.14) and

$$\mathbf{u}^A + \mathbf{X}^A - (\mathbf{u}^B + \mathbf{X}^B) = 0, \text{ on } \Gamma_c, \quad (3.22a)$$

$$\sigma^A \mathbf{n}^A = -\sigma^B \mathbf{n}^B = \lambda, \text{ on } \Gamma_c \quad (3.22b)$$

as Euler equations. This formulation requires interpolations for displacement in the domain  $\Omega$  and for the multiplier,  $\lambda$ , on the surface  $\Gamma_c$ . These interpolations lead to the following system of equations:

$$\begin{bmatrix} \mathbf{K}^A & 0 & \mathbf{Q} \\ 0 & \mathbf{K}^B & -\mathbf{Q} \\ \mathbf{Q}^T & -\mathbf{Q}^T & 0 \end{bmatrix} \begin{Bmatrix} \mathbf{q}^A \\ \mathbf{q}^B \\ \mathbf{r} \end{Bmatrix} = \begin{Bmatrix} \mathbf{f}^A \\ \mathbf{f}^B \\ \mathbf{Q}^T(\mathbf{X}^A - \mathbf{X}^B) \end{Bmatrix}, \quad (3.23)$$

where  $\mathbf{r}$  is the vector of degrees of freedom associated with the interpolation for  $\lambda$  and the contact matrix has the form

$$\mathbf{Q} = \int_{\Gamma_c} \mathbf{M}^T \mathbf{N} \, d\Omega. \quad (3.24)$$

The matrix  $\mathbf{M}$  is the interpolation for the multiplier on  $\Gamma_c$ , and should be chosen to have as many independent coefficients as the interpolation of the constraint, Eq. (3.15a). With fewer coefficients, the constraint would not be adequately enforced. For example, in the

case of quadratic displacement elements this would dictate quadratic multipliers as well. This is perhaps counter-intuitive, since the Euler equations identified the multiplier as a traction, which, if computed from the displacement interpolation, would be piecewise linear for this element.

As with the penalty method, there is an additional forcing term in the final matrix equations. The system in Eq. (3.23) is larger than Eq. (3.19), however, by the number of interpolation coefficients required for the multiplier. Observe also that the system of equations is semi-definite, due to the zero matrix on the diagonal. For direct equation solvers, this can be accommodated through the use of the Crout factorization [66]. Again, an intelligent equation numbering will reduce the bandwidth of the contact matrices. In contrast to the penalty method, though, the contact contributions to the left hand side matrix can be updated without modifying the stiffness contributions. For linear problems this can result in a savings of CPU time, since a large portion of the left hand side can be factored in advance and retained throughout the calculations.

### Augmented Lagrangian Element

Applying the canonical augmented Lagrangian functional, Eq. (3.9), to this linear elastic contact problem gives the following functional

$$\begin{aligned} \Pi_{AL}(\mathbf{u}) = & \frac{1}{2} \int_{\Omega} \boldsymbol{\varepsilon}^T \mathbf{D} \boldsymbol{\varepsilon} d\Omega - \int_{\Gamma_t} \mathbf{u}^T \bar{\mathbf{t}} d\Gamma - \int_{\Gamma_c} \lambda^T (\mathbf{u}^A + \mathbf{x}^A - (\mathbf{u}^B + \mathbf{x}^B)) d\Gamma + \\ & + \beta \int_{\Gamma_c} (\mathbf{u}^A + \mathbf{x}^A - (\mathbf{u}^B + \mathbf{x}^B))^T (\mathbf{u}^A + \mathbf{x}^A - (\mathbf{u}^B + \mathbf{x}^B)) d\Gamma, \end{aligned} \quad (3.25)$$

which has as Euler equations Eqns. (3.14) and

$$\sigma^A \mathbf{n}^A = \lambda - 2\beta (\mathbf{u}^A + \mathbf{x}^A - (\mathbf{u}^B + \mathbf{x}^B)) \text{ on } \Gamma_c, \quad (3.26a)$$

$$\sigma^B \mathbf{n}^B = -\lambda + 2\beta (\mathbf{u}^A + \mathbf{x}^A - (\mathbf{u}^B + \mathbf{x}^B)) \text{ on } \Gamma_c. \quad (3.26b)$$

Recall that the multiplier is considered a known vector of length  $n_{sd}$ , and will be iterated to convergence. In the limit  $\beta \rightarrow \infty$  the displacement constraint will be satisfied. The Euler equations also indicate that, for finite  $\beta$ , as the degree of constraint satisfaction increases, the multipliers can be identified as contact traction, and that the traction will be continuous on  $\Gamma_c$ . Interpolating the displacements leads to the following matrix equations,

$$\begin{bmatrix} \mathbf{K}^A + 2\beta \mathbf{Q}^{AA} & -2\beta \mathbf{Q}^{AB} \\ -2\beta \mathbf{Q}^{BA} & \mathbf{K}^B + 2\beta \mathbf{Q}^{BB} \end{bmatrix} \begin{Bmatrix} \mathbf{q}^A \\ \mathbf{q}^B \end{Bmatrix} = \begin{Bmatrix} \mathbf{f}^A + \mathbf{R}^A \\ \mathbf{f}^B - \mathbf{R}^B \end{Bmatrix} - 2\beta \begin{bmatrix} \mathbf{Q}^{AA} & \mathbf{Q}^{AB} \\ \mathbf{Q}^{BA} & \mathbf{Q}^{BB} \end{bmatrix} \begin{Bmatrix} \mathbf{x}^A \\ \mathbf{x}^B \end{Bmatrix}, \quad (3.27)$$

where the current multipliers appear as part of a forcing term on the right hand side,

$$\mathbf{R}^\gamma = \int_{\Gamma_c} \mathbf{N}^{\gamma T} \lambda \, d\Gamma \quad \gamma = A, B. \quad (3.28)$$

These equations are nearly identical in form to those of the penalty formulation, with the addition of the vectors  $\mathbf{R}^\gamma$ . Because of this similarity, implementation details relating to computational efficiency are also the same. Recall from the one degree of freedom example that the choice of penalty in the augmented Lagrangian can be significantly smaller than that in the penalty method. Thus, one would expect that the performance of the augmented Lagrangian would be much better than the penalty method, because of the better numerical conditioning.

One of the advantages of the iterative scheme is that it restores a quadratic convergence rate to the solution [58,83]. This implies that the usual iterative procedure to determine the correct contact surface will now converge with a guaranteed quadratic rate.



In nonlinear problems, where a nonlinear iteration procedure is nested within the contact iterations, both loops will have this property, greatly reducing the computational effort.

### Hybrid Contact Elements

An assumed stress hybrid approach to generating finite element equations often results in an element more efficient than the corresponding displacement-based formulation [16,106,140]. When beginning from a variational principle, the displacement elements will use the potential energy, Eq. (3.13), while the hybrid elements use the complementary energy. As the name implies, the assumed stress element interpolates the stress field within the element, as well as the displacement on the boundary of the element. While the methods used to derive each element are different, the matrix form of the stiffness equations is the same.

In the same way that a penalty term or Lagrange multiplier is appended to the potential energy to enforce the contact boundary conditions, the complementary energy functional can be modified to enforce constraints on the field variables. Any of the three methods described above could be implemented with the hybrid functional. For example, a hybrid contact element formulated with Lagrange multipliers will have matrix equations of the same form as the displacement-based contact element (see, for example, [76]). Thus, computational performance of the hybrid contact element is similar to the displacement-based elements with regard to the treatment of contact. Any performance advantages of one method over the other for the non-contact elements will be retained.

There are several features of the hybrid formulations that make it attractive for constrained media problems, in particular for biphasic elements [157]. This section will not present a full derivation of the hybrid contact elements, but rather, recognizes the

similarity in the resulting finite element equations. To complete the process of evaluating possible formulations for the biphasic contact finite element, the hybrid contact elements will be considered using the information presented in the previous sections, and information in the literature on hybrid finite elements [16,76,110,113,114].

## **Selection of the Biphasic Element**

There are two important considerations in choosing a biphasic contact finite element. First is the means by which the mixture continuity relation, Eq. (2.37), will be introduced into the formulation. As has been alluded to, finite element formulations for constrained media problems can present significant difficulty when choosing the finite element interpolations [90,108]. Second is the method of enforcing the contact boundary conditions, Eqns. (2.40), the alternatives to which have been described in this chapter.

### **Selecting the Element Formulation**

Regarding the continuity relation, there have been four methods reported in the literature for biphasic finite elements: the penalty formulation of Suh *et al.* [142,146], the mixed-penalty formulation of Spilker and Maxian [139], the hybrid formulation of Vermilyea and Spilker [156] and the pressure-velocity formulation of Oomens *et al.* [112] or the similar pressure-displacement formulation by Wayne *et al.* [159]. A recent paper suggests using the augmented Lagrangian approach to enforce the continuity relation for a single-phase continuum [161], although this method has not yet been used with the biphasic equations.

The penalty formulation of Suh was implemented for two dimensional problems with a four-node quadrilateral. He notes that for distorted quadrilaterals, this element

behaves poorly [145]. In addition, the mean dilatational formulation used for that element is not readily extensible to higher order elements, which are often desirable in constrained media problems. Maxian indicates these shortcomings as the motivation to develop the mixed-penalty element [91]. There is also strong motivation to use simplex elements when considering mesh generation on realistic geometries [122,137,141], or when employing adaptive mesh updates [39]. The pressure-velocity elements are quite attractive, since they replace the unknown fluid velocity in the formulations by the scalar pressure field, reducing the size of the assembled matrix equations. In Wayne's formulation, she notes that the solution can exhibit spatial oscillations near a loaded surface at early times in the deformation [159]. While these oscillations do diminish in time, they can have significant effects for nonlinear problems, or on solutions that take advantage of  $h$ -adaptive mesh enrichment.

The hybrid method appears quite attractive, since it does not require the user to select a penalty parameter to enforce the continuity constraint. In addition, Vermilyea indicates a much better convergence rate for the two dimensional hybrid element as compared with the mixed-penalty triangle for an uniaxial confined compression problem [155]. There are disadvantages, however, most significant being that the hybrid formulation requires a strain-stress law, as opposed to a stress-strain law for displacement-based elements. For linear materials it is straightforward to invert the material property matrix, but for nonlinear materials one must formulate the inverse of the Helmholtz free energy function. This is a significant undertaking for, as described in Chapter II, there are numerous axioms which must be satisfied. While constitutive laws of this form could be constructed, experimentally curve fit to determine their parameters and tested to ensure physically plausible behaviour, one does not presently exist so biphasic studies to date with the hybrid element have been limited to linear analysis.

With regard to numerical performance, the hybrid element does require larger amounts of CPU time to assemble, factor and solve the system of equations. Vermilyea reports between one and three times more effort spent on these tasks for the three dimensional hybrid element, as compared with the mixed-penalty element [155]. There is also an increase in system bandwidth by as much as a factor of two, adversely effecting the solution time and storage requirements.

For a confined compression stress relaxation problem, Vermilyea reports a convergence rate of 2.6 for fluid velocity in a two-dimensional element [155]. These tests were conducted on regular meshes of triangles. Using irregular meshes, Maxian found a convergence rate of 1.0 for fluid velocity in the mixed-penalty triangle [91]. More recently, Almeida has reported convergence studies for a confined compression creep problem with both the mixed-penalty and velocity-pressure formulations [6]. The mixed-penalty triangle converges with a rate of 2 for fluid velocity, for either regular or irregular meshes. With the velocity-pressure formulation, the rate was less than this, perhaps indicative of over constraint for this particular mesh [66].

With these observations, then, the mixed-penalty element will be chosen as the basis on which to formulate the biphasic contact element. For reference, a complete presentation of the finite element equations is given by Spilker and Maxian. This provides an accurate, efficient element which can be extended to nonlinear contact analysis in the future, and which has been successfully extended to model all relevant nonlinear mechanics for the single-region problem [6]. In addition, the element has been implemented for both triangles and tetrahedra, allowing existing  $h$ -adaptive mesh enrichment schemes to be coupled to this formulation [20,39], providing the necessary resolution of moving contact interfaces.

## Selecting the Contact Treatment

With the element formulation now determined, each of the methods of enforcing contact constraints will be evaluated with respect to this element. Two pieces of information weigh heavily in determining the efficiency of the candidate contact formulations. First, the present implementation considers only the *linear*, time-dependent form of the biphasic equations. Second, the computer implementation will utilize a direct equation solution strategy, on a serial computer architecture.

While there are numerous successful penalty contact finite elements (for example, [24,67,74]), the ill-conditioning due to the penalty term may prove problematic. This is especially true in the presence of a penalty term to enforce the continuity relation. Also, considering the time-dependent nature of the biphasic problem, and the use of a direct solution strategy, the structure of the penalty equations will entail excessive calculations.

For nearly the same reasons, the augmented Lagrange approach is also discarded. As noted previously, the form of the matrix equations for both the penalty and augmented Lagrange methods is the same, which results in the same conclusion concerning repeated solutions in this time-dependent problem. Unfortunately, for a linear equation set, the quadratic convergence of the multipliers does not provide any significant improvement in the computational effort.

Thus, the biphasic contact finite element will be implemented with a mixed-penalty treatment of the incompressibility and a Lagrange multiplier treatment of the contact constraints. Since there is no potential energy functional for the biphasic theory, it will be necessary to formulate the element using a Galerkin weighted residual method. The contact contribution due to the Lagrange multipliers will also be introduced into the

weighted residual. Observe that if the resulting finite element equations are symmetric, a variational principle does exist, and that its Euler equations and natural boundary conditions are those introduced into the weighted residual statement [165]. This formulation is the subject of the subsequent chapter.

# Chapter IV: The Mixed-Penalty Lagrange Multiplier Formulation

## Introduction

With the statement of the governing equations and boundary conditions for the biphasic contact problem, Eqns. (2.37-43), and the element formulation specified in Chapter III, it is straightforward to develop the finite element equations. This derivation will be based on a Galerkin weighted residual statement, and will closely follow the presentation given by Spilker and Maxian [139]. Attention is focused on the Lagrange multiplier treatment of the contact boundary conditions in the context of a weighted residual method. A matrix form of the weighted residual statement is developed, which is general and can be interpreted for any two- or three-dimensional interpolation. The formulation is then specialized for a quadratic velocity interpolation over a triangular element.

## Weighted Residual Statement

The finite element method has a rich history which began when researchers in the 1950's began to apply relaxation and approximation methods to structural problems (see, for example, [165] for a history of the method). A tremendous mathematical formalism has been developed since then, which allows nearly any system of equations to be approximated. Before the biphasic finite element equations can be developed, however, two important steps must be taken. First, the mixture continuity equation and contact boundary conditions must be modified to facilitate the numerical procedure. Second, the weighted residual method requires a precise mathematical statement of the function spaces

in which solutions will be sought. Then a weak form of the problem can be formulated, to which the numerical approximation will be applied.

## Preliminaries

The weighted residual statement is constructed from the governing equations and natural boundary conditions in each domain, and from the contact boundary conditions. In particular, the solid and fluid momentum equations, a penalized form of the mixture continuity relation and the traction boundary conditions will be approximated, while the constitutive laws, strain-displacement relations and essential boundary conditions will be exactly satisfied. The method begins by developing a penalized form of the continuity equation [45,139],

$$\left( \phi^s v_i^s + \phi^f v_i^f \right)_{,i} + \frac{p}{\beta} = 0, \quad (4.1)$$

which in the limit  $\beta \rightarrow \infty$  is equivalent to the original continuity relation presented in Chapter II. Suh developed a methodology to estimate the penalty parameter for the biphasic equations [145]. He formed the total momentum as the sum of the solid and fluid momenta, Eq. (2.38), and substituted from the constitutive laws, Eqns. (2.39), to obtain an expression in terms of displacement, velocity and pressure. He then eliminated pressure by using Eq. (4.1). Specializing this relation for a one-dimensional problem, he found the penalty parameter was proportional to machine accuracy, a reference time and the equilibrium modulus of the solid phase, and inversely proportional to volume fraction. He later demonstrated that for linear problems, the penalty parameter can be varied over approximately four orders of magnitude with no adverse effect on the solution.

To introduce the contact boundary conditions into the weighted residual statement, and still retain the properties of a Lagrange multiplier method, it is necessary to redefine



the kinetic contact relations. For example, compare the contact continuity relations developed in Chapter II, Eqns. (2.40), with the Euler equations for the Lagrange functional for elastic contact in Chapter III, Eqns. (3.22). Observe that the kinematic constraint appears directly as an Euler equation, but that kinetic constraint is replaced by two equivalent relations. These indicate that the multiplier is simultaneously equal to traction on side 'A' of the interface and the negative of traction on side 'B'. The Euler equations can be considered defining relations for the multiplier which have the additional effect of producing continuous traction on the interface.

In the absence of an energy functional in the biphasic case, it is still possible to develop finite element equations which represent a Lagrange multiplier constraint operation. As stated previously, if the finite element equations which result from a weighted residual statement are symmetric, one can conclude that a functional does exist which produces the same equations [165]. In addition, the Euler equations of this unknown functional are precisely those equations introduced into the weighted residual statement. Thus, in this formulation, the kinetic continuity relations will be rewritten to define the multipliers according to the analogy above. For the biphasic case two scalar multipliers will be required: one each for the solid and fluid kinetic contact continuity relations. From Eq. (2.40c) define  $\lambda^f$  on the contact surface and require:

$$\lambda^f = \frac{\sigma_{ij}^f n_i^A n_j^A}{\phi f^A} \quad \text{on } \Omega^A \cap \Gamma_c, \quad (4.2a)$$

$$\lambda^f = \frac{\sigma_{ij}^f n_i^B n_j^B}{\phi f^B} \quad \text{on } \Omega^B \cap \Gamma_c. \quad (4.2b)$$

In a similar manner, define  $\lambda^s$  on the contact surface from Eq. (2.40d):

$$\lambda^s = (\sigma_{ij}^{sA} n_i^A n_j^A) - \frac{\phi^{sA}}{\phi^{fA}} (\sigma_{ij}^{fA} n_i^A n_j^A) \quad \text{on } \Omega^A \cap \Gamma_c, \quad (4.3a)$$

$$\lambda^s = (\sigma_{ij}^{sB} n_i^B n_j^B) - \frac{\phi^{sB}}{\phi^{fB}} (\sigma_{ij}^{fB} n_i^B n_j^B) \quad \text{on } \Omega^B \cap \Gamma_c. \quad (4.3b)$$

Note that  $\lambda^s$  and  $\lambda^f$  are not independent in body 'A' and body 'B', but rather are defined on  $\Gamma_c$  such that they enforce the continuity required by Eqns. (2.40c,d). They become additional variables which must be interpolated in the finite element formulation, and from which the normal components of interface tractions can be recovered.

### Choice of Trial and Test Spaces

The essence of the weighted residual method is to multiply each equation that will be approximated by an arbitrary weighting function, integrate this over the domain where the equation is to be enforced and sum these. For arbitrary weight functions, the resulting weighted sum is equivalent to the governing equations [66]. For the biphasic contact element, three classes of weight, or test, functions are required. These function spaces are defined as follows:

$$\mathcal{V}_v = \left\{ w \mid w \in H^1 \text{ and } w = 0 \text{ on } \Gamma_{vs} \cup \Gamma_{vf} \right\}, \quad (4.4a)$$

$$\mathcal{V}_p = \left\{ w \mid w \in H^0 \right\}, \quad (4.4b)$$

$$\mathcal{V}_c = \left\{ w \mid w \in H^0 \text{ and } w = 0 \text{ on } \Omega \setminus \Gamma_c \right\}, \quad (4.4c)$$

where  $H^s$  are Sobolev spaces equipped with their natural norms. Respectively, these will be spaces of velocity, pressure and contact weight functions. These are, in effect, smoothness requirements on the test functions, and will ensure that the subsequent mathematical manipulations are well defined [70,144]. Additionally, three function spaces for the trial

solutions must be defined as

$$\delta_{v_i}^\alpha = \left\{ w \mid w \in H^1 \text{ and } w = \bar{w} \text{ on } \Gamma_{v_i}^\alpha \right\}, \quad \alpha = s, f, \quad (4.5a)$$

$$\delta_p = \left\{ w \mid w \in H^0 \right\}, \quad (4.5b)$$

$$\delta_c = \left\{ w \mid w \in H^0 \text{ and } w = 0 \text{ on } \Omega \setminus \Gamma_c \right\}. \quad (4.5c)$$

Analogous to the test functions, these are trial spaces for the velocity (or displacement), pressure and multipliers. These definitions require that the trial solutions satisfy the essential boundary conditions, while the velocity weight functions need only satisfy the homogeneous form of the essential boundary conditions. Rigorously, the space of velocities must also be constrained by the kinematic part of the Kuhn-Tucker relations, Eq. (2.43a) [75]. In practice, this requirement is too strong, since the deformed state of the material is unknown in advance. Alternatively, an iterative procedure has been developed which finds solutions satisfying both Eqns. (2.43) and (4.5).

### Development of the Weak Form

A single weighted residual statement will be written as the sum of terms from body 'A', body 'B' and the contact surface, such that

$$G^A + G^B + G^c = 0. \quad (4.6)$$

For clarity, each of these will be presented separately. From body 'A' the contributions to the weighted residual are

$$G^A = \int_{\Omega^A} w_i^{sA} (\sigma_{ij,j}^{sA} + \Pi_i^{sA}) d\Omega + \int_{\Gamma_{ti}^{sA}} h_i^{sA} (\bar{t}_i^{sA} - t_i^{sA}) d\Gamma +$$

$$\begin{aligned}
& + \int_{\Omega^A} w_i^{fA} (\sigma_{ij,j}^{fA} + \Pi_i^{fA}) d\Omega + \int_{\Gamma_{ti}^{fA}} h_i^{fA} (\bar{t}_i^{fA} - t_i^{fA}) d\Gamma + \\
& + \int_{\Omega^A} w^{cA} \left( \left( \phi^{fA} v_i^{fA} + \phi^{sA} v_i^{sA} \right)_{,i} + \frac{p^A}{\beta^A} \right) d\Omega + \\
& + \int_{\Gamma_c} r^{fA} \left( \lambda^f - \frac{\sigma_{ij}^{fA} n_i^A n_j^A}{\phi^{fA}} \right) d\Gamma + \\
& + \int_{\Gamma_c} r^{sA} \left( \lambda^s - (\sigma_{ij}^{sA} n_i^A n_j^A) + \frac{\phi^{sA}}{\phi^{fA}} (\sigma_{ij}^{fA} n_i^A n_j^A) \right) d\Gamma. \tag{4.7}
\end{aligned}$$

Here the requirements on the weight functions are that  $w_i^\alpha \in \vartheta_v$ ,  $h_i^\alpha \in \vartheta_v$ ,  $r^\alpha \in \vartheta_v$  and  $w^c \in \vartheta_p$  for  $\alpha = s, f$ . Trial solutions are restricted to be members of the spaces defined by Eqns. (4.5) as follows:  $v_i^\alpha \in \delta_{v_i}^\alpha$ ,  $p \in \delta_p$  and  $\lambda^\alpha \in \delta_c$ . Observe that Eq. (4.7) contains the definitions of the multipliers given by Eqns. (4.2a) and (4.3a).

To develop the weak form of the weighted residual, terms in the first and third integrals of Eq. (4.7) with the divergence of stress can be rewritten by applying the Divergence Theorem. The first integral becomes

$$\int_{\Omega^A} w_i^{sA} \sigma_{ij,j}^{sA} d\Omega = - \int_{\Omega^A} w_{(i,j)}^{sA} \sigma_{ij}^{sA} d\Omega + \int_{\Gamma^A} w_i^{sA} \sigma_{ij}^{sA} n_j^A d\Gamma, \tag{4.8}$$

where the parentheses surrounding the indices indicate the symmetric part of the tensor. Weight functions are chosen to be members of the spaces in Eqns. (4.4), then, since  $\Gamma^A = \Gamma_{vs}^A \cup \Gamma_{vf}^A \cup \Gamma_{ts}^A \cup \Gamma_{tf}^A \cup \Gamma_c$ , the choice of weight functions will cause the boundary integral in Eq. (4.8) to be zero on  $\Gamma_{vs}^A$  and  $\Gamma_{vf}^A$ . Also if  $w_i^{sA}$  is chosen equal to  $w_i^{sA}$ , portions

of Eq. (4.8) will cancel terms in the second integral of Eq. (4.7). By decomposing the traction vector into its normal and tangential components, and recognizing the tangential component will be zero on  $\Gamma_c$  for the frictionless case considered in this study, the remaining terms will be

$$\int_{\Omega^A} w_i^{sA} \sigma_{ij,j}^{sA} d\Omega = - \int_{\Omega^A} w_{(i,j)}^{sA} \sigma_{ij}^{sA} d\Omega + \int_{\Gamma_c} w_k^{sA} (\sigma_{ij}^{sA} n_j^A n_i^A) n_k^A d\Gamma. \quad (4.9)$$

This last term in Eq. (4.9) can be eliminated by choosing the weight function  $r^{sA} = w_k^{sA} n_k^A$  in Eq. (4.7).

Likewise, applying the same operations to the third integral in Eq. (4.7) and selecting the fluid weight functions  $h_i^{fA} = w_i^{fA}$  and  $r^{fA} = \phi^{fA} w_k^{fA} n_k^A + \phi^{sA} w_k^{sA} n_k^A$ , the term remaining from the divergence theorem applied to this integral will be

$$\int_{\Omega^A} w_i^{fA} \sigma_{ij,j}^{fA} d\Omega = - \int_{\Omega^A} w_{(i,j)}^{fA} \sigma_{ij}^{fA} d\Omega. \quad (4.10)$$

The contributions from body 'B' are similar, and the same steps can be followed to develop a weak form for  $G^B$ . In particular, the requirements for trial and test spaces for the solution and weight functions are the same. Also, the same choices are made for relations between the weight functions after the Divergence Theorem has been applied.

Terms in the weighted residual from the contact surface are

$$\begin{aligned} G^c = & \int_{\Gamma_c} \frac{s^s}{\Delta t \omega} \left( (u_i^{sA} + X_i^{sA}) n_i^A + (u_i^{sB} + X_i^{sB}) n_i^B \right) d\Gamma + \\ & + \int_{\Gamma_c} \frac{s^f}{\Delta t \omega} \left[ \left( \phi^{fA} (u_i^{fA} + X_i^{fA}) + \phi^{sA} (u_i^{sA} + X_i^{sA}) \right) n_i^A + \right. \end{aligned}$$

$$+ \left( \phi^{fB} (u_i^{fB} + X_i^{fB}) + \phi^{sB} (u_i^{sB} + X_i^{sB}) \right) n_i^B d\Gamma \Big], \quad (4.11)$$

and come from Eqns. (2.40a,b). The contact weight factors are restricted to be in  $H^0$ :  $s^\alpha \in \mathcal{V}_c$  for  $\alpha = s, f$ . The decision to scale the scalar weight functions will become apparent after the time discretization. Of course, since this is an arbitrary weight function, the scale factor does not effect the generality of this derivation.

Now the complete weak form of the weighted residual is formed as the sum of the contributions from body 'A', body 'B', and the interface. Multiplying through by negative one at the same time, this becomes

$$\begin{aligned} & \int_{\Omega^A} w_{(i,j)}^{sA} \sigma_{ij}^{sA} d\Omega + \int_{\Omega^B} w_{(i,j)}^{sB} \sigma_{ij}^{sB} d\Omega + \int_{\Omega^A} w_{(i,j)}^{fA} \sigma_{ij}^{fA} d\Omega + \int_{\Omega^B} w_{(i,j)}^{fB} \sigma_{ij}^{fB} d\Omega - \\ & - \int_{\Omega^A} w_i^{sA} \Pi_i^{sA} d\Omega - \int_{\Omega^B} w_i^{sB} \Pi_i^{sB} d\Omega - \int_{\Omega^A} w_i^{fA} \Pi_i^{fA} d\Omega - \int_{\Omega^B} w_i^{fB} \Pi_i^{fB} d\Omega - \\ & - \int_{\Gamma_{t_1}^{sA}} w_i^{sA} t_i^s d\Gamma - \int_{\Gamma_{t_1}^{fA}} w_i^{fA} t_i^f d\Gamma - \int_{\Gamma_{t_1}^{sB}} w_i^{sB} t_i^s d\Gamma - \int_{\Gamma_{t_1}^{fB}} w_i^{fB} t_i^f d\Gamma - \\ & - \int_{\Omega^A} w^{cA} \left( (\phi^{fv_i} f^A)_{,i} + (\phi^{sv_i} s^A)_{,i} + \frac{p^A}{\beta^A} \right) d\Omega - \int_{\Omega^B} w^{cB} \left( (\phi^{fv_i} f^B)_{,i} + (\phi^{sv_i} s^B)_{,i} + \frac{p^B}{\beta^B} \right) d\Omega - \\ & - \int_{\Gamma_c} \lambda^f n_k^A (\phi^{sA} w_k^{sA} + \phi^{fA} w_k^{fA}) d\Gamma - \int_{\Gamma_c} \lambda^s n_k^A w_k^{sA} d\Gamma - \\ & - \int_{\Gamma_c} \lambda^f n_k^B (\phi^{sB} w_k^{sB} + \phi^{fB} w_k^{fB}) d\Gamma - \int_{\Gamma_c} \lambda^s n_k^B w_k^{sB} d\Gamma - \end{aligned}$$

$$\begin{aligned}
& - \int_{\Gamma_c} \frac{s^s}{\Delta t \omega} \left[ (u_i^{sA} + X_i^{sA}) n_i^A + (u_i^{sB} + X_i^{sB}) n_i^B \right] d\Gamma - \\
& - \int_{\Gamma_c} \frac{s^f}{\Delta t \omega} \left[ \left( \phi^{fA} (u_i^{fA} + X_i^{fA}) + \phi^{sA} (u_i^{sA} + X_i^{sA}) \right) n_i^A + \right. \\
& \left. + \left( \phi^{fB} (u_i^{fB} + X_i^{fB}) + \phi^{sB} (u_i^{sB} + X_i^{sB}) \right) n_i^B \right] d\Gamma = 0.
\end{aligned} \tag{4.12}$$

## Finite Element Matrix Equations

At this stage the weak form, Eq. (4.12), is a statement equivalent to the governing equations presented in Chapter II, Eqns. (2.37-43), and no approximations have been introduced. The next step is to choose finite dimensional counterparts to the function spaces given in Eqns. (4.4-5), which will suggest the numerical approximation. This will be conducted in a formal way, producing a set of matrix equations valid for acceptable choices of interpolations in two or three dimensions. The final step is to particularize the interpolations for a six-node, triangular element.

### Element Interpolations

To write Eq. (4.12) in matrix form the domain is divided into elements and the kinematic variables, pressure, Lagrange multipliers ( $\lambda^s$  and  $\lambda^f$ ) and weight functions are interpolated in terms of their element nodal values, with subscript 'e' indicating the element number. The interpolations within element 'e' are chosen as follows. Solid and fluid velocity are interpolated with functions,  $N \in \delta_{v\alpha}^h \subset \delta_{v\alpha}$ , where the superscript 'h' refers to the finite dimensional subset. The form of the interpolation for velocity is

$$v^{\alpha\gamma} = N v_e^{\alpha\gamma}, \quad \alpha = s, f \quad \gamma = A, B, \tag{4.13a}$$

and for solid displacement is

$$\mathbf{u}^{s\gamma} = \mathbf{N} \mathbf{u}_e^{s\gamma}, \quad \gamma = A, B, \quad (4.13b)$$

where the coefficients  $\mathbf{u}_e^{s\gamma}$  are related to  $\mathbf{v}_e^{s\gamma}$  by a time derivative. The velocity weight functions which, for a Galerkin weighted residual method, have the same polynomial form as the velocities, are interpolated with functions  $\mathbf{N} \in \mathcal{V}_v^h \subset \mathcal{V}_v$  as

$$\mathbf{w}^{\alpha\gamma} = \mathbf{N} \mathbf{w}_e^{\alpha\gamma}, \quad \alpha = s, f \quad \gamma = A, B. \quad (4.13c)$$

Referring to the definitions of the spaces in Eqns. (4.4-5), the only difference in the interpolations for the velocity and its weight functions are at locations where essential boundary conditions are specified. This has the effect of removing as independent equations those corresponding to the constrained degrees of freedom, and producing additional forcing terms related to the essential conditions. With this recognized, the slight abuse in notation of using the same symbol for both the velocity and its weight function will be allowed. In the computer implementation, this important distinction is properly accounted for by an element-level constraint operation. Pressure is interpolated with functions  $N_p \in \delta_p^h \subset \delta_p$  as

$$p^\gamma = N_p p_e^\gamma, \quad \gamma = A, B, \quad (4.13d)$$

and its weight function with  $N_p \in \mathcal{V}_p^h \subset \mathcal{V}_p$  as

$$w^{c\gamma} = N_p w_e^{c\gamma}, \quad \gamma = A, B. \quad (4.13e)$$

Each of these two interpolations has a lower order continuity than the velocity. The solid and fluid multipliers, whose interpolant is non-zero only on the contact surface, are interpolated with functions  $\mathbf{M} \in \delta_c^h \subset \delta_c$  as



$$\lambda^\alpha = \mathbf{M} \lambda_e^\alpha, \quad \alpha = s, f, \quad (4.13f)$$

and the corresponding weight function with  $\mathbf{M} \in \mathcal{V}_c^h \subset \mathcal{V}_c$  as

$$s^\alpha = \mathbf{M} s_e^\alpha, \quad \alpha = s, f. \quad (4.13g)$$

Element reference coordinates, required in the kinematic contact continuity relations, are interpolated in the same way as displacement,

$$\mathbf{X}^{\alpha\gamma} = \mathbf{N} \mathbf{X}_e^{\alpha\gamma}, \quad \alpha = s, f \quad \gamma = A, B. \quad (4.13h)$$

Last is an interpolation for the known volume fraction,

$$\phi^{\alpha\gamma} = \tilde{\mathbf{N}} \phi_e^{\alpha\gamma}, \quad \alpha = s, f \quad \gamma = A, B, \quad (4.13i)$$

enabling the numerical calculation of the gradient of volume fraction within the finite element program. The interpolation matrix  $\tilde{\mathbf{N}}$  would typically contain the same polynomials as  $\mathbf{N}$ , though the ordering within the matrix is different.

At this time the constitutive relations, Eqns. (2.39), are substituted into Eq. (4.12), which necessitates several other definitions. Strain and strain rate are defined as the symmetric part of the gradient of solid displacement and fluid velocity, respectively, and are interpolated as,

$$\varepsilon^s = \nabla^s \mathbf{N} \mathbf{u}_e^s = \mathbf{B} \mathbf{u}_e^s \quad (4.14a)$$

$$\dot{\varepsilon}^f = \nabla^s \mathbf{N} \mathbf{v}_e^f = \mathbf{B} \mathbf{v}_e^f, \quad (4.14b)$$

with  $\nabla^s$  the symmetric gradient operator. Similar operations are performed for the symmetric gradient of the weighting functions. The gradient of volume fraction,

$$\nabla \phi^{\alpha\gamma} = \nabla \tilde{\mathbf{N}} \phi_e^{\alpha\gamma} = \tilde{\mathbf{B}} \phi_e^{\alpha\gamma}, \quad \alpha = s, f \quad \gamma = A, B, \quad (4.15a)$$

is required in terms coming from the momentum exchange and continuity relation. Because the mixture is saturated, gradients of the solid and fluid volume fractions are related,

$$\nabla \phi^f \gamma = \nabla (1 - \phi^s \gamma) = -\nabla \phi^s \gamma, \quad \gamma = A, B. \quad (4.15b)$$

In the finite element method, a reduced index notation will be used for stress and strain, where the independent terms of the symmetric tensors are arranged in a vector. To account for this, the vector  $\mathbf{m}$  is defined as the reduced index form of the Kronecker delta operator, and the fourth rank tensors of material properties are redefined accordingly.

With  $n_{el}$  defined to be the total number of finite elements in body 'A' and body 'B', then substituting the interpolations into Eq. (4.12), the following matrix form of the weighted residual results (note that the terms are in the same order as in Eq. (4.12)),

$$\begin{aligned} & \sum_{e=1}^{n_{el}} \left\{ \mathbf{w}_e^{sA^T} \left( -\phi^{sA} \int_{\Omega_e^A} \mathbf{B}^T \mathbf{m}^T \mathbf{N}_p \, d\Omega \, \mathbf{p}_e^A + \int_{\Omega_e^A} \mathbf{B}^T \mathbf{D}^{sA} \mathbf{B} \, d\Omega \, \mathbf{u}_e^{sA} \right) + \right. \\ & \quad + \mathbf{w}_e^{sB^T} \left( -\phi^{sB} \int_{\Omega_e^B} \mathbf{B}^T \mathbf{m}^T \mathbf{N}_p \, d\Omega \, \mathbf{p}_e^B + \int_{\Omega_e^B} \mathbf{B}^T \mathbf{D}^{sB} \mathbf{B} \, d\Omega \, \mathbf{u}_e^{sB} \right) + \\ & \quad + \mathbf{w}_e^{fA^T} \left( -\phi^{fA} \int_{\Omega_e^A} \mathbf{B}^T \mathbf{m}^T \mathbf{N}_p \, d\Omega \, \mathbf{p}_e^A + \int_{\Omega_e^A} \mathbf{B}^T \mathbf{D}^{fA} \mathbf{B} \, d\Omega \, \mathbf{v}_e^{fA} \right) + \\ & \quad \left. + \mathbf{w}_e^{fB^T} \left( -\phi^{fB} \int_{\Omega_e^B} \mathbf{B}^T \mathbf{m}^T \mathbf{N}_p \, d\Omega \, \mathbf{p}_e^B + \int_{\Omega_e^B} \mathbf{B}^T \mathbf{D}^{fB} \mathbf{B} \, d\Omega \, \mathbf{v}_e^{fB} \right) \right\}. \end{aligned}$$

$$\begin{aligned}
& - \mathbf{w}_e^{sA^T} \left( \int_{\Omega_e^A} \mathbf{N}^T \tilde{\mathbf{B}}_{\phi_e}^{sA} \mathbf{N}_p d\Omega \mathbf{p}_e^A + \int_{\Omega_e^A} \mathbf{N}^T \mathbf{K}^A \mathbf{N} d\Omega \mathbf{v}_e^{fA} - \int_{\Omega_e^A} \mathbf{N}^T \mathbf{K}^A \mathbf{N} d\Omega \mathbf{v}_e^{sA} \right) - \\
& - \mathbf{w}_e^{sB^T} \left( \int_{\Omega_e^B} \mathbf{N}^T \tilde{\mathbf{B}}_{\phi_e}^{sB} \mathbf{N}_p d\Omega \mathbf{p}_e^B + \int_{\Omega_e^B} \mathbf{N}^T \mathbf{K}^B \mathbf{N} d\Omega \mathbf{v}_e^{fB} - \int_{\Omega_e^B} \mathbf{N}^T \mathbf{K}^B \mathbf{N} d\Omega \mathbf{v}_e^{sB} \right) - \\
& - \mathbf{w}_e^{fA^T} \left( - \int_{\Omega_e^A} \mathbf{N}^T \tilde{\mathbf{B}}_{\phi_e}^{sA} \mathbf{N}_p d\Omega \mathbf{p}_e^A - \int_{\Omega_e^A} \mathbf{N}^T \mathbf{K}^A \mathbf{N} d\Omega \mathbf{v}_e^{fA} + \int_{\Omega_e^A} \mathbf{N}^T \mathbf{K}^A \mathbf{N} d\Omega \mathbf{v}_e^{sA} \right) - \\
& - \mathbf{w}_e^{fB^T} \left( - \int_{\Omega_e^B} \mathbf{N}^T \tilde{\mathbf{B}}_{\phi_e}^{sB} \mathbf{N}_p d\Omega \mathbf{p}_e^B - \int_{\Omega_e^B} \mathbf{N}^T \mathbf{K}^B \mathbf{N} d\Omega \mathbf{v}_e^{fB} + \int_{\Omega_e^B} \mathbf{N}^T \mathbf{K}^B \mathbf{N} d\Omega \mathbf{v}_e^{sB} \right)
\end{aligned}$$

$$- \mathbf{w}_e^{sA^T} \int_{\Gamma_{t_e}^{sA}} \mathbf{N}^T \tilde{\mathbf{t}}^{sA} d\Gamma - \mathbf{w}_e^{fA^T} \int_{\Gamma_{t_e}^{fA}} \mathbf{N}^T \tilde{\mathbf{t}}^{fA} d\Gamma -$$

$$- \mathbf{w}_e^{sB^T} \int_{\Gamma_{t_e}^{sB}} \mathbf{N}^T \tilde{\mathbf{t}}^{sB} d\Gamma - \mathbf{w}_e^{fB^T} \int_{\Gamma_{t_e}^{fB}} \mathbf{N}^T \tilde{\mathbf{t}}^{fB} d\Gamma -$$

$$\begin{aligned}
& - \mathbf{w}_e^{cA^T} \left( \int_{\Omega_e^A} \mathbf{N}_p^T \phi_e^{fA^T} \tilde{\mathbf{B}}^T \mathbf{N} d\Omega \mathbf{v}_e^{fA} + \int_{\Omega_e^A} \mathbf{N}_p^T \phi_e^{fA} \mathbf{m} \mathbf{B} d\Omega \mathbf{v}_e^{fA} + \right. \\
& + \int_{\Omega_e^A} \mathbf{N}_p^T \phi_e^{sA^T} \tilde{\mathbf{B}}^T \mathbf{N} d\Omega \mathbf{v}_e^{sA} + \int_{\Omega_e^A} \mathbf{N}_p^T \phi_e^{sA} \mathbf{m} \mathbf{B} d\Omega \mathbf{v}_e^{sA} + \\
& \left. + \int_{\Omega_e^A} \mathbf{N}_p^T \frac{1}{\beta^A} \mathbf{N}_p d\Omega \mathbf{p}_e^A \right) -
\end{aligned}$$

$$\begin{aligned}
& - \mathbf{w}_e^{\text{cBT}} \left( \int_{\Omega_e^{\text{B}}} \mathbf{N}_p^{\text{T}} \phi_e^{\text{fBT}} \tilde{\mathbf{B}}^{\text{T}} \mathbf{N} \, d\Omega \, \mathbf{v}_e^{\text{fB}} + \int_{\Omega_e^{\text{B}}} \mathbf{N}_p^{\text{T}} \phi_e^{\text{fB}} \mathbf{m} \mathbf{B} \, d\Omega \, \mathbf{v}_e^{\text{fB}} + \right. \\
& + \int_{\Omega_e^{\text{B}}} \mathbf{N}_p^{\text{T}} \phi_e^{\text{sBT}} \tilde{\mathbf{B}}^{\text{T}} \mathbf{N} \, d\Omega \, \mathbf{v}_e^{\text{sB}} + \int_{\Omega_e^{\text{B}}} \mathbf{N}_p^{\text{T}} \phi_e^{\text{sB}} \mathbf{m} \mathbf{B} \, d\Omega \, \mathbf{v}_e^{\text{sB}} + \\
& \left. + \int_{\Omega_e^{\text{B}}} \mathbf{N}_p^{\text{T}} \frac{1}{\beta^{\text{B}}} \mathbf{N}_p \, d\Omega \, \mathbf{p}_e^{\text{B}} \right) \cdot \\
& - \mathbf{w}_e^{\text{sAT}} \phi_e^{\text{sA}} \int_{\Gamma_{\text{ce}}} \mathbf{N}^{\text{T}} \mathbf{n}^{\text{A}} \mathbf{M} \, d\Gamma \, \lambda_e^{\text{f}} - \mathbf{w}_e^{\text{fAT}} \phi_e^{\text{fA}} \int_{\Gamma_{\text{ce}}} \mathbf{N}^{\text{T}} \mathbf{n}^{\text{A}} \mathbf{M} \, d\Gamma \, \lambda_e^{\text{f}} - \\
& - \mathbf{w}_e^{\text{sAT}} \int_{\Gamma_{\text{ce}}} \mathbf{N}^{\text{T}} \mathbf{n}^{\text{A}} \mathbf{M} \, d\Gamma \, \lambda_e^{\text{s}} - \\
& - \mathbf{w}_e^{\text{sBT}} \phi_e^{\text{sB}} \int_{\Gamma_{\text{ce}}} \mathbf{N}^{\text{T}} \mathbf{n}^{\text{B}} \mathbf{M} \, d\Gamma \, \lambda_e^{\text{f}} - \mathbf{w}_e^{\text{fBT}} \phi_e^{\text{fB}} \int_{\Gamma_{\text{ce}}} \mathbf{N}^{\text{T}} \mathbf{n}^{\text{B}} \mathbf{M} \, d\Gamma \, \lambda_e^{\text{f}} - \\
& - \mathbf{w}_e^{\text{sBT}} \int_{\Gamma_{\text{ce}}} \mathbf{N}^{\text{T}} \mathbf{n}^{\text{B}} \mathbf{M} \, d\Gamma \, \lambda_e^{\text{s}} - \\
& - \frac{\mathbf{s}_e^{\text{sT}}}{\Delta t \, \omega} \int_{\Gamma_{\text{ce}}} \mathbf{M}^{\text{T}} \mathbf{n}^{\text{AT}} \mathbf{N} \, d\Gamma \, (\mathbf{u}_e^{\text{sA}} + \mathbf{X}_e^{\text{sA}}) + \frac{\mathbf{s}_e^{\text{sT}}}{\Delta t \, \omega} \int_{\Gamma_{\text{ce}}} \mathbf{M}^{\text{T}} \mathbf{n}^{\text{BT}} \mathbf{N} \, d\Gamma \, (\mathbf{u}_e^{\text{sB}} + \mathbf{X}_e^{\text{sB}}) - \\
& - \frac{\mathbf{s}_e^{\text{fT}}}{\Delta t \, \omega} \left( \phi_e^{\text{sA}} \int_{\Gamma_{\text{ce}}} \mathbf{M}^{\text{T}} \mathbf{n}^{\text{AT}} \mathbf{N} \, d\Gamma \, (\mathbf{u}_e^{\text{sA}} + \mathbf{X}_e^{\text{sA}}) + \phi_e^{\text{sB}} \int_{\Gamma_{\text{ce}}} \mathbf{M}^{\text{T}} \mathbf{n}^{\text{BT}} \mathbf{N} \, d\Gamma \, (\mathbf{u}_e^{\text{sB}} + \mathbf{X}_e^{\text{sB}}) + \right. \\
& \left. \phi_e^{\text{fA}} \int_{\Gamma_{\text{ce}}} \mathbf{M}^{\text{T}} \mathbf{n}^{\text{AT}} \mathbf{N} \, d\Gamma \, (\mathbf{u}_e^{\text{fA}} + \mathbf{X}_e^{\text{fA}}) + \phi_e^{\text{fB}} \int_{\Gamma_{\text{ce}}} \mathbf{M}^{\text{T}} \mathbf{n}^{\text{BT}} \mathbf{N} \, d\Gamma \, (\mathbf{u}_e^{\text{fB}} + \mathbf{X}_e^{\text{fB}}) \right) \Bigg\} = 0. \quad (4.16)
\end{aligned}$$

The notation of a summation over elements implies that an integral over an element domain  $\Omega_e^B$  would be zero when the index 'e' corresponds to an element in the domain  $\Omega^A$ . Likewise, an integral over  $\Gamma_{ce}$  would be zero when the index 'e' refers to an element that is not on the contact surface.

### Element Matrices

In Eq. (4.16), the nodal coefficients have been removed from the integrals, as they are not functions of position. Each of the remaining integrals, then, can be identified as an element level matrix, or its transpose. These matrices are

$$\mathbf{a} = \int_{\Omega_e} (\mathbf{m} \mathbf{B})^T \mathbf{N}_p d\Omega, \quad (4.17a)$$

$$\mathbf{b}^\gamma = \int_{\Omega_e} \mathbf{N}^T \tilde{\mathbf{B}} \phi_e^{s\gamma} \mathbf{N}_p d\Omega, \quad \gamma = A, B \quad (4.17b)$$

$$\mathbf{k}_e^{\alpha\gamma} = \int_{\Omega_e} \mathbf{B}^T \mathbf{D}^{\alpha\gamma} \mathbf{B} d\Omega, \quad \alpha = s, f, \quad \gamma = A, B \quad (4.17c)$$

$$\mathbf{c}_e^\gamma = \int_{\Omega_e} \mathbf{K}^\gamma \mathbf{N}^T \mathbf{N} d\Omega, \quad \gamma = A, B \quad (4.17d)$$

$$\mathbf{k}_p = \int_{\Omega_e} \mathbf{N}_p^T \mathbf{N}_p d\Omega \quad (4.17e)$$

$$\mathbf{q}_e^\gamma = - \int_{\Gamma_{ce}} \mathbf{N}^T \mathbf{n}^\gamma \mathbf{M} d\Gamma, \quad \gamma = A, B \quad (4.17f)$$

$$\mathbf{f}_e^{\alpha\gamma} = \int_{\Gamma_e^{\alpha\gamma}} \mathbf{N}^T \mathbf{t}^{\alpha\gamma} d\Gamma, \quad \alpha = s, f, \quad \gamma = A, B \quad (4.17g)$$

Recall that, because of the assumptions made during the derivation of the contact boundary conditions,  $\mathbf{k}_e^f$  is required to be zero for this element. This restricts the contact formulation to model only inviscid fluids. With these definitions, Eq. (4.16) becomes,

$$\sum_{e=1}^{n_{el}} \left\{ \begin{array}{c} w_e^{sA} \\ w_e^{fA} \\ w_e^{cA} \\ w_e^{sB} \\ w_e^{fB} \\ w_e^{cB} \\ s_e^s \\ \frac{\omega \Delta t}{s_e^f} \\ \frac{\omega \Delta t}{s_e^f} \end{array} \right\}^T \left[ \begin{array}{cccc|cccc} c_e^A & -c_e^A & 0 & 0 & 0 & 0 & 0 & 0 \\ -c_e^A & k_e^{fA} + c_e^A & 0 & 0 & 0 & 0 & 0 & 0 \\ -\phi^{sA} a^T - b^A & -\phi^{fA} a^T + b^A & 0 & 0 & 0 & 0 & 0 & 0 \\ \hline 0 & 0 & 0 & c_e^B & -c_e^B & 0 & q_e^B & \phi^{sB} q_e^B \\ 0 & 0 & 0 & -c_e^B & k_e^{fB} + c_e^B & 0 & 0 & \phi^{fB} q_e^B \\ 0 & 0 & 0 & -\phi^{sB} a^T - b^B & -\phi^{fB} a^T + b^B & 0 & 0 & 0 \\ \hline 0 & 0 & 0 & 0 & 0 & 0 & 0 & 0 \\ 0 & 0 & 0 & 0 & 0 & 0 & 0 & 0 \end{array} \right] \left\{ \begin{array}{c} v_e^{sA} \\ v_e^{fA} \\ 0 \\ \hline v_e^{sB} \\ v_e^{fB} \\ 0 \\ \hline \lambda_e^s \\ \lambda_e^f \end{array} \right\} +$$

$$+ \sum_{e=1}^{n_{el}} \left\{ \begin{array}{c} w_e^{sA} \\ w_e^{fA} \\ w_e^{cA} \\ w_e^{sB} \\ w_e^{fB} \\ w_e^{cB} \\ s_e^s \\ \frac{\omega \Delta t}{s_e^f} \\ \frac{\omega \Delta t}{s_e^f} \end{array} \right\}^T \left[ \begin{array}{cccc|cccc} k_e^{sA} & 0 & -\phi^{sA} - b^A & 0 & 0 & 0 & 0 & 0 \\ 0 & 0 & -\phi^{fA} + b^A & 0 & 0 & 0 & 0 & 0 \\ 0 & 0 & -\frac{1}{\beta} k_p & 0 & 0 & 0 & 0 & 0 \\ \hline 0 & 0 & 0 & k_e^{sB} & 0 & -\phi^{sA} - b^A & 0 & 0 \\ 0 & 0 & 0 & 0 & 0 & -\phi^{fA} + b^A & 0 & 0 \\ 0 & 0 & 0 & 0 & 0 & -\frac{1}{\beta} k_p & 0 & 0 \\ \hline q_e^{A^T} & 0 & 0 & q_e^{B^T} & 0 & 0 & 0 & 0 \\ \phi^{sA} q_e^{A^T} & \phi^{fA} q_e^{A^T} & 0 & \phi^{sB} q_e^{B^T} & \phi^{fB} q_e^{B^T} & 0 & 0 & 0 \end{array} \right] \left\{ \begin{array}{c} u_e^{sA} \\ 0 \\ p_e^A \\ \hline u_e^{sB} \\ 0 \\ p_e^B \\ \hline 0 \\ 0 \end{array} \right\} =$$

$$\begin{aligned}
& \left[ \begin{array}{c} w_e^{SA} \\ w_e^{fA} \\ w_e^{cA} \\ \vdots \\ w_e^{SB} \\ w_e^{fB} \\ w_e^{cB} \\ s_e^s \\ \frac{\omega \Delta t}{s_e^f} \\ \frac{\omega \Delta t}{s_e^f} \end{array} \right]^T = \sum_{e=1}^{n_{el}} \left\{ \begin{array}{c} f_e^{SA} \\ f_e^{fA} \\ 0 \\ \vdots \\ f_e^{SB} \\ f_e^{fB} \\ 0 \\ -\left( q^{AT} X^{SA} + q^{BT} X^{SB} \right) \\ -\left( \phi^{SA} q^{AT} X^{SA} + \phi^{fA} q^{AT} X^{fA} + \phi^{SB} q^{BT} X^{SB} + \phi^{fB} q^{BT} X^{fB} \right) \end{array} \right\} \quad (4.18)
\end{aligned}$$

The shape functions  $N_p$  are chosen according to Eq. (4.5b), and thus possess  $C^{-1}$  continuity. This allows one to solve the third and sixth equations of Eq. (4.18) for the element pressure coefficients,  $p_e^A$  and  $p_e^B$ , at the element level. This solution is

$$p_e^\gamma = \beta^\gamma(k_p)^{-1} \left( (-\phi^{s\gamma} \mathbf{a}^T - \mathbf{b} \gamma^T) \mathbf{v}^{s\gamma} + (-\phi^{f\gamma} \mathbf{a}^T + \mathbf{b} \gamma^T) \mathbf{v}^{f\gamma} \right), \quad \gamma = A, B, \quad (4.19)$$

which can now be substituted back into Eq. (4.18), yielding

$$\begin{aligned}
& \sum_{e=1}^{n_{el}} \left\{ \begin{matrix} w_e^A \\ w_e^B \\ \frac{s_e}{\omega \Delta t} \end{matrix} \right\}^T \left[ \begin{matrix} C_e^A + \mathcal{B}_e^A & 0 & Q_e^A \\ 0 & C_e^B + \mathcal{B}_e^B & Q_e^B \\ 0 & 0 & 0 \end{matrix} \right] \left\{ \begin{matrix} v_e^A \\ v_e^B \\ \lambda_e \end{matrix} \right\} + \\
& + \sum_{e=1}^{n_{el}} \left\{ \begin{matrix} w_e^A \\ w_e^B \\ \frac{s_e}{\omega \Delta t} \end{matrix} \right\}^T \left[ \begin{matrix} K_e^A & 0 & 0 \\ 0 & K_e^B & 0 \\ Q_e^{AT} & Q_e^{BT} & 0 \end{matrix} \right] \left\{ \begin{matrix} u_e^A \\ u_e^B \\ 0 \end{matrix} \right\} = \\
& = \sum_{e=1}^{n_{el}} \left\{ \begin{matrix} w_e^A \\ w_e^B \\ \frac{s_e}{\omega \Delta t} \end{matrix} \right\}^T \left\{ \begin{matrix} f_e^A \\ f_e^B \\ g_e \end{matrix} \right\} \quad (4.20)
\end{aligned}$$

The element matrix  $\mathcal{B}_e^\gamma$  comes from the penalty terms and gradient of volume fraction, and is given by

$$\mathcal{B}_e^\gamma = \beta^\gamma \begin{bmatrix} (\phi^{s\gamma} \mathbf{a} + \mathbf{b}) \mathbf{k}_p^{-1} (\phi^{s\gamma} \mathbf{a} + \mathbf{b})^T & -(\phi^{s\gamma} \mathbf{a} + \mathbf{b}) \mathbf{k}_p^{-1} (-\phi^{f\gamma} \mathbf{a} + \mathbf{b})^T \\ -(-\phi^{f\gamma} \mathbf{a} + \mathbf{b}) \mathbf{k}_p^{-1} (\phi^{s\gamma} \mathbf{a} + \mathbf{b})^T & (-\phi^{f\gamma} \mathbf{a} + \mathbf{b}) \mathbf{k}_p^{-1} (-\phi^{f\gamma} \mathbf{a} + \mathbf{b})^T \end{bmatrix}, \quad \gamma = A, B \quad (4.21a)$$

and,

$$\mathbf{C}_e^\gamma = \begin{bmatrix} \mathbf{c}_e^\gamma & -\mathbf{c}_e^\gamma \\ -\mathbf{c}_e^\gamma (\mathbf{k}_e^{f\gamma} + \mathbf{c}_e^\gamma) & \end{bmatrix}, \quad \gamma = A, B, \quad (4.21b)$$

$$\mathbf{K}_e^\gamma = \begin{bmatrix} \mathbf{k}_e^{s\gamma} & \mathbf{0} \\ \mathbf{0} & \mathbf{0} \end{bmatrix}, \quad \gamma = A, B, \quad (4.21c)$$

$$\mathbf{Q}_e^\gamma = \begin{bmatrix} \mathbf{q}_e^\gamma & \phi^{s\gamma} \mathbf{q}_e^\gamma \\ \mathbf{0} & \phi^{f\gamma} \mathbf{q}_e^\gamma \end{bmatrix}, \quad \gamma = A, B, \quad (4.21d)$$



$$\mathbf{v}_e^\gamma = \begin{Bmatrix} \mathbf{v}_e^{s\gamma} \\ \mathbf{f}_e^\gamma \\ \mathbf{v}_e \end{Bmatrix}, \quad \mathbf{u}_e^\gamma = \begin{Bmatrix} \mathbf{u}_e^{s\gamma} \\ \mathbf{f}_e^\gamma \\ \mathbf{u}_e \end{Bmatrix}, \quad \mathbf{w}_e^\gamma = \begin{Bmatrix} \mathbf{w}_e^{s\gamma} \\ \mathbf{f}_e^\gamma \\ \mathbf{w}_e \end{Bmatrix}, \quad \gamma = A, B, \quad (4.21e)$$

$$\lambda_e = \begin{Bmatrix} \lambda_e^s \\ \lambda_e^f \\ \lambda_e \end{Bmatrix}, \quad \mathbf{s}_e = \begin{Bmatrix} \mathbf{s}_e^s \\ \mathbf{s}_e^f \\ \mathbf{s}_e \end{Bmatrix}, \quad (4.21f)$$

$$\mathbf{f}_e^\gamma = \begin{Bmatrix} \mathbf{f}_e^{s\gamma} \\ \mathbf{f}_e^\gamma \\ \mathbf{f}_e \end{Bmatrix}, \quad \gamma = A, B, \quad (4.21g)$$

$$\mathbf{g}_e = \begin{Bmatrix} -(\mathbf{q}^A \mathbf{A}^T \mathbf{X}^s \mathbf{A} + \mathbf{q}^B \mathbf{B}^T \mathbf{X}^s \mathbf{B}) \\ -(\phi^s \mathbf{A} \mathbf{q}^A \mathbf{A}^T \mathbf{X}^s \mathbf{A} + \phi^f \mathbf{A} \mathbf{q}^A \mathbf{A}^T \mathbf{X}^f \mathbf{A} + \phi^s \mathbf{B} \mathbf{q}^B \mathbf{B}^T \mathbf{X}^s \mathbf{B} + \phi^f \mathbf{B} \mathbf{q}^B \mathbf{B}^T \mathbf{X}^f \mathbf{B}) \end{Bmatrix}. \quad (4.21h)$$

It is interesting to note that the matrix  $\mathbf{q}_e^\gamma$  is precisely that which arises in a Lagrange multiplier formulation for single phase elasticity. This matrix couples the multipliers to degrees of freedom on both sides 'A' and 'B' of the interface. In the biphasic case, the matrix  $\mathbf{Q}_e^\gamma$  performs this coupling, including the cross coupling between solid and fluid degrees of freedom on opposite sides of the contact surface.

Before assembling the global counterpart of Eq. (4.20), the family of generalized trapezoidal finite difference rules is applied in time [66]. For the present implementation, the time scale of the problem is divided into uniform increments of length  $\Delta t$ , and the displacement at the current time step is written in terms of the current velocity and the displacements and velocities at the previous time step,

$$\mathbf{u} = \hat{\mathbf{u}} + \Delta t (1-\omega) \hat{\mathbf{v}} + \Delta t \omega \mathbf{v}. \quad (4.22)$$

The superposed (^) indicates the known value at the previous time step and  $\omega$  is an user-defined parameter chosen between 0 and 1 that controls the order of accuracy of the time integration, numerical damping, *etc.* When  $\omega \geq 0.5$  the integration corresponds to an

implicit method which is stable for any size time step. Comments on the choice of this parameter for the biphasic contact finite element are given in Appendix A. Equation (4.22) is substituted into Eq. (4.20) and the known values are transferred to the right hand side.

$$\begin{aligned}
 \sum_{e=1}^{n_{el}} \begin{Bmatrix} w_e^A \\ w_e^B \\ s_e \end{Bmatrix}^T \left[ \begin{bmatrix} C_e^A + \mathcal{B}_e^A & 0 & Q_e^A \\ 0 & C_e^B + \mathcal{B}_e^B & Q_e^B \\ Q_e^{AT} & Q_e^{BT} & 0 \end{bmatrix} + \omega \Delta t \begin{bmatrix} K_e^A & 0 & 0 \\ 0 & K_e^B & 0 \\ 0 & 0 & 0 \end{bmatrix} \right] \begin{Bmatrix} v_e^A \\ v_e^B \\ \lambda_e \end{Bmatrix} = \\
 = \sum_{e=1}^{n_{el}} \begin{Bmatrix} w_e^A \\ w_e^B \\ s_e \end{Bmatrix}^T \begin{Bmatrix} f_e^A \\ f_e^B \\ \frac{g_e}{\omega \Delta t} \end{Bmatrix} - \\
 - \sum_{e=1}^{n_{el}} \begin{Bmatrix} w_e^A \\ w_e^B \\ s_e \end{Bmatrix}^T \begin{bmatrix} K_e^A & 0 & 0 \\ 0 & K_e^B & 0 \\ \frac{Q_e^{AT}}{\omega \Delta t} & \frac{Q_e^{BT}}{\omega \Delta t} & 0 \end{bmatrix} \begin{Bmatrix} \hat{u}_e^A + \Delta t(1-\omega)\hat{v}_e^A \\ \hat{u}_e^B + \Delta t(1-\omega)\hat{v}_e^B \\ 0 \end{Bmatrix} \quad (4.23)
 \end{aligned}$$

Note that the contributions from the contact elements are symmetric because of the choice of the algebraic scale factor introduced in Eq. (4.11). Standard finite element assembly procedures are now applied to this system, and the assembled weight functions are recognized as arbitrary, which leads to a global system of differential equations in time,

$$\begin{aligned}
 \left[ \begin{bmatrix} C^A + \mathcal{B}^A & 0 & Q^A \\ 0 & C^B + \mathcal{B}^B & Q^B \\ Q^{AT} & Q^{BT} & 0 \end{bmatrix} + \omega \Delta t \begin{bmatrix} K^A & 0 & 0 \\ 0 & K^B & 0 \\ 0 & 0 & 0 \end{bmatrix} \right] \begin{Bmatrix} v^A \\ v^B \\ \lambda \end{Bmatrix} = \\
 = \begin{Bmatrix} f^A \\ f^B \\ \frac{g}{\omega \Delta t} \end{Bmatrix} - \begin{bmatrix} K^A & 0 & 0 \\ 0 & K^B & 0 \\ \frac{Q^{AT}}{\omega \Delta t} & \frac{Q^{BT}}{\omega \Delta t} & 0 \end{bmatrix} \begin{Bmatrix} \hat{u}^A + \Delta t(1-\omega)\hat{v}^A \\ \hat{u}^B + \Delta t(1-\omega)\hat{v}^B \\ 0 \end{Bmatrix} \quad (4.24)
 \end{aligned}$$

where the matrices without the subscript 'e' are the assembled counterparts of those with the 'e'. This is a semi-definite system as is typical of Lagrange multiplier methods. Note that as the contact surface evolves in this linear problem, only the matrices  $\mathbf{Q}^A$  and  $\mathbf{Q}^B$  will change, so for a direct solution strategy the upper 2x2 block of Eq. (4.24) need be factored only once.

### Quadratic Velocity Triangle

For the first biphasic contact finite element, the computer implementation is restricted to the six-node, quadratic-velocity triangle. Details of the interpolation, integration order and post processing are given by Maxian [91]. This section will be primarily concerned with the additional requirements of the contact matrices.

Interpolations for displacement and velocity are quadratic, and use the familiar Lagrangian shape functions for the triangle [66]. Both a plane strain and an axisymmetric version of the element have been implemented. The element is isoparametric, and has nodes at the vertices and mid-edges. All calculations are performed in the element parent coordinates system, which is based on triangular area coordinates. Gaussian quadrature of sufficient order to exactly integrate straight-sided elements is performed for all element matrices.

The pressure interpolation is linear within an element, and independent from element to element, as would be expected for this constrained media problem. Maxian found that a three-parameter interpolation written directly in terms of the triangular coordinates produced a matrix  $\mathbf{k}_p$  that was insensitive to numerical instability during inversion [91]. It should be recognized that the combination of quadratic velocity and linear, discontinuous pressure produces an element which violates the Babuska-Brezzi

condition [66] for linear elasticity. In practice, the triangular biphasic element performs well, and shows no signs of locking or constraint violation for reasonable meshes. Alternatively, the quadratic-velocity, constant-pressure element does satisfy the Babuska-Brezzi condition. Experiments performed with the one-parameter pressure interpolation in the contact formulation showed no improvement in the behaviour of the solutions. The discussion may not be directly extensible to three dimensions, however. Recent convergence studies by Almeida with simplex and hexahedral elements in three dimensions show that the tetrahedron can be sensitive to mesh gradation and orientation when using the linear pressure interpolation [6].

If the finite element matrices are to be symmetric, which is a highly desirable characteristic, the multipliers and contact weight functions must be interpolated with the same functions. There are two possibilities, then, when choosing the order of interpolation for these variables. Examining the weak form of the weighted residual statement, Eq. (4.12), one sees terms that are products of the multiplier with the velocity weight functions, and others that are products of the contact weight function with velocity. In addition, recall Eqns. (4.2-3) which define the multipliers as tractions.

The first possible interpolation is to choose the multipliers to be of the same order as traction, *e.g.*, the gradient of displacement. For this element, that is a linear interpolation. In the case of node-to-node contact, traction evaluated in elements on either side of the interface is equal pointwise, and equal to the multiplier. The kinematic contact constraints are only enforced pointwise, however. The second theory is to choose the interpolant such that there are as many independent coefficients in the contact weight function as there are in the velocity. This is a quadratic interpolation and would produce solutions where the weighted integral form of the kinematic contact continuity relations

are exactly enforced. This element uses the second philosophy, which favors a more rigorous enforcement of the kinematic conditions, but does not allow one to equate the element traction with the multipliers at a particular location within the element. Numerical experiments with elastic contact elements in the symbolic algebra package MAPLE [31] support these conclusions, and are presented in Appendix B.

The choice of function spaces does not require the interpolation for the multipliers to be continuous between elements. With a Lagrange multiplier method, though, the final matrix equations are semi-definite, and do not allow the multipliers to be eliminated at the element level. Thus, there is no computational advantage in choosing a discontinuous interpolation.

For the triangular element, the contact surface will be a curve in space. This implies that the contact interpolations will be the familiar Lagrange polynomials of order two defined on the canonical range  $(-1,1)$ . Here too, Gaussian quadrature of sufficient order to exactly integrate straight-sided elements will be used to compute integrals of the matrices  $\mathbf{q}$ . The following chapter will detail the procedures for assembling these matrices for the discrete representation of the contact surface.



# Chapter V: Contact Surface Calculations

## Introduction

As described earlier, the contact surface is unknown in advance, and iterations must be performed to find that surface which is consistent with the Kuhn-Tucker relations, Eqns. (2.43). In addition, a discretization of the contact surface is required so that the contact matrices can be evaluated. It is important that the discretization algorithm be robust, computationally efficient and insensitive to mesh gradation. While the proposed method of discretizing the contact surface has been implemented only in two dimensions, it is readily extensible to three dimensions, and would suffer only from the naturally higher cost of three-dimensional geometric calculations.

Contact surface calculations can become a significant part of the computational effort during finite element analysis [24]. It is essential that efficient means of contact detection be developed, and that these be optimized for either scalar, vector or parallel hardware. Several algorithms have been presented in the literature, including the pinball algorithm of Belytschko and Neal [24] and the contact segment treatment of Simo, Wriggers and Taylor [126]. Others have included the contact surface kinematics directly into a finite element formulation [58]. Laursen and co-workers have recently proposed a method which localizes all calculations to numerical quadrature points within finite elements on the contact surface [82,83]. This same algorithm was independently developed in the course of the present research.

Within an iterative cycle, three main tasks must be performed. First, given a point on one side of the contact surface, the closest point projection to the opposing surface is

computed, and the finite element containing this projection is found. Second, utilizing the projection results, a discretized form of the contact surface is developed, which will be used in forming the contact matrices. Last, there is an assessment of changes to the surface, including points that come into or are released from contact. Each of these topics is covered in detail in the subsequent sections. The chapter concludes with a description of the iteration algorithm itself.

### Closest Point Projection

In evaluating the Kuhn-Tucker relations, Eqns. (2.43), the vector from a point on one surface directed normal to the opposing surface is required. This vector is referred to as the *gap function*, and, by construction, represents the minimum distance to the opposing surface. It has its origin at a *contactor point*,  $\mathbf{x}_c$ , located on a *contactor surface*, and terminates at the nearest point,  $\mathbf{x}^*$ , on a *target surface*. In the finite element context, this function will be evaluated with respect to the isoparametric coordinate interpolation. Although this formulation has been developed within the limits of infinitesimal deformation theory, a distinction must be made at this point between reference and current coordinates. All calculations and solution quantities are referred to the reference configuration; however, for the purpose of identifying evolving contact, a current coordinate system must be used. Thus, the gap function is defined with respect to the current configuration of the contactor and target surfaces, represented by the deformed coordinates of finite element nodes on these surfaces.

Three pieces of data result from this calculation: the finite element which contains the closest point projection, the local coordinate of the projection within that element and the magnitude of the gap function. An algebraic sign is associated with the magnitude to



indicate whether the contact point has penetrated the target surface. A positive magnitude represents surfaces which are not in contact. The sign is computed by comparing the direction of the gap function with that of the external normal to the contactor surface. The sign of the inner product of the normal vector with the gap function is taken as the sign of the magnitude, as illustrated in Fig. 5.1

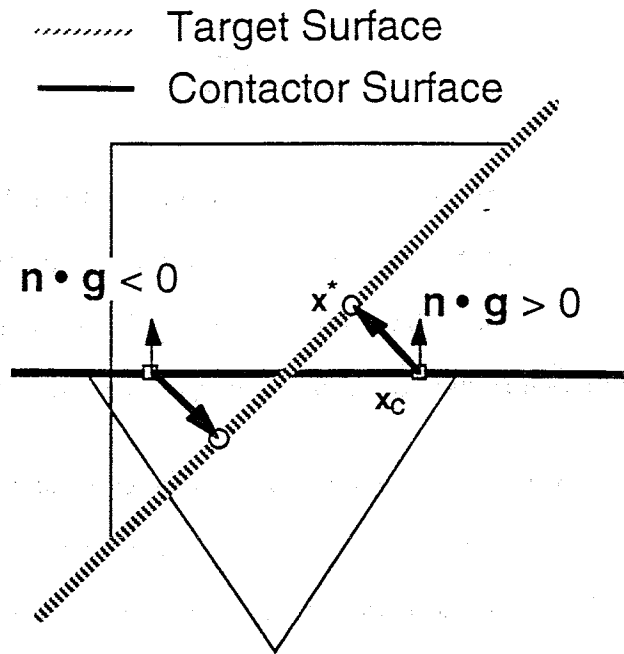


Fig. 5.1. Definition of the gap function and its sign on a contactor surface.

Mathematically, the closest point projection is stated as a minimization problem. Given a spatial point,  $\mathbf{x}_c$ , on the contactor surface find the spatial point,  $\mathbf{x}^*$ , on the target surface that minimizes the distance from  $\mathbf{x}_c$  to the target. Symbolically this is represented by the equations

$$\mathbf{g} = \mathbf{x} - \mathbf{x}_c \quad \mathbf{x} \in \{ \mathbf{x}_t \}, \quad (5.1a)$$

$$\frac{d \|\mathbf{g}(\mathbf{x}^*)\|}{d\mathbf{x}} = 0, \quad (5.1b)$$

where the set  $\{\mathbf{x}_t\}$  is the target surface. When the target surface is discretized by isoparametric finite elements, these calculations can be performed for each element that lies on the surface, and one can take advantage of a local coordinate system,  $\xi$ , within these elements to reduce the dimensionality of the problem. This is expressed as

$$\mathbf{g}^e(\xi) = \mathbf{x}(\xi) - \mathbf{x}_c, \quad \mathbf{x} \in \{\mathbf{x}_t\}, \quad (5.2a)$$

$$\min_e \left( \frac{d \|\mathbf{g}^e(\xi^*)\|}{d\xi} = 0 \right). \quad (5.2b)$$

In performing the minimization over elements, solutions  $\xi^*$  outside the valid range of local coordinates must be discarded. The discrete equations have the advantage of returning the required finite element and local coordinate as their solution. This information can then be used to calculate the gap function and its sign.

For the six-node triangle, Eq. (5.2b) is a cubic equation in one variable, which has a closed-form solution [136]. In three dimensions, the problem rapidly becomes more difficult to solve. For example, for straight-sided tetrahedra, there are two linear equations in two variables. When the elements have curved sides, there are two nonlinear equations in two variables. Despite the difficulty, one can still obtain a solution. This algorithm can be made much more efficient by reducing the number of elements that are tested for the minimum. One such methodology is the pinball algorithm of Belytschko and Neal [24], where finite elements are replaced by spheres of equal volume. It is relatively inexpensive, then, to compare the distance between the centers of two spheres with their radii. Only those elements whose spheres overlap need be checked in Eq. (5.2b).

The present finite element is built upon a topological data structure for both the finite element mesh and the geometric model, referred to as a radial edge representation

[160]. In this structure the topology of a finite element is composed of four hierarchical entities: vertices, edges, faces and regions, ranked zero through three, respectively. Two vertices bound an edge, edges in turn bound faces, and faces bound regions. Any entity within the mesh contains pointers to the higher order entities that use it, and to the lower order entities it uses. The data structure is depicted graphically for a simple mesh in Fig. 5.2. Similarly, a topological representation of the physical geometry is maintained by a geometric modeling program. During the course of generating the finite element mesh [120], each mesh entity is classified on a topological entity of the geometric model. The classification always refers to the lowest order geometric entity that contains the mesh entity. For example, finite element vertex '4' in Fig. 5.2 would be classified on the underlying model vertex, not on the model edge or model face. This proves an highly efficient means by which to program a finite element with regard to attribute specification [121] and other issues, and this topological data is also advantageous when treating contact.

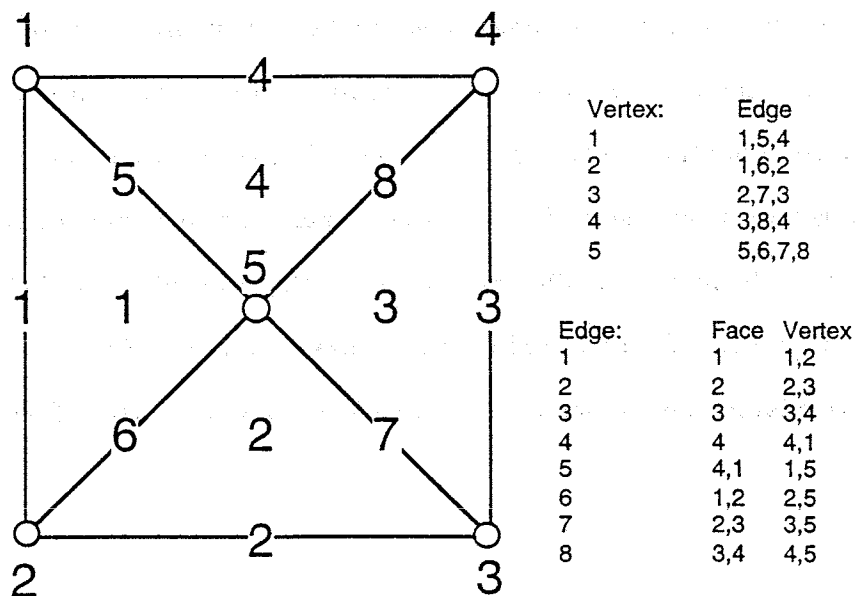


Fig 5.2. Finite element mesh of four triangles with the topological entities identified. A sample of the upward and downward pointers for edges and vertices is given at right.

As a consequence of the classification property in the radial edge data structure, it is a trivial matter to compute those finite elements whose mesh entities are on the model boundary. This avoids costly procedures to determine which elements lie on the boundary [23], or the need to store this information and search through it. Once the finite element containing the projection has been found, subsequent searches during the evolving contact problem can utilize topological adjacencies to limit the number of elements that are evaluated. Strategies based on the mesh topology are used in the current two-dimensional implementation and prove quite efficient.

## Surface Discretization

To initialize contact a user denotes model edges, in two dimensions, or model faces, in three dimensions, as *contactors* or *targets*. The finite element edges or faces that lie on those model entities then become contactor or target *segments*. A contactor segment may come in contact with a target, or several targets, in any part of the model, except those within the same model region as the contactor (note that one physical body may be composed of multiple model regions, though). The code does not allow contactor segments to contact other contactors. In the case of an internal model edge or face shared by multiple regions, it should be identified as a contactor; the code will define both the contactor and target segments. A sample finite element mesh is given in Fig. 5.3, which shows how the contactor-target designation would be able to identify three pairs of contacting surfaces.

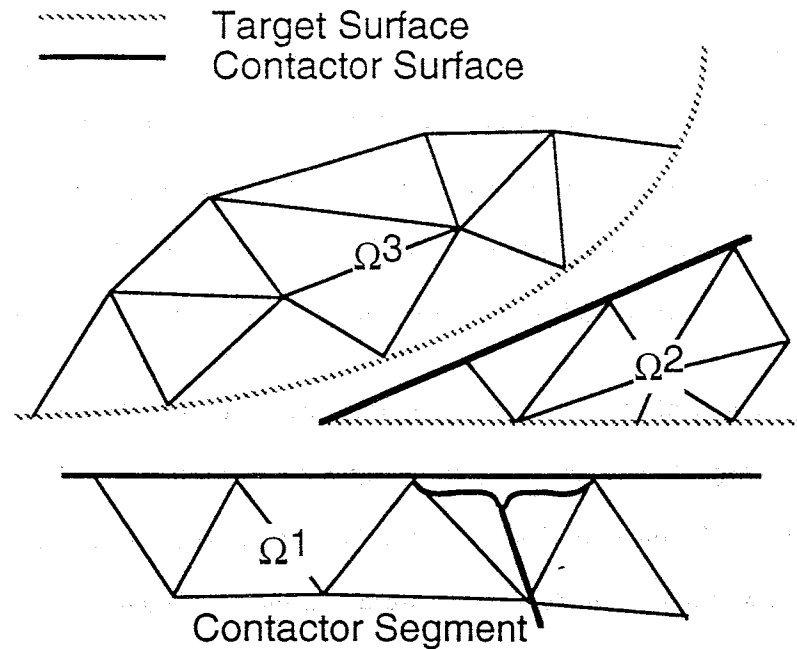


Fig. 5.3. Section of a finite element mesh composed of three model regions. An appropriate selection of the contactor and target surfaces is indicated.

When complex mechanical systems are subjected to loading, one often does not know where the contact areas will be. Thus, the present assumptions on contactor-target pairs may seem overly restrictive. For biological systems, however, there is a growing body of data to indicate where the prospective contact areas are (for example, [68,134,135]). With this knowledge of the contactor-target pairs, it is straightforward to generate a model and annotate it with this information. The contactor-target methodology is merely a convenience to reduce the number of surface elements that must be searched for a closest point projection. In the future, if more complex contact geometries arise, one can abandon this treatment in favor of a more general searching algorithm, at the expense of higher computational cost.

Examples presented in the following chapter show that the solution is not biased by the choice of contactors or targets with regard to mesh refinement, material properties or expected deformation. One exception may be the case where the level of mesh refinement

on a contactor is significantly less than that on a target. While the algorithm would function, there is the possibility that evolving contact could not be resolved properly, or that the contact continuity conditions would not be adequately enforced. Arbitrarily, then, the contactor surface is associated with domain 'A' referred to in the problem definition set forth in Chapter II, and the target surface is identified with domain 'B'.

The contact algorithm requires integrals to be performed along the contact surface. These integrals involve terms uniquely defined on the interface, and alternately, terms defined in the domain elements on either side of the contact surface. The discretization algorithm must provide a coordinate system in which to perform the integrals and information about the domain elements on either side. The most easily identified coordinate system is that which is already defined within the contactor segments. The nodes of the contact elements will therefore be chosen to coincide with those of the finite elements along the contactor surface. Interpolations of quantities associated with side 'A' of the contact surface are readily available, since the contact elements are aligned with the finite elements on the model boundary. Quantities associated with side 'B' can be computed in the finite element containing the closest point projection. More information concerning the contact elements and degree of freedom numbering is given below in the section on element matrix calculations.

## **Detecting Contact or Release**

For each candidate contactor segment, an assessment must be made as to whether this segment should be included in the contact surface. Since the contact matrices will be integrated with numerical quadrature, this assessment is made for each quadrature point within the segment. Thus, the quadrature points also become the contactor points,  $\mathbf{x}_c$ , used

to define the gap function. For each quadrature point two pieces of data are stored: the finite element into which it is projected and the local coordinate of the projected point. This data is the minimum required to perform the contact integrals and to define the degree of freedom connectivity for assembling the contact matrices.

Two other pieces of data are used to determine if this quadrature point should be considered active or not active for the contact integrals. These are the gap function and the normal component of total traction, calculated in the reference coordinates of the contactor segment. For quadrature points that were not previously active, they will be active in this iteration only if the gap is less than some positive tolerance. For quadrature points that were previously active, they will remain so if the normal component of total traction is negative and will be released if the traction is tensile. Note that, with a Lagrange multiplier method, the gap function at active quadrature points will be zero, within numerical precision. This would not necessarily be true with a penalty method, or an augmented Lagrangian, where the constraint is approximated. These conditions are derived from the Kuhn-Tucker relations, Eqns. (2.43), and will form the basis of the iterative process in the final section of this chapter.

A tolerance parameter is required to define proximity for the contact calculations. To avoid user-specified values, the tolerance is chosen as a fraction of the minimum contactor segment length,

$$\text{TOL} = \alpha_c h_{\min}. \quad (5.3)$$

Selecting the fraction  $\alpha_c$  requires some special considerations. It is possible (in fact, it is often the case) that a contact geometry will have only point contact at the initial time. If the tolerance were zero, this would produce a contact surface of zero length, and effectively

uncouple the two domains. Having ignored the inertia terms in the governing equations, this situation will result in an ill-posed problem when forces are applied. To circumvent this difficulty, the fraction  $\alpha_c$  has different values at  $t = 0$  and at  $t > 0$ . The program chooses default values of 0.1 and 0.0001, respectively, for  $\alpha_c$  at these times, although the user may override these choices. This has the effect of making the initial surface large, and allowing the contact-release algorithm to remove segments as needed in the early iterations. At later times, the domains must nearly penetrate before contact is extended. In general the solution is relatively insensitive to this parameter, however, a poor choice will result in more contact iterations to converge at a given time step. Effects of varying the parameter are given in the examples.

## Element Matrix Calculations

Degrees of freedom for the multipliers will be associated with the finite element nodes of the contactor segments. If at least one of the quadrature points within a contactor segment is classified as active, then the degrees of freedom are created for its nodes and are assigned unique numbers. To illustrate this refer to Eq. (4.17f), repeated here as Eq. (5.4), defining the element level contact submatrix,

$$\mathbf{q}_e^\gamma = - \int_{\Gamma_{ce}} \mathbf{N}^T \mathbf{n} \gamma \mathbf{M} \, d\Gamma, \quad \gamma = A, B. \quad (5.4)$$

When the index  $\gamma$  is taken to be 'A', the domain of the integral,  $\Gamma_{ce}$ , will be an entire contactor segment. Interpolations for the multipliers,  $\mathbf{M}$ , are defined in the local coordinates of this contactor segment. Likewise, the surface normal,  $\mathbf{n}$ , and velocity interpolations,  $\mathbf{N}$ , can be computed by looking to the finite element associated with this contactor segment. In practice, each of these terms will be evaluated at some number of



quadrature points along the contactor segment. In general, there is no direct correspondence between the local coordinates within a contactor segment and those within a *single* target segment, as illustrated by Fig. 5.4. For this reason, contributions to both  $\mathbf{q}^A$  and  $\mathbf{q}^B$  are assembled on a per-quadrature-point basis. Thus, the contribution to  $\mathbf{q}^A$  from the first active quadrature point in the contactor segment is computed and assembled into the global matrix. Then the contribution to  $\mathbf{q}^B$  is calculated with respect to the finite element associated with the target segment containing the projection. Recall from the previous discussion that this closest point projection information has been stored for each quadrature point. This methodology allows for several interesting features including node-to-edge contact, partial contact within a contactor segment and multiple regions contacting at one point.

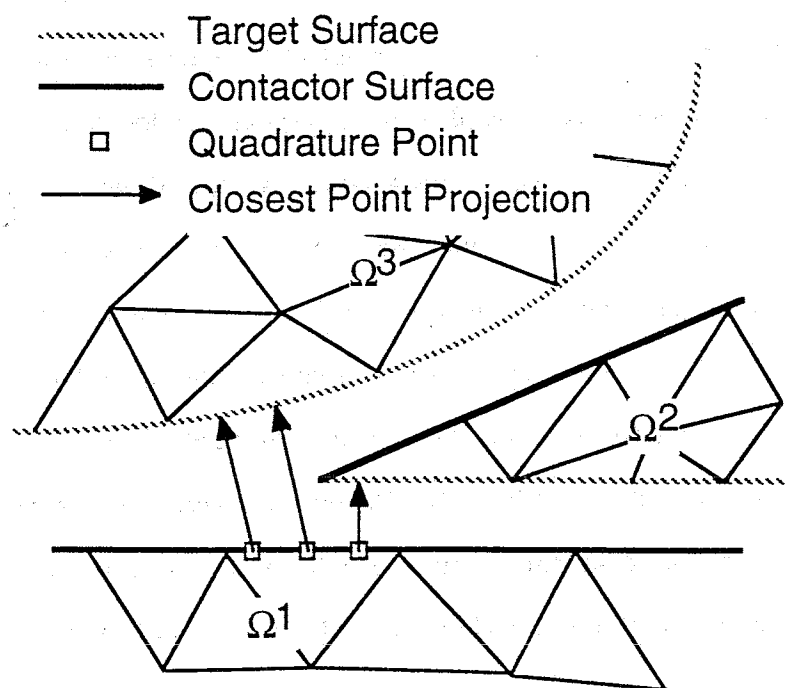


Fig. 5.4. Section of a finite element mesh indicating the projection of quadrature points to the target surface. A contactor segment in  $\Omega^1$  is coupled to multiple target segments in different regions.

In the context of a direct equation solver, the form of the finite element matrix equations for contact can be quite undesirable. There is a block of zeros on the diagonal, and there are columns corresponding to the contact matrices that have a large bandwidth (see Eq. (4.24)). Since the location of the zero diagonals can be anticipated, Crout elimination can be used and there is no restriction placed on the solver. An intelligent node numbering scheme can be effective in reducing the amount of computational effort required to factor or solve the matrix equations. A reverse Cuthill-McKee [37] algorithm is used, and its present implementation is based on the radial edge representation of the finite element mesh.

To begin, a finite element vertex, or group of vertices, is chosen as the starting point, or *seed*, of a queue. The queue is set up as a first-in-first-out data structure. The algorithm proceeds by taking a vertex out of the queue and assigning it a node number. Then, respectively, unnumbered nodes in regions, on faces or on edges surrounding the vertex are numbered. Last, vertices with unnumbered nodes on edges connected to this vertex are added to the queue and the process is repeated until the queue is empty. Once the numbering is complete, it is fully reversed. An effective means to implement this in the contact code is to seed the queue with the contactor and target finite element vertices. In the first pass, these will be given the lowest node (and hence degree of freedom) numbers. When reversed, they will have the highest numbers. As the active contact degrees of freedom are assigned, their numbers will be closest to the degrees of freedom of the contactor and target finite elements, minimizing the column heights of the coupling matrices.

## Contact Iterations

While the Lagrange multiplier treatment of the contact boundary conditions guarantees that these conditions will be satisfied on the contact surface, it does not ensure that this is the correct surface. An independent test is required to make this assessment, and an iterative algorithm is implemented to find the proper contact surface. The choice of active or inactive contact segments is modified by recognizing two forms of non-physical behaviour: material overlap or tensile contact traction. Both of these conditions are precluded by the Kuhn-Tucker relations, Eqns. (2.43).

If a contact surface is selected which is smaller than the true surface, the material will appear to be more compliant and will experience a deformation greater than the true solution. Since there is no boundary condition outside the active contact segments, boundaries from either domain may deform past each other. This will be identified by a negative gap function during the subsequent validity check. On the other hand, if the contact surface is chosen larger than the true surface, the material response will be excessively stiff. The kinematic contact boundary conditions dictate that points on  $\Gamma_c$  will have the same current position. The multipliers function to apply a force which produces exactly this deformation, even if the result is a tensile contact force. If the multiplier, or more precisely the normal component of total traction, is positive this indicates that this point should be released from contact.

Iterations, then, will be performed until the Kuhn-Tucker relations are satisfied. In the finite element implementation each quadrature point on the contactor surface is assessed as active or inactive according to Fig. 5.5 below, and contact contributions are assembled from the active points.

```

CONVERGE:=true
for each quadrature point {
  compute  $\mathbf{g}$  and  $\mathbf{n} \cdot \mathbf{t}^T$ 
  if (inactive &&  $\|\mathbf{g}\| < \text{TOL}$ ) {
    make active
    CONVERGE:=false}
  else if (active &&  $\mathbf{n} \cdot \mathbf{t}^T > 0$ ) {
    make inactive
    CONVERGE:=false}
}
if (CONVERGE)
  goto next time step
else
  solve with updated surface

```

Fig. 5.5. Algorithm for contact surface iterations.

A solution to the matrix equations is generated, and each quadrature point is reassessed. If no point changes its state, then convergence has been achieved; otherwise, the solution is recomputed with the updated status of the quadrature points. Once convergence is achieved, the solution is advanced to the next time step with the current state of the quadrature points retained. In practice a limit is placed on the number of iterations within a time step. An example showing the progress of the iterations is presented as one of the validation problems in the next chapter.

# Chapter VI: Two Dimensional Examples

## Introduction

The contact code must perform two functions. First, given the contact surface it must enforce the required continuity of kinematic and kinetic variables across that interface. Second, when the contact surface evolves in time, there must be logic to adjust the definition of the surface for advancing or retreating contact. In validating the proposed formulation, each of these requirements will be addressed with separate examples.

With the element and algorithms verified, the program may be used to model problems of clinical significance. In the present implementation, only plane strain or axisymmetric geometries may be analyzed for deformations within the linear regime. This precludes cases where there is large-displacement, sliding contact, effectively eliminating some of the more interesting clinical applications. Axial compression of the gleno-humeral joint of the shoulder does provide an axially symmetric geometry that can be analyzed with the current formulation. Contact between the femur, meniscus and tibia is another that awaits a solution. While the knee joint is not axially symmetric, two different axisymmetric geometric approximations are analyzed to investigate the dependence of the solution on geometry. This problem also demonstrates that the discretization algorithm functions properly for multi-body contact where there are three pairs of contacting surfaces.

## Validation Examples

Three examples are chosen to validate the biphasic contact finite element. The first checks that the kinematic and kinetic contact continuity relations are enforced across the

contact surface in a mesh where there is node-to-node contact. Two cases are run: one where the solid content is continuous and one where it experiences a jump across  $\Gamma_c$ . A second problem assesses the performance of the contact discretization and iteration algorithms. The elastic Hertz problem is used, since there is a closed form solution. Last, comparisons are made to an analytic solution of a spherical biphasic indentation test. This verifies both the continuity enforcement and contact iterations for a problem with two-phase materials.

### Unconfined Compression

One of the most fundamental tissue tests performed experimentally is the unconfined compression test. The solution to this problem is well known, and it provides an excellent means to test the contact algorithms. One quadrant of a plane strain unconfined compression geometry is analyzed. This quadrant is divided into two material regions at the quarter-height of the sample. The primary goal with this problem is to demonstrate that the required continuity on a contact interface is enforced. One expects that with either a lubricated or adhesive platen, in stress relaxation or creep, there will be no shear at the contact interface, and thus the contact surface geometry will not change in time. The finite element mesh provides node-to-node contact, and it is trivial to validate that the discretization algorithm is performing correctly.

Geometry and boundary conditions are given in Fig. 6.1, while the finite element mesh for this example is in Fig. 6.2. Material properties for each material region are chosen to simulate articular cartilage:  $\lambda = 0.1\text{MPa}$ ,  $\mu = 0.3\text{MPa}$ ,  $\phi^s = 0.17$ ,  $\kappa = 7.6 \times 10^{-15} \text{ m}^4/\text{Ns}$  and  $\beta = 1.0 \times 10^{14}$ , where  $\lambda$  and  $\mu$  are the Lamé parameters for the isotropic solid matrix. There should be no confusion between the Lamé parameter  $\lambda$  and the Lagrange multipliers  $\lambda^{s,f}$ . The sample has  $h = 1.78\text{mm}$  and  $w = 6.35\text{mm}$ . An uniform

displacement whose value increases linearly from  $u = 0$  at  $t = 0$  to  $u_0 = 0.05h/2 = 0.045\text{mm}$  at  $t = t_0 = 500\text{s}$  is applied to the upper, frictionless platen. These material and physical parameters follow values reported by Mow *et al.* [96].

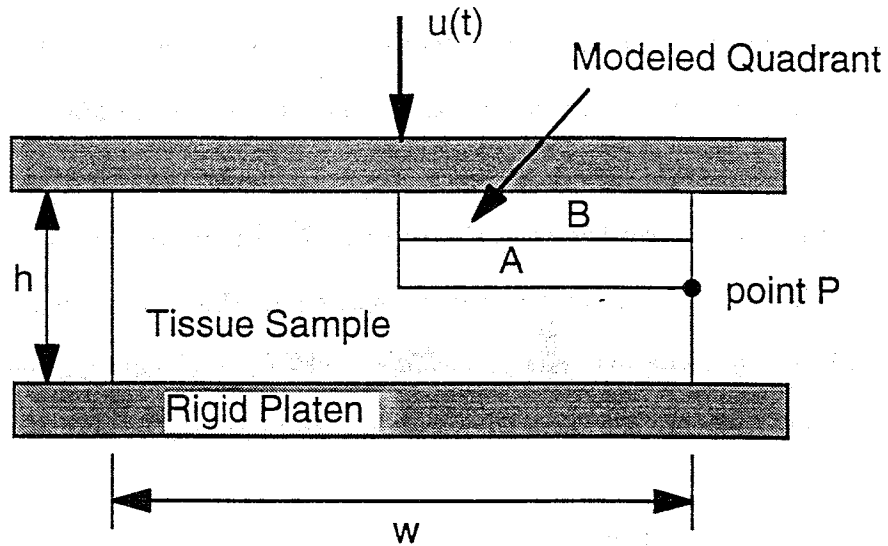


Fig. 6.1. Geometry and boundary conditions for the frictionless unconfined compression problem.

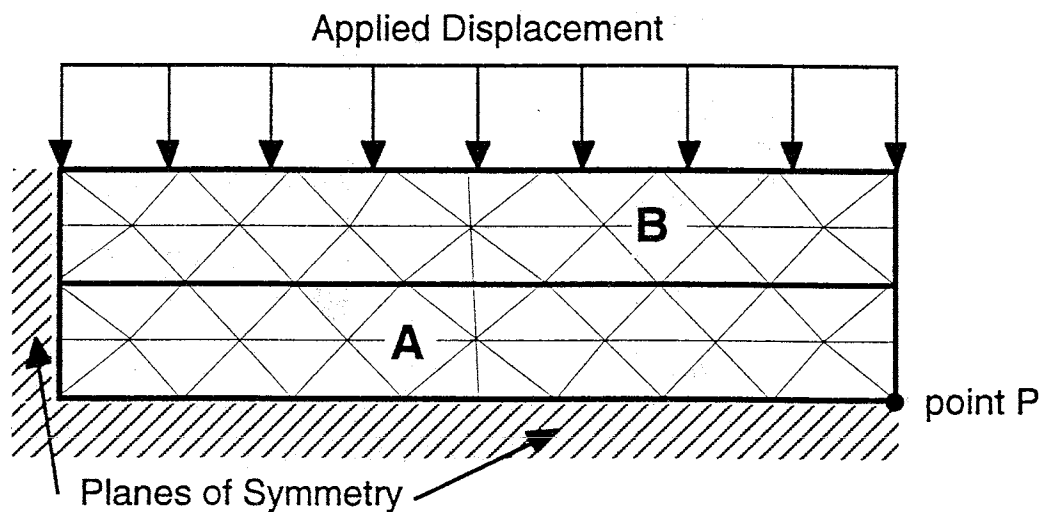


Fig. 6.2. Finite element mesh and boundary conditions for the unconfined compression problem.

To compare the overall accuracy of the contact formulation, the solid and fluid radial velocities at point 'P' of Fig. 6.1 are plotted in time in Fig. 6.3. This demonstrates that displacements applied to region 'B' are transferred through the contact surface to region 'A', and compares well with the values presented by Vermilyea [155] for an hybrid biphasic finite element. Of more interest are the displacements, velocities and stresses on the contact surface. Axial velocities are compared at  $t = 50s$  in Fig. 6.4, where the lines are solutions from the degrees of freedom on side 'A' and the symbols are from those on side 'B'. One would expect the velocities to be uniform through the width of the sample, and although there are slight variations depicted in the figure, these occur in the sixth significant digit and are not problematic. One can see that the kinematic continuity is exactly enforced for this case, since the lines and symbols coincide.

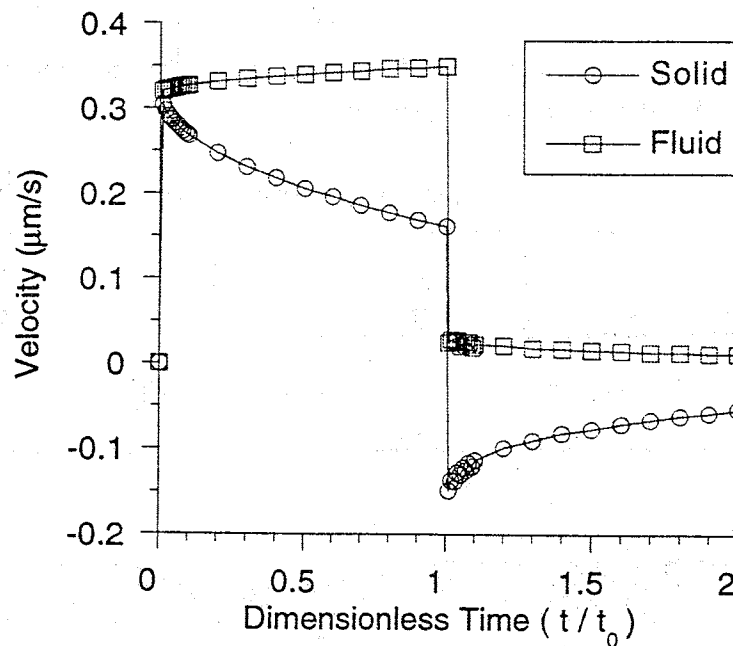


Fig. 6.3. Radial solid and fluid velocities at the half-height, point 'P', for the unconfined compression test.



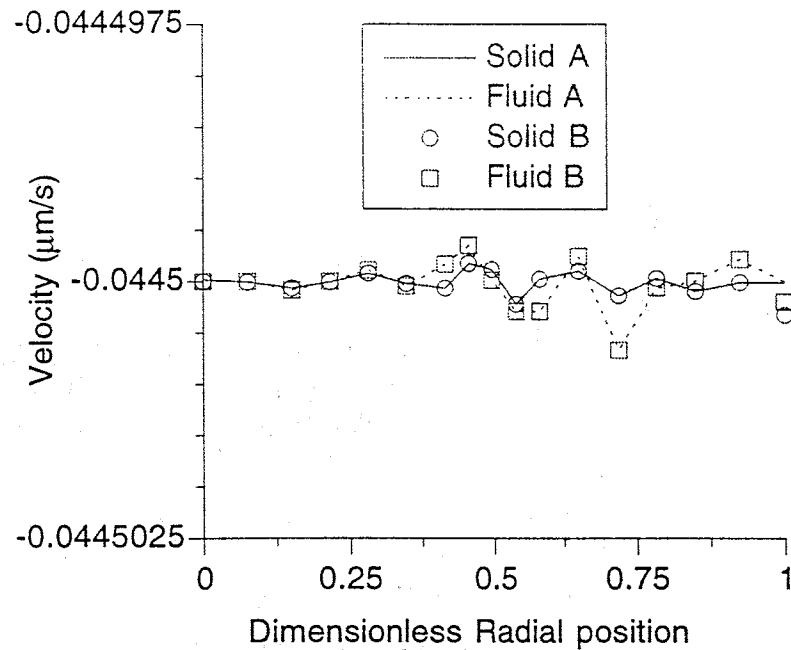


Fig. 6.4. Axial solid and fluid velocities along the contact surface at  $t = 50s$  for the unconfined compression test.

Figure 6.5 compares solid stresses and pressure along the contact surface, also at  $t = 50s$ . The figure shows stress at the nodes of each contactor segment (side 'A') plotted as a line, while those from the target segments are plotted as symbols. Recall from the derivation of the contact boundary conditions that when the solid content is continuous across a contact surface, the normal solid velocity, normal fluid velocity, solid normal traction and fluid pressure will each be continuous. For this problem the normal to the contact surface is in the axial direction, and the desired continuity is enforced. Also observe that the solid shear stress is zero along the contact surface, in agreement with the frictionless contact assumptions.

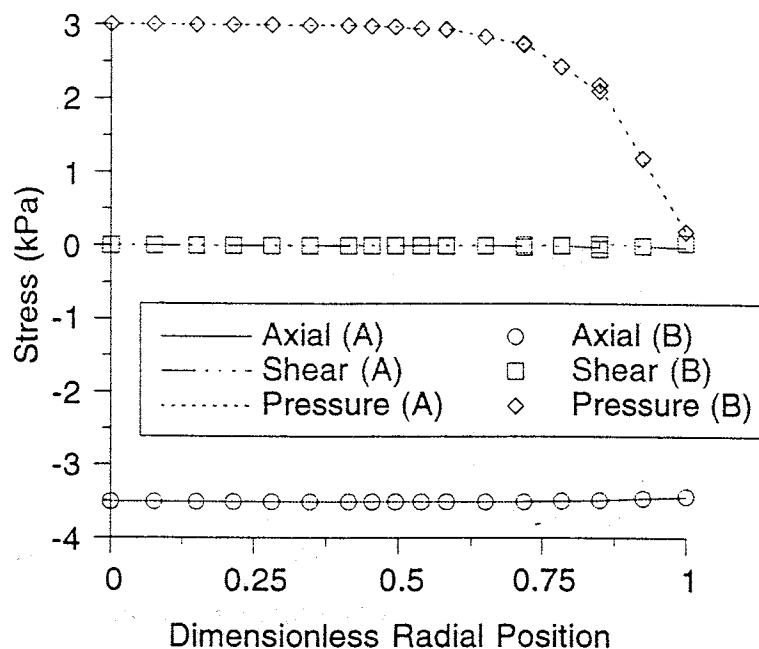


Fig. 6.5. Solid stress and fluid pressure along the contact surface at  $t = 50s$  for the unconfined compression test.

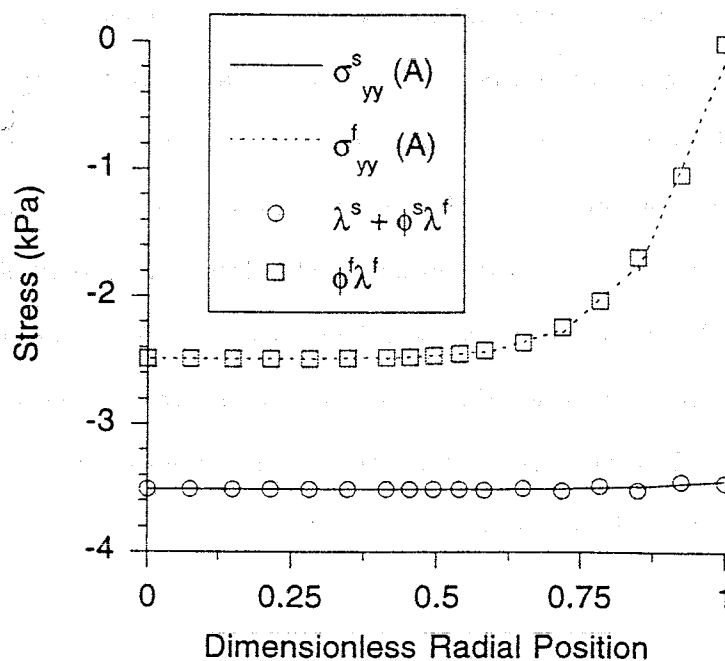


Fig. 6.6. Solid and fluid normal traction along the contact surface compared with the multipliers at  $t = 50s$  for the unconfined compression test.

In Fig. 6.6 the multipliers are compared to the normal components of solid and fluid traction on the contact surface. Since the multipliers are not directly identified with tractions, Eqns. (4.2-3) have been solved for traction in terms of the multipliers; this solution is reflected in the legend. Overall there is good agreement, though when plotted on finer scales, there is a difference of one percent between the smooth element stresses and the more oscillatory Lagrange multipliers.

The previous analysis is now repeated for materials with a discontinuity in the solid content across the contact surface. The lower portion of the model in Fig. 6.1, side 'A', is taken to have  $\phi^{SA} = 0.25$  and  $\phi^{SB} = 0.5$ . For most problems, one would expect that a jump in the solid volume fraction will produce a discontinuity in fluid velocity, as predicted by Eq. (2.40b). For unconfined compression however, the relative velocity is purely radial. This implies that the vertical components of both the solid and fluid velocity will be continuous, which also satisfies Eq. (2.40b). The stresses are dependent on pressure, which is continuous, and volume fraction, and will experience discontinuities as depicted in Fig. 6.7. Using the scale on the figure and Eqns. (2.40c,d) one can calculate that the required continuity of the stresses is enforced for this choice of volume fractions.

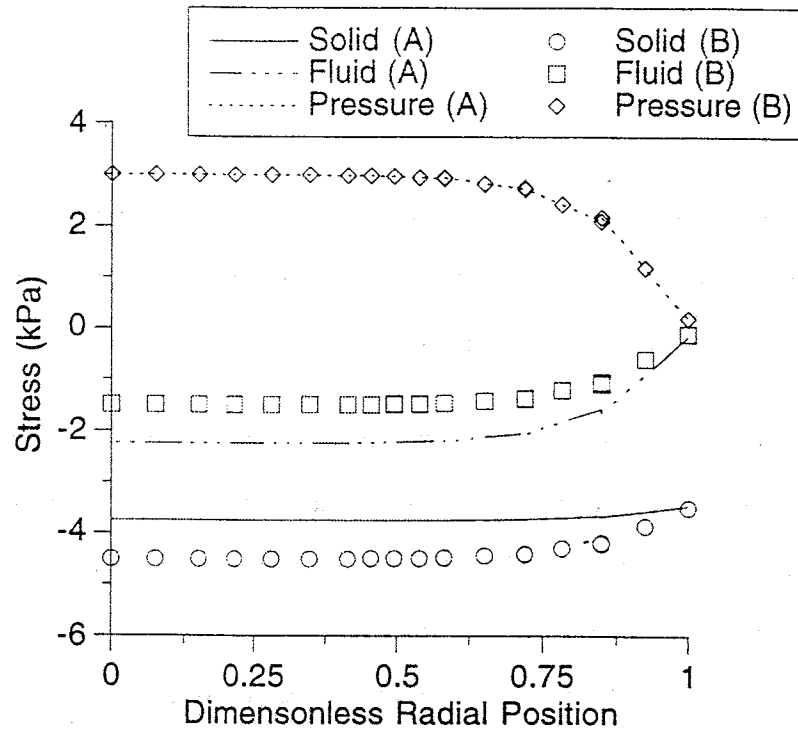


Fig. 6.7. Solid stress, fluid stress and pressure along the contact surface at  $t = 50s$  for the unconfined compression test with discontinuous volume fraction.

## Hertz Contact

The contact solutions developed by Hertz [59] are some of the only analytic results for evolving contact problems. As a demonstration of the discretization algorithm, the biphasic mixed-penalty contact finite element is used to solve the problem of a cylinder contacting an infinite medium. The problem is modeled in plane strain, and material parameters for the biphasic element must be chosen which will accurately simulate either rigid or linearly elastic materials. Figure 6.8 presents the geometric model, and Fig. 6.9 depicts the finite element mesh. There are 669 triangular elements and 1506 nodes, manually graded toward the contactor and target surfaces.

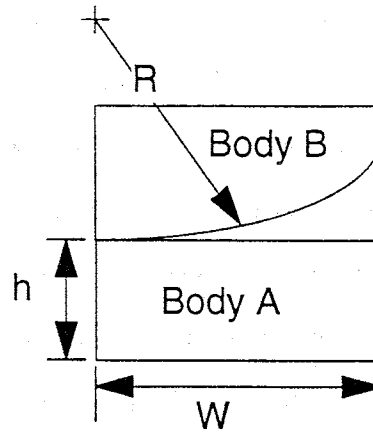


Fig. 6.8. Model geometry for the plane strain Hertz contact problem.

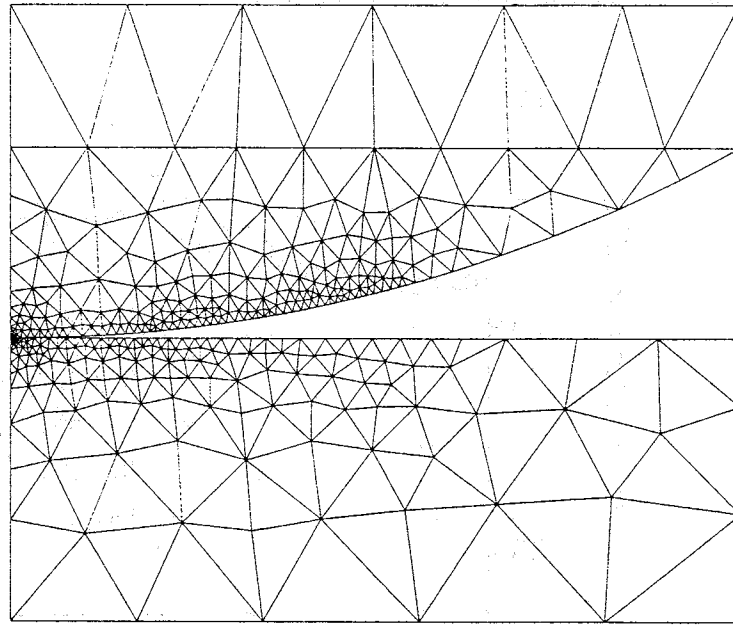


Fig. 6.9. Finite element mesh for the plane strain Hertz contact problem.

For this problem the flat surface of the foundation was chosen as the contactor and the curved surface of the cylinder was the target. Three combinations of materials are possible: both bodies elastic, an elastic cylinder contacting a rigid foundation or a rigid cylinder contacting an elastic foundation. Accurate solutions using a fixed mesh have been obtained for each case, demonstrating the invariance of the solution to the choice of the

master segments with regard to material properties and expected deformation. Results for the last case are presented here. The foundation is 2 mm in height and 5 mm in width, while the cylinder has a radius of 10 mm. Young's modulus for the foundation is 1.0 MPa and Poisson's ratio is  $1/3$ . Both the cylinder and foundation are designated as 95% solid, and made highly permeable so there is no resistance to fluid flow. This essentially uncouples the solid and fluid motions and allows one to recover the compressible elastic solution from the biphasic theory. The penalty parameter is chosen as  $1 \times 10^{10}$  for the foundation. A rigid material is given material properties making it 1000 times stiffer than the compliant materials surrounding it.

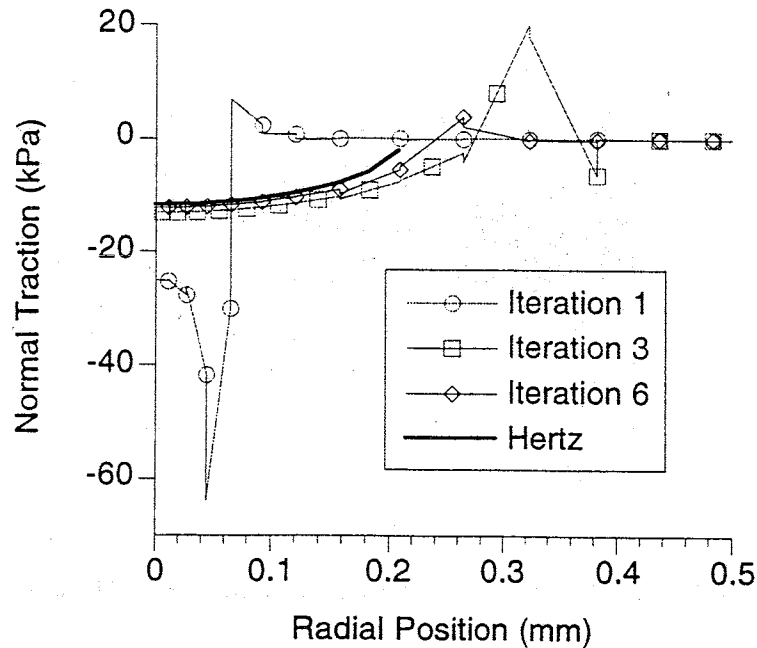


Fig. 6.10. Axial solid stress at several iterations of the contact surface for a total load of 4 N in the plane strain Hertz contact problem.

Figure 6.10 depicts the axial solid stress distribution on the surface of the foundation for several of the iterations required to converge when a total load of 4N is applied to the cylinder. Note that for this geometry, the axial direction will be the normal to

the contactor surface. Also in the figure is the accepted solution to this problem. The choice of a contact surface for the first iteration drastically underestimates the true contact surface. This prediction is made based only on the proximity of the contactor and target segments. The algorithm recognizes the material overlap that results, and adjusts the contact surface. This prediction now overestimates the surface. By the sixth iteration there is no change made to the presumed surface and the solution for contact radius and traction agrees with the accepted solution to within one contactor segment length. At each iteration quadrature points are made inactive when they have a positive normal traction. Observe in the intermediate iterations that near the edge of the contact region there is a rapid change in sign of the normal traction. These are contactor segments with only some active quadrature points, and the element is trying to represent both the contact pressure and the traction free surface. Mesh refinement would be required to further refine the definition of the contact radius and traction distribution.

The previous result was generated with the factor  $\alpha_c$  in the tolerance parameter, Eq. (5.3), chosen to be  $\alpha_c(0) = 0.01$  at  $t = 0$  and  $\alpha_c(t) = 0.0$  for  $t > 0$ . Table 6.1 shows that six iterations of the contact surface were required before the Kuhn-Tucker relations were satisfied. Different choices of the tolerance parameter result in different numbers of iterations to convergence. The table indicates the number of active contactor segments in the surface at each iteration. When the same value is indicated for subsequent iterations, the number of active quadrature points in the segment has been changed. Observe that when  $\alpha_c(0)$  is small, the initial contact surface is small, and that subsequent iterations overestimate the surface. The parameter  $\alpha_c(t)$  controls the proximity of points that will be brought into contact after the initial surface is chosen. A value of zero is an acceptable choice, though the program chooses a default of 0.0001. As this parameter becomes larger, there is increasingly more oscillation in the choice of segments to include.

Iteration Number	$\alpha_c(0) = 0.1$ $\alpha_c(t) = 0.0$	$\alpha_c(0) = 0.01$ $\alpha_c(t) = 0.0$	$\alpha_c(0) = 0.001$ $\alpha_c(t) = 0.0$	$\alpha_c(0) = 0.01$ $\alpha_c(t) = 0.001$
1	7	4	2	4
2	9	11	12	11
3		10	11	10
4		10	10	10
5		9	10	9
6		9	9	9
7			9	9

Table 6.1. Number of active contactor segments at each iteration of the contact surface for a range of settings of the tolerance parameter.

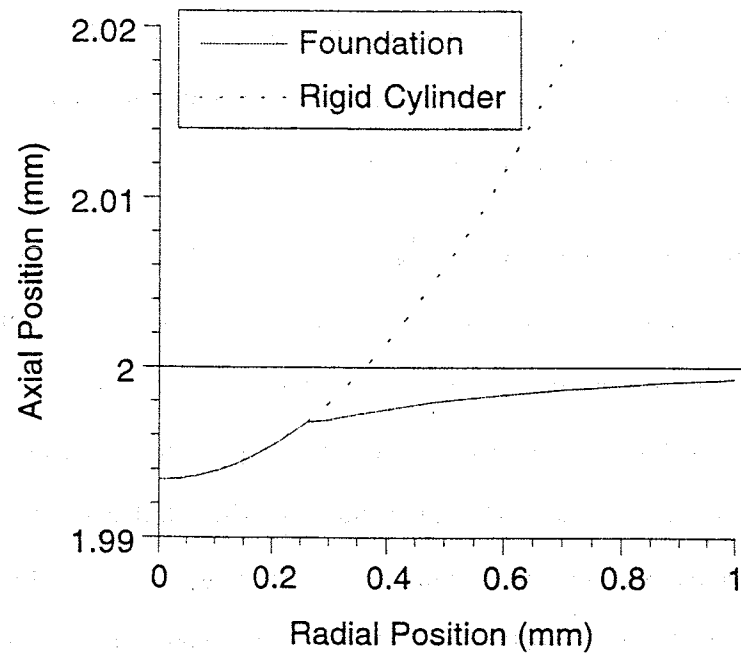


Fig. 6.11. Deformed surface geometry for a total load of 4 N in the plane strain Hertz contact problem.



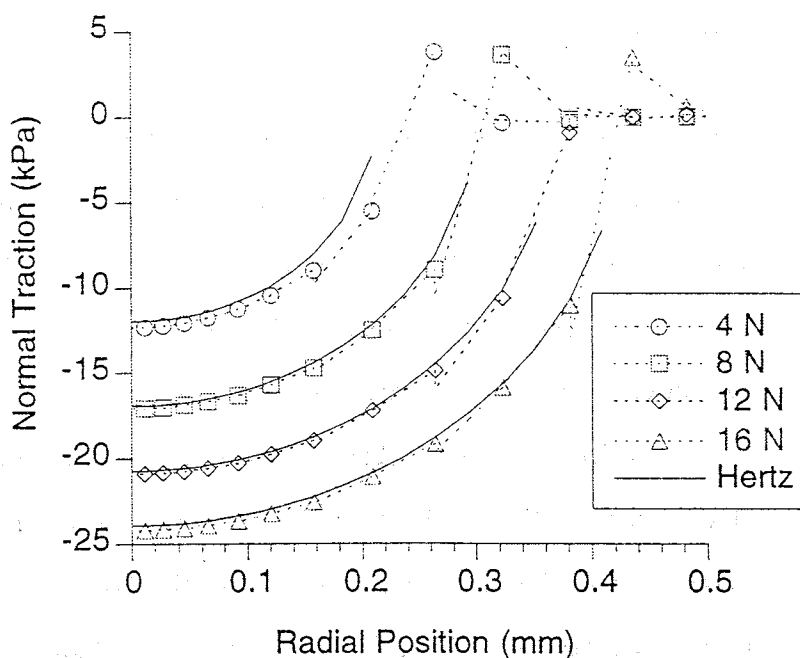


Fig. 6.12. Axial solid stress distributions for several applied loads in the plane strain Hertz contact problem.

Figure 6.11 displays the deformed surface geometry when the applied load is 4N. Observe that the cylinder does remain rigid, and that the foundation surface remains geometrically smooth. The accepted contact radius for this configuration is 0.213mm. While the elastic solution to Hertz contact is not time-dependent, the biphasic contact finite element formulation does discretize in time. For the elastic problem a force varying linearly with time is prescribed, and the solution at each time step is considered the elastic solution for that particular load level. Figure 6.12 compares the converged traction distributions at four load levels with the accepted solution. As the load increases, the discretization algorithm continues to correctly predict the extent of the contact surface, and hence the traction distribution.

## Biphasic Indentation

The previous examples show that the contact code is capable of both finding the correct contact surface, and enforcing the required continuity there. The next goal is to verify these two criteria for an evolving biphasic contact problem. There are limited solutions for this type of problem, an asymptotic solution presented by Ateshian *et al.* [13] and a more recent integral transform solution by Kelkar and Ateshian [73]. The geometry is as in the plane strain Hertz contact problem, but with geometric parameters  $h = 1\text{mm}$ ,  $W = 20\text{mm}$  and  $R = 100\text{mm}$ . Physically the problem represents two identical cylinders layered with a biphasic material in contact along the length of their axes. Because of the symmetry, a geometrical transformation reduces this to a shallow, rigid, impermeable cylinder indented into a thin biphasic layer. A creep problem is modeled where a load is applied to the cylinder at  $t = 0^+$  and held constant.

Following Kelkar's model, the material properties for the tissue layer are  $\lambda = 0.0$ ,  $\mu = 0.25\text{MPa}$ ,  $\phi^s = 0.25$ ,  $\kappa = 0.2 \times 10^{-14} \text{ m}^4/\text{Ns}$  and  $\beta = 1.0 \times 10^{10}$ . A distributed load equal to 1000N is applied to the rigid cylinder in one time step. Results are presented for times well beyond the application of load. This allows for differences between a true step load and the short ramp loading to decay. Figure 6.13 shows excellent agreement between the surface normal traction predicted by the integral transform solution (lines) and the finite element solution (symbols) at  $t = 100\text{s}$ . Similar correlations are observed for times from 20 to 200 seconds, and for kinematic variables. Observe that the fluid traction is nearly twice the solid traction. At much longer times, when fluid flow ceases, the pressure will be zero and the total load will be carried by the solid phase.

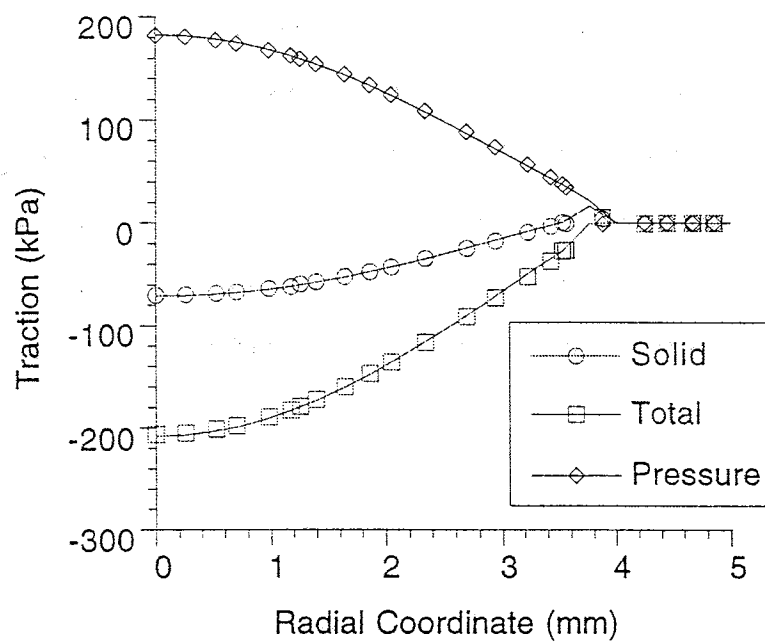


Fig. 6.13. Normal traction distributions for biphasic indentation after 100 seconds of creep. Lines are the integral transform solution and symbols are the finite element result.

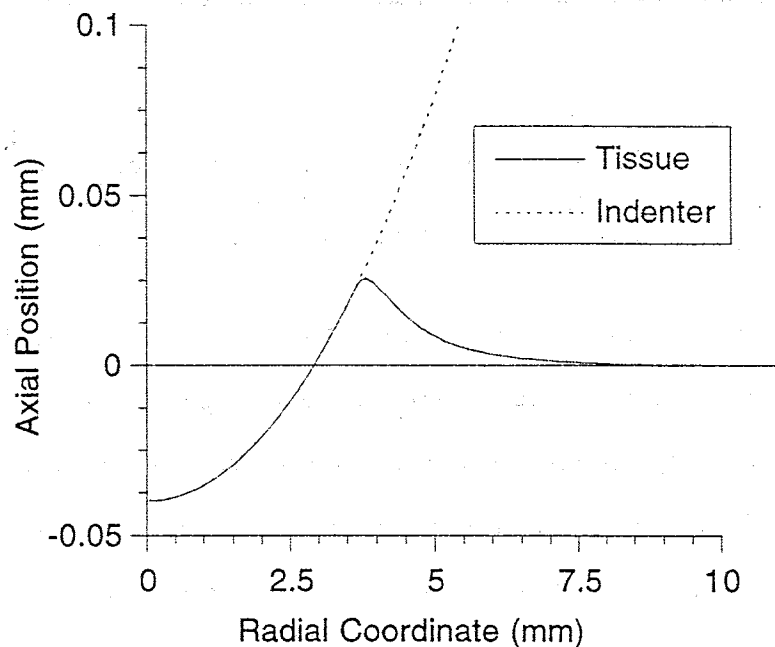


Fig. 6.14. Deformed surface for biphasic indentation after 100 seconds of creep.

In Fig. 6.14, note how the tissue surface has undergone a tensile deformation in the outer portion of the contact surface, also at  $t = 100\text{s}$ . This region also experiences an efflux of fluid, as depicted by the relative velocity in Fig 6.15. The maximum principal stress is shown as a shaded contour on a mesh deformed by five times the displacement; the scale is given in kilopascals at right. The magnitude and direction of the relative velocity field is indicated by the arrows, with magnitudes ranging to  $0.43\text{ }\mu\text{m/s}$ .

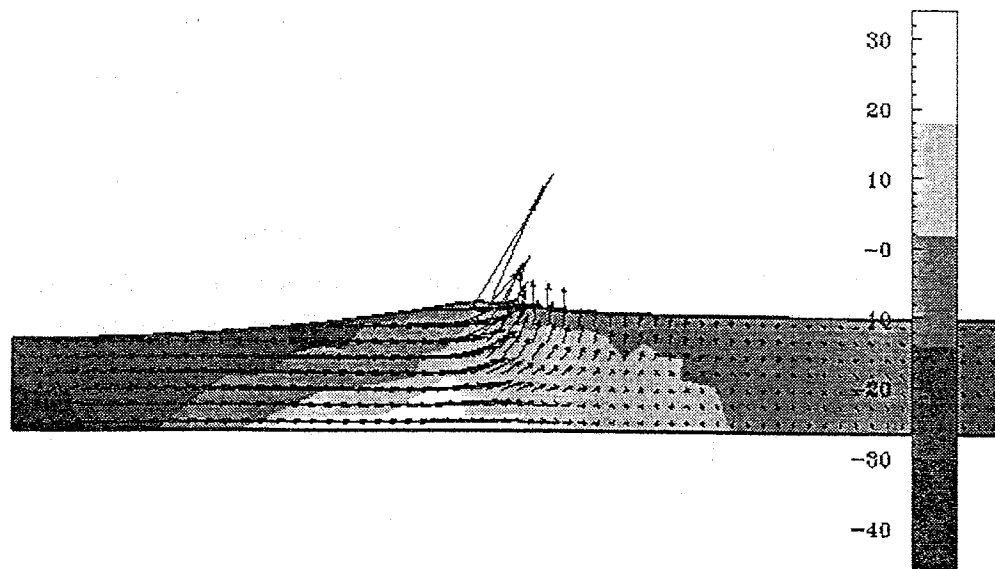


Fig. 6.15. Shaded contour of maximum principal stress in kPa for biphasic indentation. Solutions are on a  $5\times$  deformed mesh after 100 seconds of creep. The relative velocity field is indicated by arrows.

For the purpose of visualizing the solution, the program Data Explorer [69] is used. It is extremely powerful, but requires certain simplifications for finite element data. First, it can only represent a linear variation between the points of its connection elements. Thus, for the six-node triangle, only data values at finite element vertices are used. Alternatively, one could define four sub-elements to each triangle. Neither method depicts the true spatial variation of the finite element interpolations. Second, it is not capable of interpolating data from points other than the vertices. For derivative quantities,

which are typically evaluated at the Barlow points [22] within an element, some smoothing is necessary between elements. Currently a direct nodal averaging is used. In the future, more sophisticated techniques may be implemented, such as  $L_2$  smoothing [107] or patch recovery [166]. In the present case the finite element mesh is sufficiently fine that the visualization does not incur any appreciable error. All subsequent contour plots or vector distributions should be viewed with this fact in mind, however.

## Clinical Demonstrations

Two examples which demonstrate the applicability of the biphasic contact finite element to problems of clinical significance are presented. Axisymmetric models of the gleno-humeral joint (GHJ) of the shoulder and tibio-femoral joint of the knee are selected since they can be analyzed under the linear assumptions used in the present element. These are problems which will benefit greatly from recent advances in data collection [12,14] for and finite element mesh generation [122,123,137,141] of physiological geometries, as well as from three dimensional and nonlinear analysis techniques being developed [6,7].

### Gleno-Humeral Contact

An axisymmetric model of the GHJ is developed from stereophotogrammetric data by choosing the sphere which most closely approximates the true surface geometry [133]. Average values of the radius of curvature for both the bone and cartilage surfaces of the humeral head and glenoid cavity of male specimens are reported in Table 6.2. Along with these are average material properties; all values are from Soslowsky [133].

	Glenoid	Humeral Head
Cartilage Radius (mm)	26.37	26.85
Bone Radius (mm)	34.56	26.10
$\lambda$ (MPa)	0.01146	0.0295
$\mu$ (MPa)	0.274	0.265
$\kappa * 10^{-15}$ (M <sup>4</sup> /Ns)	1.16	1.70
$\phi^S$	0.2	0.2

Table 6.2. Average material and geometric properties for human cartilage in an axisymmetric model of the gleno-humeral joint, from [133].

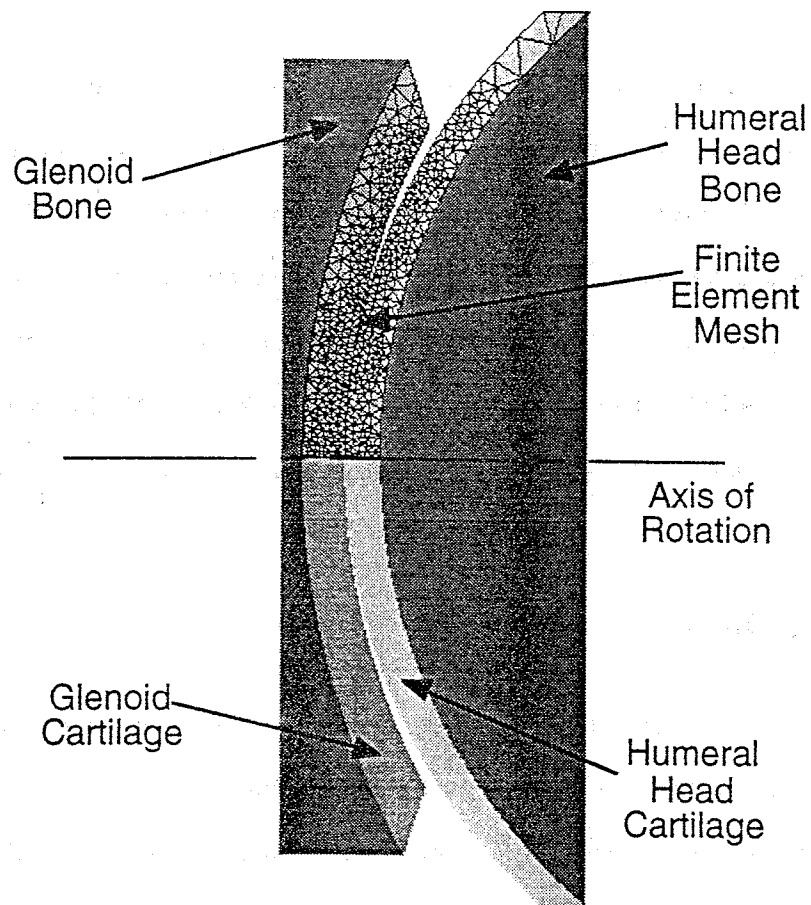


Fig 6.16. Model geometry and finite element mesh for the axisymmetric GHJ.

The geometric model and a finite element mesh of 1128 quadratic triangular elements and 2536 nodes are depicted in Fig. 6.16. A distributed load whose magnitude

increases linearly to 100N in one second is applied to the humeral head along the axis of rotation, while the glenoid bone is held fixed. This level of load is then maintained for an additional one second.

The contact surface establishes itself immediately as the load is applied, and remains nearly constant in size during the creep phase. Figure 6.17 shows that on the contact surface a majority of the load is supported by the fluid stress. This behaviour matches the prediction by Hou *et al.* [64], who state that the applied load is distributed between the phases according to the volume fraction.

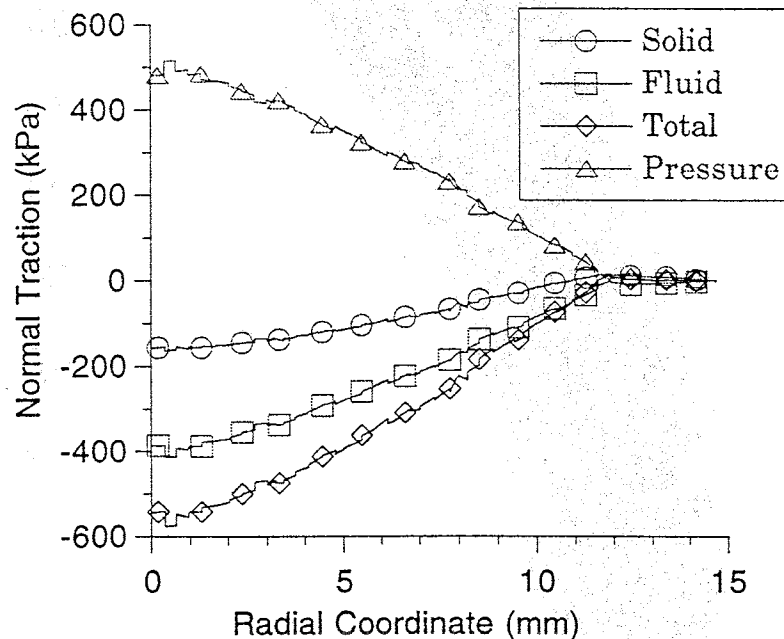


Fig. 6.17. Normal tractions *verses* radial coordinate after one second of creep for points along the glenoid surface.

Results are displayed as shaded contours over the deformed geometry at one second. At this time, approximately 80% of the glenoid surface is in contact with the humeral head. As with the spherical indentation problem, the tissue experiences significant tensile stresses, despite the purely compressive loading. In the presence of a

large fluid pressure, elastic stress (that stress coming from the deformation of the solid matrix, see Eq. (2.39b)) is a more meaningful measure of the stress state in the solid matrix. Thus, Figs. 6.18 and 6.19 display the maximum and minimum elastic principal stresses in the tissue layers.

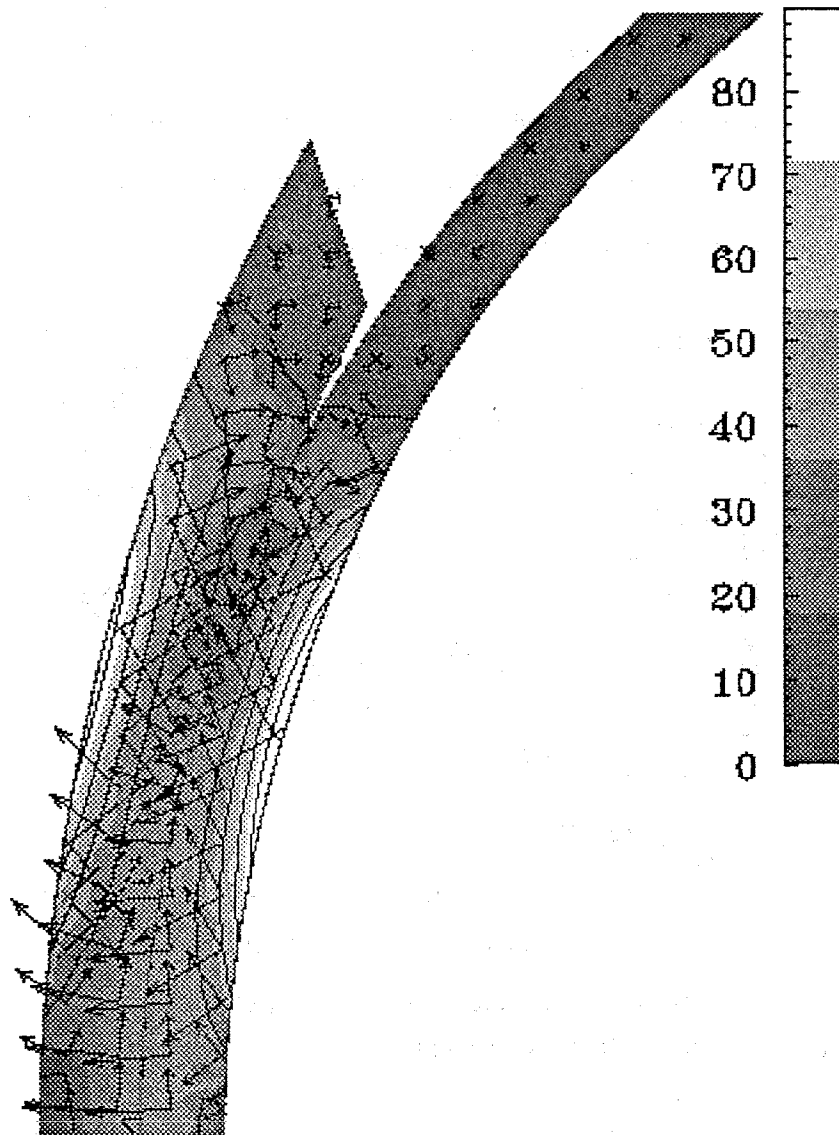


Fig. 6.18. Shaded contour of the maximum principal elastic stress in kPa in the GHJ after one second of creep. Magnitude and direction of the in-plane principal stresses indicated by arrows.



Figure 6.18 also displays arrows representing the magnitude and direction of the in-plane principal elastic stresses. These figures indicate that every point in the tissue experiences a tensile elastic principal stress. Also observe that both the peak positive and negative principal stresses occur at the cartilage-bone interfaces. This implies that the shear stress will be maximum at these locations.

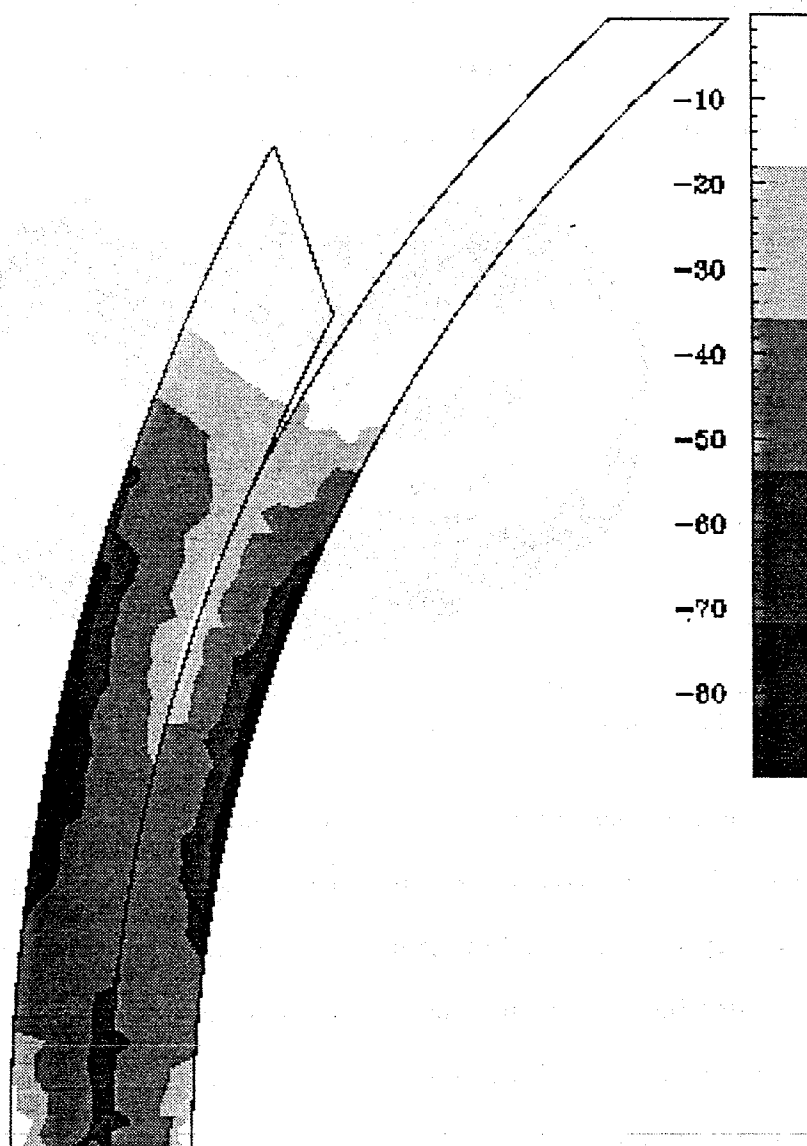


Fig. 6.19. Shaded contour of the minimum principal elastic stress in kPa in the GHJ after one second of creep.

## Tibio-Femoral Contact

The knee is perhaps one of the most interesting diarthrodial joints in the body, as well as one of the most complex. Referring to Fig. 6.20, the articulation between femur, meniscus and tibia is certainly not axisymmetric. For the present investigation, however, two axisymmetric models will be developed as a demonstration of the capabilities of the biphasic contact finite element. Of primary interest is the ability of the code to simultaneously follow advancing contact with multiple pairs of contact surfaces.

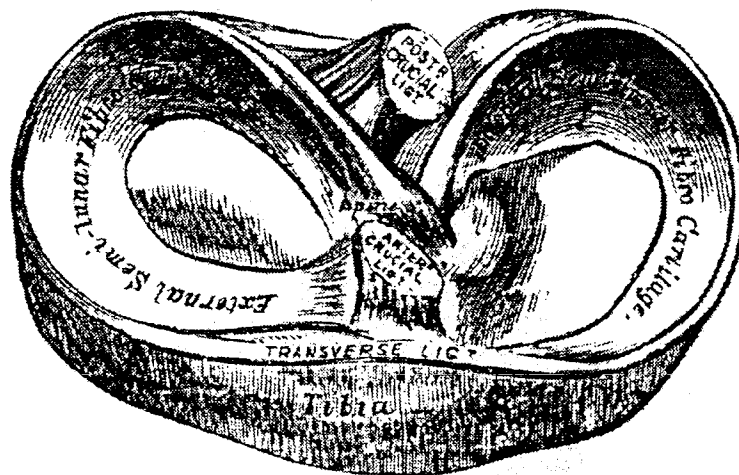


Fig. 6.20. Tibial surface of the knee showing the menisci and several major ligaments, from [51].

The two models represent different views of the meniscal geometry on the tibial surface. The first treats the femur as spherical and considers a single meniscus surrounding it. The second recognizes the femoral condyles and analyzes one condyle in contact with the surrounding meniscus. The primary differences in the models are the distance from the axis of symmetry to the inner radius of the meniscus, and the geometry of the distal femur.

Figure 6.21 displays the parametric geometry for the axisymmetric model of the knee. Tibial cartilage is modeled as a rectangular region rigidly attached to the underlying, impermeable bone and frictionless at its top surface. Femoral cartilage is modeled by a cubic curve passing through points 'A' and 'B' in the figure, and tangent to the meniscus and tibia, respectively, at those locations. The femur is treated as rigid and impermeable. Cartilage thickness values are averages obtained from stereophotogrammetry [14]. The tibial surface of the meniscus is flat, while the outer and femoral surfaces are quadratic. This geometry was used previously for a parametric study of the meniscus with loads applied to the solid and fluid phases, and normal to the femoral surface [138]. Table 6.3 gives values of the various geometric parameters for the two different models of the knee. Model 1 corresponds to a spherical geometry for the distal femur and a single meniscal ring, while Model 2 considers only one condyle.

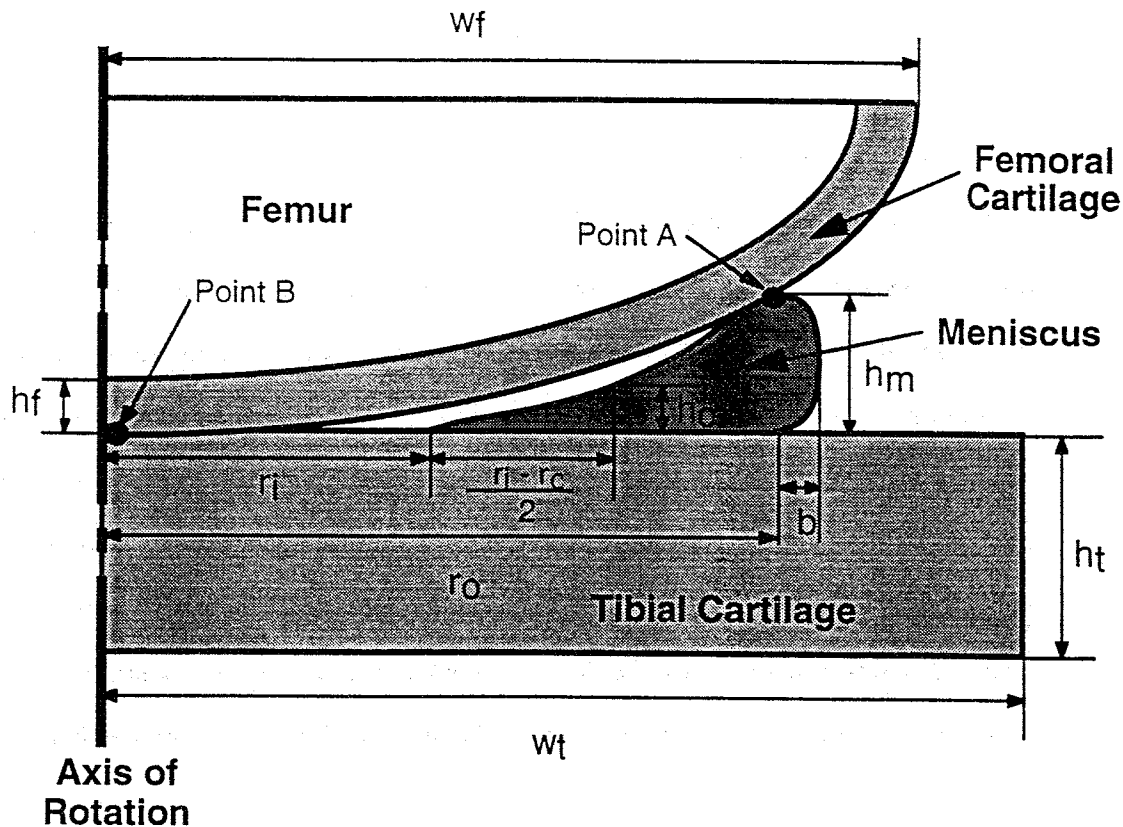


Fig. 6.21. Parametric geometry for axisymmetric, three-body meniscus-femur-tibia contact.

Isotropic material properties are selected for cartilage, while a transversely isotropic constitutive law is used for the solid phase of the meniscus. Isotropic values are averages reported by Mow *et al.* [96] and the transversely isotropic values are those reported by Proctor *et al.* [117] and also used by Spilker, Donzelli and Mow [138] in a previous meniscus study. In the transversely isotropic meniscus, fibers are assumed to be oriented circumferentially, and will provide a stiffening effect to the tissue. In Model 1, a total load increasing linearly in time from zero to 350N at  $t = 1s$ , is applied axially to the femur. In model 2 the stress level is held constant, while the area has decreased, resulting in 176N at  $t = 1s$ . This level of stress is consistent with values measured by Ahmed and Burke [3].

		Model 1	Model 2
Inner radius	$r_i$	15.0	5.0
Outer radius	$r_o$	30.0	20.0
Meniscal bulge	$b$	1.5	1.5
Center height	$h_c$	2.25	2.25
Meniscal height	$h_m$	6.0	6.0
Tibial width	$w_t$	35.0	25.0
Tibial height	$h_t$	5.0	5.0
Femoral width	$w_f$	35.0	25.0
Femoral height	$h_f$	2.0	2.0

Table 6.3. Geometric parameters for two axisymmetric models of three-body meniscus-femur-tibia contact. Values are given in mm.

As with other biphasic contact problems, the contact area develops rapidly, and all surfaces come in contact within the first half of the loading cycle. During this time, the discretization algorithm correctly detects contact between the femur and tibia, tibia and meniscus, and meniscus and femur. Figure 6.22 displays contour plots of axial compressive strain at  $t = 1s$  on the deformed geometry for both models of the knee joint. Overall the distributions are quite similar. In Model 1 there is a greater compressive strain in the region of contact between the tibia and femur. For the particular geometry chosen in Model 1, this region supports nearly twice the load seen in the meniscus-tibia contact. The peak compressive strains are seen at the outer radius of the meniscus, along the tibial surface. Values are localized to that point, and are most certainly an artifact of the sharp geometric corner. Of clinical interest are the tensile strains at the inner radius and bulged region of the meniscus. These tensile strains may be indicative of regions susceptible to tears [9].

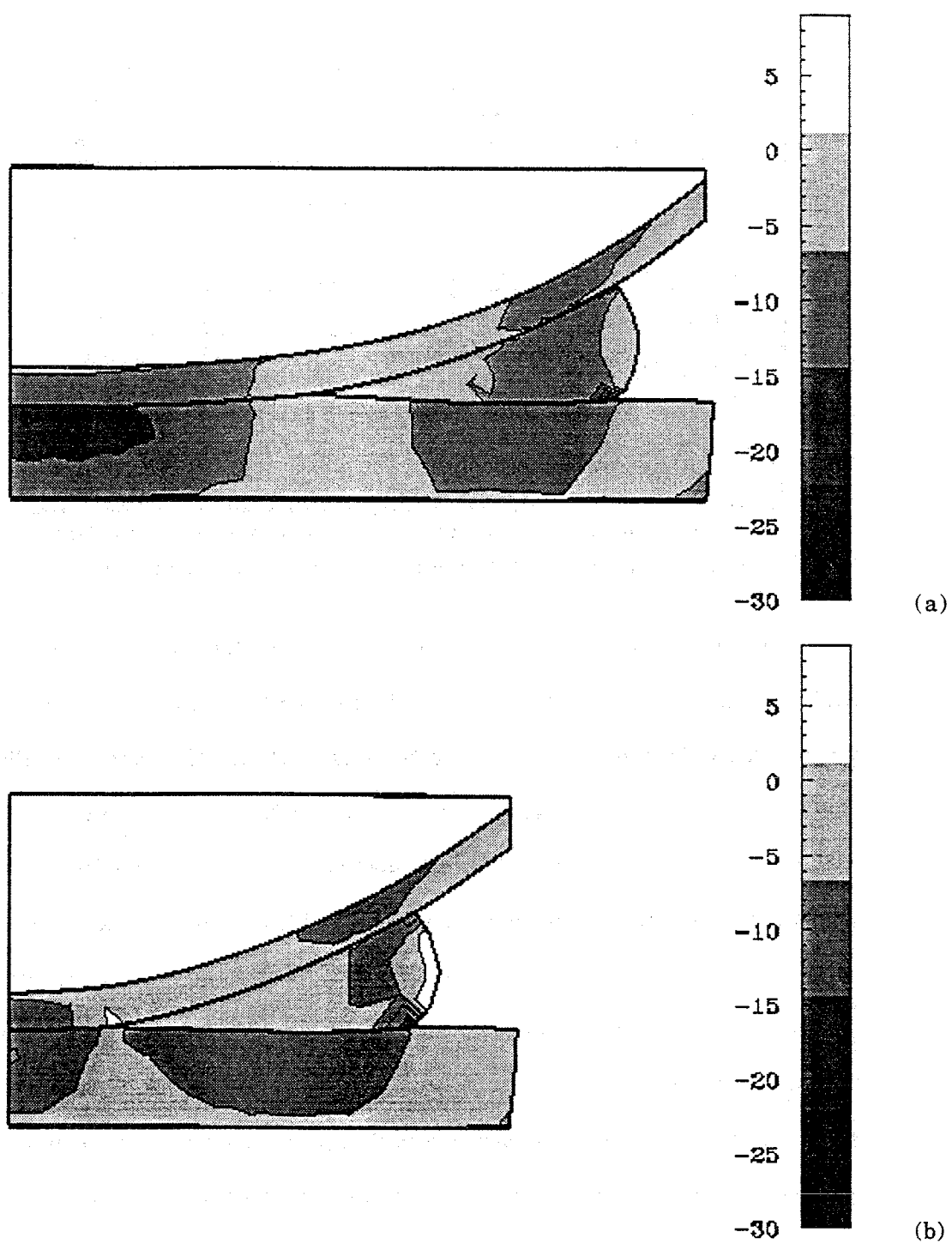


Fig. 6.22. Axial compressive strain in percent at  $t = 1s$  for axisymmetric, three-body meniscus-femur-tibia contact: (a) Model 1 and (b) Model 2. Values are not reported for the femur.

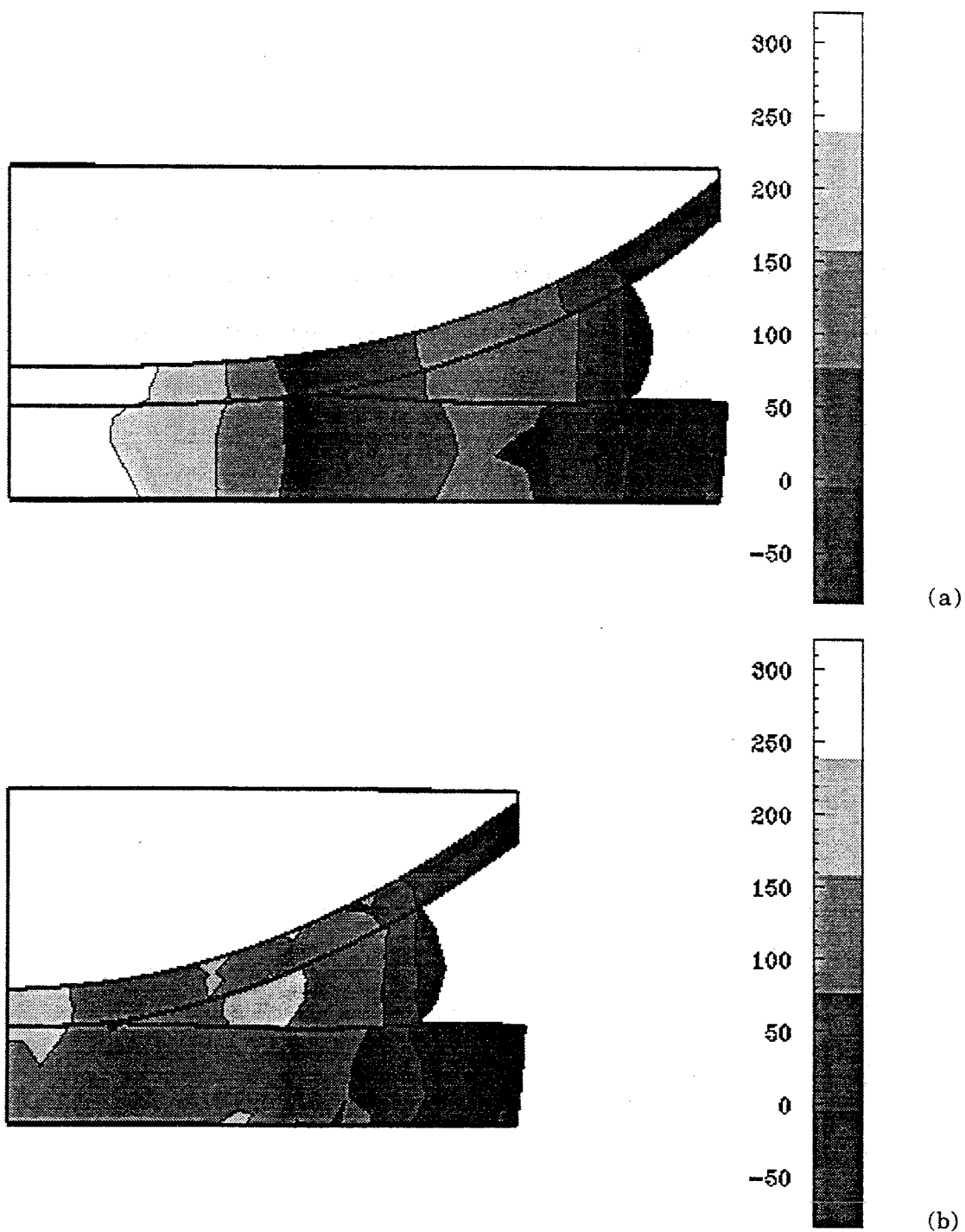
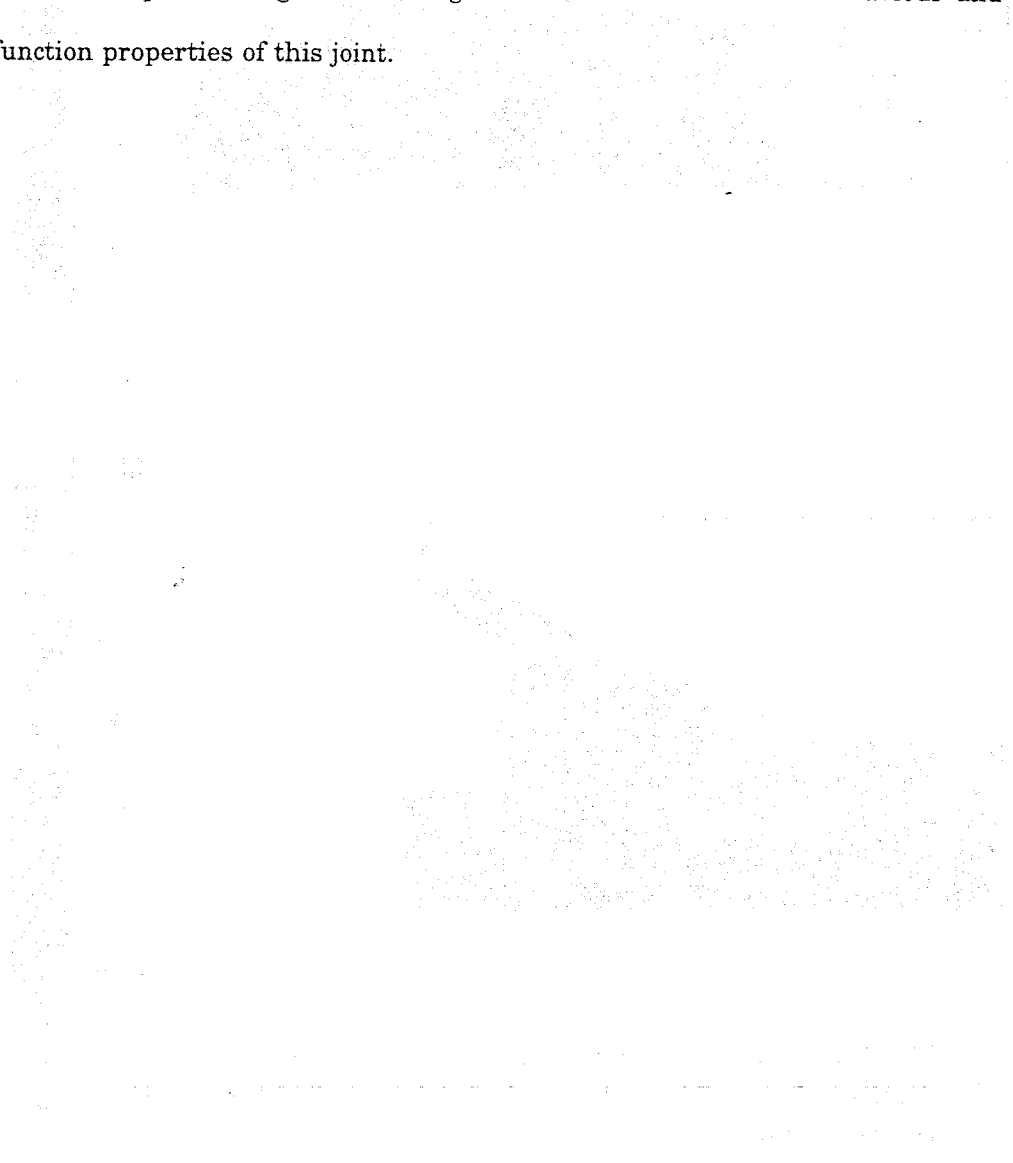


Fig. 6.23. Fluid pressure in kPa at  $t = 1s$  for axisymmetric, three-body meniscus-femur-tibia contact: (a) Model 1 and (b) Model 2. Values are not reported for the femur.

Figure 6.23 displays contour plots of fluid pressure at  $t = 1s$  in both models of the knee. Higher pressures are observed in Model 1 where there is an extended region of contact between the tibia and femur. In either case, this pressure develops rapidly as the mating tissue surfaces come into contact, effectively limiting fluid exudation. While the data presented is for simplified models of the knee, extensive parametric variation in the future can provide significant insight into the deformational behaviour and structure-function properties of this joint.





# Chapter VII: Summary and Concluding Remarks

## Summary

A contact formulation based on the mixed-penalty biphasic finite element [139] has been derived from a weighted residual statement. In addition to the customary governing equations for hydrated soft tissues [96], the conditions of contact [64] have been included as weighted integrals over an assumed contact surface. Significant efforts have been made in this research to develop an efficient means of introducing the contact constraints into the formulation, and to determine the correct contact surface on which to enforce these conditions.

The present formulation, while valid for two- or three-dimensional analysis, has been implemented only for the six-node triangle. In addition, the formulation is based on the fully linear form of the biphasic theory, where the solid matrix is governed by a linear constitutive law and volume fraction and permeability are not dependent on deformation. Boundary conditions on the contact surface have been simplified to account for these assumptions, as well as for the assumption of frictionless contact. A Lagrange multiplier approach was selected to enforce the contact conditions. By examining the contact formulations for single phase elasticity, a weighted residual Lagrange multiplier method was developed for the biphasic contact finite element formulation. The finite element equations are written for an assumed contact surface, and iterations must be performed to find that surface which is physically admissible, in addition to satisfying the contact boundary conditions. An iteration algorithm based on the contact surface kinematics and kinetics at the Gaussian quadrature points of finite elements on the model boundary was

implemented. This contact surface discretization is directly extensible to three-dimensional analysis with either hexahedra or tetrahedra.

Two series of example problems were presented. The first consists of tests with known solutions which isolate different aspects of the formulation and numerical implementation. The biphasic contact finite element has successfully solved each of these test cases, thus validating the formulation and implementation. A second class of examples illustrates how this element may be used for challenging problems of clinical significance. Axial compression of the gleno-humeral and tibio-femoral joints, while simplified loading protocols, can provide insight into the deformational behaviour of cartilage. These examples further demonstrate the importance of fluid effects in tissue mechanics.

## **Comments on Element Performance**

Overall the mixed-penalty contact finite element is capable of providing accurate solutions to a wide range of contact problems. There are some limitations of which an analyst should be aware. These are rapid rates of loading, modeling rigid or elastic materials and mesh refinement. Each will be discussed in turn in the following paragraphs.

As indicated in the presentation of the spherical, biphasic indentation problem, very rapid rates of loading can be problematic. First, if too severe, they can cause material deformations beyond the limits of applicability of the linear theory. Within the linear regime, it is still possible to achieve non-physical solutions due to a contact surface that is drastically underestimated. In this situation, traction results may dictate that points within the contact surface be released, while overlap conditions indicate that points need to

be added. The result is that a 'hole' may develop in the surface. In general this will correct itself, however the experience to date indicates that the most reliable solutions are obtained when the initial estimate of the contact surface is greater than the true surface. This can be achieved by varying the input parameter  $\alpha_c$  at  $t = 0$  over one to two orders of magnitude and observing the converged solutions at the initial time step. With the correct choice the program can be allowed to continue unattended for the duration of the time scale of the problem. Default values of the contact parameters are chosen by the program and would be appropriate for most ramp-type loadings.

Rigid materials modeled with the biphasic elements present problems independent of the contact boundary conditions. As one approaches the limits of solid content or permeability, poor numerical performance may affect the solution. When both compliant and rigid materials are present in the same mesh, direct solution strategies may become ill conditioned, and the analyst must be aware of this possibility. In general, rigid materials are defined by increasing the solid moduli by two to three orders of magnitude above the surrounding materials. Permeable or impermeable interfaces are created by respectively increasing or decreasing the permeability coefficient by two to three orders of magnitude.

With regard to the contact element, rigid or compressible elastic materials on the contact surface may pose additional problems. In the Hertz problem the solution was declared independent of the choice of the contactor and target edges. Indeed, for the case presented, the solution was in good agreement with the analytical result. With a rigid material on the contactor surface however, it may be possible to have kinematic solutions with the correct continuity, but with small variations. With high moduli, these can be amplified into significant variations in traction. As a result, the discretization algorithm

may release quadrature points based on these erroneous tractions. Often only one quadrature point in the contact element will be released, not significantly affecting the solution. The analyst should be aware of this possibility, and should choose the rigid materials to be target surfaces whenever possible.

One can obtain the quasi-static response of a compressible elastic material with the biphasic theory by choosing a high permeability and a solid content near unity. If time-dependent boundary conditions are applied, the solution at any time can be considered the quasi-static response at that particular load level. With these choices, solid displacement is accurate and pressure is several orders of magnitude smaller than the elastic stress. Values of the solid and fluid velocities are not physically relevant, although the latter can be quite large. When solving contact problems with elastic materials, this large fluid velocity may cause a difficulty by virtue of its contributions to the right hand side through the time discretization. Because the fluid velocity may be larger than the solid velocity by one or two orders of magnitude, any numerical inaccuracy in the satisfaction of the contact boundary conditions becomes significant. In extreme cases, these terms will accumulate and may cause the contact algorithm to degrade. In practice, this limitation is not significant, since bone is modeled as rigid and impermeable. Alternatively, if one requires the elastic response, it is straightforward to implement the appropriate element formulation within the biphasic finite element code.

Obviously, an intelligent choice for the finite element mesh makes the contact solution progress more smoothly. An ideal solution uses adaptive mesh refinement to enrich the discretization in zones where contact is actively advancing or receding. Observations of the finite element stresses on the contact surface indicate that error estimators utilizing smooth projections of the stresses will call for mesh enrichment in

these regions. When adaptive meshing procedures are not available, the user must realize that the contact surface can be predicted to within only one element length. Depending on the type of problem being modeled, more or less refinement may be required on the contact surfaces.

## Future Directions

With the success of the first biphasic contact finite element formulation, several opportunities to increase the sophistication of diarthrodial joint modeling become apparent. The single most important tool in developing a complete simulation of articulation is three-dimensional finite element analysis of contact. While the present formulation could be implemented with a three-dimensional element, several other enhancements are required to make this element useful in clinically relevant problems.

Certainly paramount are finite deformation and material nonlinearity. Large-displacement, sliding contact, which is observed in every diarthrodial joint, cannot be modeled within the confines of geometric linearity. Obviously, the material nonlinearities represent tissue behaviour which is observed during *in vitro* tissue tests, and must be included in the model to obtain a physically meaningful solution. The effects of material and geometric linearity have been included in recent work by Almeida [6]. In the course of that research, two- and three-dimensional elements have been implemented for the mixed-penalty and velocity-pressure formulations. It is possible that frictional effects on the contact surface play an important role in the overall deformational behaviour. Additional experimental research is required to quantify this effect and to postulate the laws that may govern it for tissue mechanics. Once nonlinearity has been implemented, computational efficiency becomes a significant issue.

As the biphasic finite element analysis code is extended and applied to physiologically relevant problems, it rapidly exceeds the computational resources of the most powerful workstations. It is essential that all of the new implementations be designed for a parallel architecture. Currently parallel implementations of platform-independent software tools for mesh generation, matrix solution and data handling have been developed by researchers in collaborating groups. There are many more tasks within the biphasic code that will have to be addressed though, including parallel stiffness calculation, fast searching algorithms for contact, parallel error calculations and time integration. A complete knowledge of a portable message passing library will be needed to make these modifications. Parallel implementations of the biphasic analysis software will become a major part of future research.

Once the transition to nonlinear analysis has been made, alternative formulations for the contact boundary conditions must be evaluated. For instance, the augmented Lagrangian approach becomes more attractive when matrices must be reformulated during iterations of a nonlinear solver. At the same time, in the context of a parallel computing platform, hybrid or pressure-velocity elements may have advantages over the mixed-penalty formulation, and should be re-evaluated.

Any numerical analysis technique should be capable of providing some measure of the error in the numerical approximation. For the examples presented here, this has been the traditional approach of a convergence study; the finite element mesh is refined until solutions on subsequent meshes are the same. In the future the biphasic contact finite element should be coupled with error estimation techniques and automatic mesh enrichment. Error estimates for parabolic system of equations have been developed (see, for example, [2,70,71,94]), and research has been conducted on error analysis for porous

soils using Biot's equations [104,105]. A research effort focused on extending these error estimates specifically to the linear and nonlinear forms of the biphasic theory is necessary. This must be coupled to related work on  $h$ ,  $p$  or  $h$ - $p$  adaptivity. Certainly, these tasks must also be developed with a parallel computing platform in mind.

Any future research in biphasic finite element analysis will build upon the many existing formulations, so it is important that these elements be applied to as many varied physiological problems as possible. This serves many purposes, but most of all it advances the understanding of the nature of joint mechanics and articular cartilage. Through this process researchers can identify those areas requiring increased theoretical, experimental or computational understanding.





## References

1. Adams, M. E., and Hukins, D. W. L., "The extracellular matrix of the meniscus," in *Knee Meniscus: Basic and Clinical Foundations*, Mow, V. C., Arnoczky, S. P. and Jackson, D. W., ed., New York, Raven Press, pp. 15-28, 1992.
2. Adjerid, S., Flaherty, J. E., Moore, P. K., and Wang, Y., "High-order adaptive methods for parabolic systems," *Physica D*, **60**, pp. 94-111, 1992.
3. Ahmed, A. M., and Burke, D. L., "In-vitro measurement of static pressure distribution in synovial joints - part I: Tibial surface of the knee," *Journal of Biomechanical Engineering*, **105**, pp. 216-225, 1983.
4. Akizuki, S., Mow, V. C., Muller, F., Pita, J. C., Howell, D. S., and Manicourt, D. H., "Tensile properties of knee joint cartilage: I. Influence of ionic condition, weight bearing, and fibrillation on the tensile modulus," *Journal of Orthopaedic Research*, **4**, pp. 379-392, 1986.
5. Akizuki, S., Mow, V. C., Muller, F., Pita, J. C., Howell, D. S., and Manicourt, D. H., "Tensile properties of knee joint cartilage: II. Correlations between weight bearing and tissue pathology and the kinetics of swelling," *Journal of Orthopaedic Research*, **5**, pp. 173-186, 1987.
6. Almeida, E., "Finite Element Formulations for Biological Soft Hydrated Tissues Under Finite Deformation," PhD thesis, Department of Mechanical Engineering, Aeronautical Engineering and Mechanics, Rensselaer Polytechnic Institute, 1995.

7. Almeida, E. S., and Spilker, R. L., "Linear and nonlinear three-dimensional finite elements for biphasic continuum applied to soft hydrated tissues," in *Second World Congress of Biomechanics*, Blankevoort, L. and Kooloos, J. G. M., ed., Nijmegen, Stichting World Biomechanics, pp. 215, 1994.
8. Armstrong, C. G., Lai, W. M., and Mow, V. C., "An analysis of the unconfined compression of articular cartilage," *Journal of Biomechanical Engineering*, **106**, pp. 165-173, 1984.
9. Arnoczky, S. A., Adams, M., DeHaven, K., Eyre, D. R., and Mow, V. C., "Meniscus," in *Injury and Repair of the Musculoskeletal Soft Tissue*, Woo, S. L.-Y. and Buckwalter, J. A., ed., Chicago, American Academy of Orthopaedic Surgeons, pp. 483-537, 1988.
10. Ascenzi, A., "Biomechanics and Galileo Galilei," *Journal of Biomechanics*, **26:2**, pp. 95-100, 1993.
11. Ateshian, G., and Wang, H., "Theoretical analysis of the moving contact of biphasic cartilage layers," in *Advances in Bioengineering*, Askew, M. J., ed., New York, ASME, pp. 141-142, 1994.
12. Ateshian, G. A., "A least-squares B-spline surface-fitting technique for articular surfaces of diarthrodial joints," *Journal of Biomechanical Engineering*, **115**, pp. 366-73, 1993.
13. Ateshian, G. A., Lai, W. M., Zhu, W. B., and Mow, V. C., "An asymptotic solution for two contacting biphasic cartilage layers," *Journal of Biomechanics*, **27:11**, pp. 1347-1360, 1994.

14. Ateshian, G. A., Soslowky, L. J., and Mow, V. C., "Quantitation of articular surface topography and cartilage thickness in knee joints using stereophotogrammetry," *Journal of Biomechanics*, **24:8**, pp. 761-776, 1991.
15. Athanasiou, K. A., Agarwal, A., and Constantinides, G., "Creep Indentation of Human Hip Articular Cartilage: Comparisons of Biphasic Finite Element/Optimization and Semi-Analytical Solutions," ASME Winter Annual Meeting, Anaheim, CA, ASME, 1992.
16. Atluri, S. N., Gallagher, R. H., and Zienkiewicz, O. C., Ed., "Hybrid and Mixed Finite Element Methods," New York, John Wiley and Sons, 1983.
17. Ayari, M. L., and Saouma, V. E., "Static and dynamic contact/impact problems using fictitious forces," *International Journal for Numerical Methods in Engineering*, **32**, pp. 623-543, 1991.
18. Babuska, I., "The finite element method with Lagrange multipliers," *Numerische Mathematik*, **20**, pp. 179-192, 1973.
19. Babuska, I., Oden, J. T., and Lee, J. K., "Mixed-hybrid finite element approximations of second-order elliptic boundary-value problems," *Computer Methods in Applied Mechanics and Engineering*, **11**, pp. 175-206, 1977.
20. Baehmann, P. L., and Shephard, M. S., "Adaptive multiple-level h-refinement in automated finite element analysis," *Engineering with Computers*, **5**, pp. 235-247, 1989.

21. Barata Marques, M. J. M., and Martins, P. A. F., "Three-dimensional finite element contact algorithm for metal forming," *International Journal for Numerical Methods in Engineering*, **30**, pp. 1341-1354, 1990.
22. Barlow, J., "Optimal stress locations in finite element models," *International Journal for Numerical Methods in Engineering*, **10**, pp. 243-251, 1976.
23. Belytschko, T., and Law, S. E., "An assembled surface normal algorithm for interior node removal in three-dimensional finite element meshes," *Engineering with Computers*, **1:1**, pp. 55-60, 1985.
24. Belytschko, T., and Neal, M. O., "Contact-impact by the pinball algorithm with penalty and Lagrangian methods," *International Journal for Numerical Methods in Engineering*, **31**, pp. 547-572, 1991.
25. Biot, M. A., "General theory of three-dimensional consolidation," *Journal of Applied Physics*, **12**, pp. 155-164, 1941.
26. Biot, M. A., and Willis, D. G., "The elastic coefficients of the theory of consolidation," *Journal of Applied Mechanics*, **24**, pp. 594-601, 1957.
27. Blankevoort, L., Kuiper, J., Huiskes, R., and Grootenboer, H., "Articular contact in a three-dimensional model of the knee," *Journal of Biomechanics*, **24:11**, pp. 1019-1032, 1991.
28. Bohatier, C., and Chenot, J.-L., "Finite element formulation for non-steady-state large deformations with sliding or evolving contact boundary conditions," *International Journal for Numerical Methods in Engineering*, **28**, pp. 753-768, 1989.

29. Bowen, R. M., "Theory of mixtures," in *Continuum Physics*, Eringen, A. C., ed., New York, Academic Press, pp. 1-127, 1976.
30. Brown, T. D., and Singerman, R. J., "Experimental determination of the linear biphasic constitutive coefficients of human fetal proximal femoral chondroepiphysis," *Journal of Biomechanics*, **10:8**, pp. 597-605, 1986.
31. Char, B. W., Geddes, K. O., Gonnet, G. H., Monagan, M. B., and Watt, S. M., *MAPLE Reference Manual*, Fifth Edition, Waterloo, Ontario, Canada, Waterloo Maple Publishing, 1990.
32. Charnley, J., "The lubrication of animal joints," Symposium on Biomechanics, Inst. of Mech. Engrs., London, 1959.
33. Cheng, W.-Q., Zhu, F.-W., and Luo, J.-W., "Computational finite element analysis and optimal design for multibody contact systems," *Computer Methods in Applied Mechanics and Engineering*, **71**, pp. 31-39, 1988.
34. Cohen, B., "Anisotropic hydrated soft tissues in finite deformation and the biomechanics of the growth plates," Ph. D. thesis, Department of Mechanical Engineering, Columbia University, 1992.
35. Cohen, B., Gardner, T. R., and Ateshian, G. A., "The influence of transverse isotropy on cartilage indentation behavior -- A study of the human humeral head," in *Transactions Orthopaedic Research Society*, Chicago, ORS, pp. 185, 1993.
36. Craine, R. E., Green, A. E., and Naghdi, P. M., "A mixture of viscous elastic materials with different constituent temperatures," *Quarterly Journal of Mechanics and Applied Mathematics*, **23:2**, pp. 171-184, 1970.

37. Cuthill, E., and McKee, J., "Reducing the bandwidth of sparse symmetric matrices," in *ACM National Conference*, San Fransisco, ACM, pp. 157-172, 1969.
38. Desai, C. S., Zaman, M. M., Lightner, J. G., and Siriwardane, H. J., "Thin-layer element for interfaces and joints," *International Journal for Numerical Methods in Geomechanics*, 8, pp. 19-43, 1984.
39. Donzelli, P. S., Spilker, R. L., Baehmann, P. L., Niu, Q., and Shephard, M. S., "Automated adaptive analysis of the biphasic equations for soft tissue mechanics using a posteriori error indicators," *International Journal for Numerical Methods in Engineering*, 34:3, pp. 1015-1033, 1992.
40. Dowson, D., Unsworth, A., Cooke, A. F., and Gvozdanovic, D., "Lubrication of joints," in *An introduction to the biomechanics of joints and joint replacement*, Dowson, D. and Wright, V., ed., London, Mechanical Engineering Publishers, Ltd., pp. 120-145, 1981.
41. Eberhardt, A. W., Keer, L. M., Lewis, J. L., and Vithoonntien, V., "An analytical model of joint contact," *Journal of Biomechanical Engineering*, 112, pp. 407-413, 1990.
42. Eberhardt, A. W., Lewis, J. L., and Keer, L. M., "Contact of layered elastic spheres as a model of joint contact: Effect of tangential load and Friction," *Journal of Biomechanical Engineering*, 113, pp. 107-108, 1991.
43. Eberhardt, A. W., Lewis, J. L., and Keer, L. M., "Normal contact of elastic spheres with two elastic layers as a model of joint articulation," *Journal of Biomechanical Engineering*, 113, pp. 410-417, 1991.

44. Elmore, S. M., Sokoloff, L., Norris, G., and Carmeci, P., "Nature of imperfect elasticity of articular cartilage," *Journal of Applied Physiology*, 18, pp. 393-396, 1963.
45. Engelman, M. S., Sani, R. L., Gresho, P. M., and Bercovier, M., "Consistent vs. reduced integration penalty methods for incompressible media using several old and new elements.," *International Journal for Numerical Methods in Fluids*, 2, pp. 25-42, 1982.
46. Favenesi, J. A., Shaffer, J. C., and Mow, V. C., "Biphasic mechanical properties of knee meniscus," *Transactions Orthopaedic Research Society*, 8, pp. 57, 1983.
47. Fung, Y. C., "Biomechanics," *Applied Mechanics Reviews*, 21:1, pp. 1-20, 1968.
48. Fung, Y. C., *Biomechanics Mechanical Properties of Living Tissues*, New York, Springer-Verlag, 1981.
49. Gaertner, R., "Investigation of plane elastic contact allowing for friction," *Computers & Structures*, 76, pp. 59-63, 1977.
50. Ghaboussi, J., and Wilson, E. L., "Variational formulation of dynamics of fluid-saturated porous elastic solids," *Journal of the Engineering Mechanics Division Proceedings of the American Society of Civil Engineers*, 98:EM4, pp. 947-963, 1972.
51. Gray, H., and Goss, C. M., *Gray's Anatomy of the Human Body*, 29th American Edition, Philadelphia, Lee & Febiger, 1973.
52. Haftka, R. T., Gurdal, Z., and Kamat, M. P., *Elements of Structural Optimization*, Second Edition, Dordrecht, the Netherlands, Kluwer Academic Publishers, 1990.

53. Hale, J. E., Rudert, M. J., and Brown, T. D., "Indentation assessment of biphasic mechanical property deficits in size-dependent osteochondral defect repair," *Journal of Biomechanics*, **26:11**, pp. 1319-1325, 1993.
54. Hardingham, T. E., Muir, H., Kwan, M. K., Lai, W. M., and Mow, V. C., "Viscoelastic properties of proteoglycan solutions with varying proportions present as aggregates," *Journal of Orthopaedic Research*, **5**, pp. 36-46, 1987.
55. Hayes, W. C., Keer, L. M., Herrmann, G., and Mockros, L. F., "A mathematical analysis for indentation tests of articular cartilage," *Journal of Biomechanics*, **5**, pp. 541-551, 1972.
56. Hayes, W. C., and Mockros, L. F., "Viscoelastic properties of human articular cartilage," *Journal of Applied Physiology*, **31**, pp. 562-568, 1971.
57. Heegaard, J.-H., "Large slip contact in biomechanics: kinematics and stress analysis of the patello-femoral joint," Ph. D. thesis, Department of Physics, Ecole Polytechnique Federale de Lausanne, 1993.
58. Heegaard, J.-H., and Curnier, A., "An augmented lagrangian method for discrete large-slip contact problems," *International Journal for Numerical Methods in Engineering*, **36:4**, pp. 569-593, 1993.
59. Hertz, H., "Über die berührung fester elastischer körper," *J. f. Math. (Crelle)*, **92**, 1881.
60. Hirsch, C., "The pathogenesis of chondromalacia of the patella," *Acta. Chir. Scand.*, **90**, pp. 1-106, 1944.



61. Holmes, M., and Mow, V., "The nonlinear characteristics of soft polyelectrolyte gels and hydrated connective tissues in ultrafiltration," *Journal of Biomechanics*, **23:11**, pp. 1145-1156, 1990.
62. Holmes, M. H., "Finite deformation of soft tissue: Analysis of a mixture model in uni-axial compression," *Journal of Biomechanical Engineering*, **108**, pp. 372-381, 1986.
63. Holmes, M. H., Lai, W. M., and Mow, V. C., "Singular perturbation analysis of the nonlinear, flow-dependent compressive stress-relaxation behavior of articular cartilage," *Journal of Biomechanical Engineering*, **107**, pp. 206-218, 1985.
64. Hou, J. S., Holmes, M. H., Lai, W. M., and Mow, V. C., "Boundary conditions at the cartilage-synovial fluid interface for joint lubrication and theoretical verifications," *Journal of Biomechanical Engineering*, **111:1**, pp. 78-87, 1989.
65. Hou, J. S., Mow, V. C., Lai, W. M., and Holmes, M. H., "Squeeze film lubrication for articular cartilage with synovial fluid," *Journal of Biomechanics*, **25**, pp. 247-259, 1992.
66. Hughes, T. J. R., *The Finite Element Method Linear Static and Dynamic Analysis*, Englewood Cliffs, Prentice-Hall, Inc., 1987.
67. Hughes, T. J. R., Taylor, R. L., Sackman, J., Curnier, A., and Kanoknukulchai, W., "A finite element method for a class of contact impact problems," *Computer Methods in Applied Mechanics and Engineering*, **8**, pp. 249-276, 1976.
68. Huiskes, R., Kremers, J., De Lange, A., Woltring, H. J., Selvik, G., and Van Rens, T. J. G., "Analytical stereophotogrammetric determination of three-

- dimensional knee-joint geometry," *Journal of Biomechanics*, 18:8, pp. 559-570, 1985.
69. IBM Corporation, *IBM Visualization Data Explorer, Users Guide*, Second Edition, Yorktown Heights, NY, IBM Corp., 1992.
  70. Johnson, C., *Numerical Solution of Partial Differential Equations by the Finite Element Method*, Cambridge, Cambridge University Press, 1987.
  71. Johnson, C., "Adaptive finite element methods for diffusion and convection problems," *Computer Methods in Applied Mechanics and Engineering*, 82, pp. 301-322, 1990.
  72. Johnson, K. L., *Contact Mechanics*, New York, Cambridge University Press, 1985.
  73. Kelkar, R., and Ateshian, G. A., "Contact creep response between a rigid impermeable cylinder and a biphasic cartilage layer using integral transforms," in *1995 Bioengineering Conference*, Hochmuth, R. M., Langrana, N. A. and Hefzy, M. S., ed., New York, ASME, 1995.
  74. Kikuchi, N., "A class of rigid punch problems involving forces and moments by reciprocal variational inequalities," *Journal of Structural Mechanics*, 7:3, pp. 273-295, 1979.
  75. Kikuchi, N., and Oden, J. T., *Contact Problems in Elasticity: A Study of Variational Inequalities and Finite Element Methods*, Philadelphia, Society for Industrial and Applied Mathematics, 1988.

76. Kubomura, K., "Solutions of contact problems by the assumed stress hybrid model," PhD thesis, Department of Aeronautics and Astronautics, Massachusetts Institute of Technology, 1979.
77. Kwak, B. M., "Complementary problem formulation of three-dimensional frictional contact," *ASME Journal of Applied Mechanics*, **58**, pp. 134-140, 1991.
78. Kwan, M. K., Lai, W. M., and Mow, V. C., "A finite deformation theory for cartilage and other soft hydrated connective tissues," *Journal of Biomechanics*, **23**, pp. 145-155, 1990.
79. Lai, W. M., Hou, J. S., and Mow, V. C., "A triphasic theory for the swelling and deformational behaviors of articular cartilage," *Journal of Biomechanical Engineering*, **113**:3, pp. 245-258, 1991.
80. Lai, W. M., and Mow, V. C., "Drag-induced compression of articular cartilage during a permeation experiment," *Biorheology*, **17**, pp. 111-123, 1980.
81. Lai, W. M., Mow, V. C., and Roth, V., "Effects of nonlinear strain-dependent permeability and rate of compression on the stress behavior of articular cartilage," *Journal of Biomechanical Engineering*, **103**, pp. 61-66, 1981.
82. Laursen, T. A., and Oancea, V. G., "Automation and assessment of augmented lagrangian algorithms for frictional contact problems," *Journal of Applied Mechanics*, 1995.
83. Laursen, T. A., and Simo, J. C., "A continuum-based finite element formulation for the implicit solution of multibody, large deformation frictional contact

- problems," *International Journal for Numerical Methods in Engineering*, 36:20, pp. 3451-3485, 1993.
84. Lipshitz, H., Etheredge, R., and Glimcher, M. J., "In vitro wear of articular cartilage: I. Hydroxyproline, hexosamine, and amino acid composition of bovine articular cartilage as a function of depth from the surface; hydroxyproline content of the lubricant and the wear debris as a measure of wear," *Journal of Bone and Joint Surgery*, 57A, pp. 527-537, 1975.
  85. Lipshitz, H., and Glimcher, M. J., "In vitro studies of the wear of articular cartilage: II. Characteristics of the wear of articular cartilage when worn against stainless steel plates having characterized surfaces," *Wear*, 52, pp. 297-339, 1979.
  86. Lissner, H. R., "Biomechanics - What is it?," in *Biomechanics Monograph*, Byars, E. F., Contini, R. and Roberts, V. L., ed., New York, ASME, pp. 250, 1967.
  87. Mak, A. F., "The apparent viscoelastic behavior of articular cartilage-The contributions from the intrinsic matrix viscoelasticity and interstitial fluid flows," *Journal of Biomechanical Engineering*, 108, pp. 123-130, 1986.
  88. Mak, A. F., Lai, W. M., and Mow, V. C., "Biphasic indentation of articular cartilage: Part I, theoretical analysis," *Journal of Biomechanics*, 20, pp. 703-714, 1987.
  89. Malcom, L. L., "An experimental investigation of the frictional and deformational response of articular cartilage interfaces to statistic and dynamic loading," Ph.D. thesis, Univ. of California, San Diego, 1976.

90. Malkus, D. S., and Hughes, T. J. R., "Mixed finite element methods - reduced and selective integration techniques: A unification of concepts," *Computer Methods in Applied Mechanics and Engineering*, **15**, pp. 63-81, 1978.
91. Maxian, T. A., "A six-node triangular element for the mixed-penalty finite element formulation of the linear biphasic theory," Master of Science thesis, Department of Mechanical Engineering, Aeronautical Engineering and Mechanics, Rensselaer Polytechnic Institute, 1989.
92. McCutchen, C. W., "The frictional properties of animal joints," *Wear*, **5**, pp. 1-17, 1962.
93. McDevitt, C. A., Gilbertson, E., and Muir, H., "An experimental model of osteoarthritis: early morphological and biochemical changes," *Journal of Bone and Joint Surgery*, **59B**, pp. 24-35, 1977.
94. Moore, P. K., and Flaherty, J. E., "Adaptive local overlapping grid methods for parabolic systems in two space dimensions," *Journal of Computational Physics*, **98**, pp. 54-63, 1992.
95. Mow, V. C., Holmes, M. H., and Lai, W. M., "Fluid transport and mechanical properties of articular cartilage: A review," *Journal of Biomechanics*, **17**, pp. 377-394, 1984.
96. Mow, V. C., Kuei, S. C., Lai, W. M., and Armstrong, C. G., "Biphasic creep and stress relaxation of articular cartilage in compression: theory and experiments," *Journal of Biomechanical Engineering*, **102**, pp. 73-84, 1980.

97. Mow, V. C., Kwan, M. K., Lai, W. M., and Holmes, M. H., "A finite deformation theory for nonlinearly permeable cartilage and other soft hydrated connective tissues," in *Frontiers in Biomechanics*, Woo, S. L.-Y., Schmid-Schonbein, G. and Zweifach, B., ed., New York, Springer-Verlag, pp. 153-179, 1986.
98. Mow, V. C., and Lai, W. M., "Mechanics of animal joints," in *Annual review of fluid mechanics*, Van Dyke, M., ed., Palo Alto, Annual review, Inc., pp. 247-288, 1979.
99. Mow, V. C., and Lai, W. M., "Recent development in synovial joint biomechanics," *SIAM Review*, **22:3**, pp. 275-317, 1980.
100. Mow, V. C., Lai, W. M., and Redler, I., "Some surface characteristics of articular cartilage. I: A scanning electron microscopy study and a theoretical model for the dynamic interaction of synovial fluid and articular cartilage," *Journal of Biomechanics*, **7**, pp. 449-456, 1974.
101. Mow, V. C., Ratcliffe, A., Chern, K. Y., and Kelly, M. A., "Structure and function relationships of the menisci of the knee," in *Knee Meniscus: Basic and Clinical Foundations*, Mow, V. C., Arnoczky, S. P. and Jackson, D. W., ed., New York, Raven Press, pp. 37-57, 1992.
102. Mow, V. C., Setton, L. A., Howell, D. S., and Buckwalter, J. A., "Structure-function relationship of articular cartilage and the effect of joint instability and trauma on cartilage function," in *Cartilage Changes in Osteoarthritis*, Brandt, K. D., ed., Indianapolis IN, University of Indiana Press, pp. 22-42, 1990.

103. Muir, H., "Proteoglycans as organizers of the extracellular matrix," *Biochemistry Society Transactions*, 11, pp. 613-622, 1983.
104. Murad, M. A., and Loula, A. F. D., "Improved accuracy in finite element analysis of Biot's consolidation problem," *Computer Methods in Applied Mechanics and Engineering*, 95:3, pp. 359-382, 1992.
105. Murad, M. A., and Loula, A. F. D., "On stability and convergence of finite element approximations of Biot's consolidation problem," *International Journal for Numerical Methods in Engineering*, 37:4, pp. 645-667, 1994.
106. Noor, A. K., "Multifield (mixed and hybrid) finite element models," in *State-of-the art Surveys on Finite Element Technology*, Noor, A. K. and Pilkey, ed., ASME, AMD, pp. 127-162, 1983.
107. Oden, J. T., and Brauchli, H. J., "On the calculation of consistent stress distributions in finite element approximations," *International Journal for Numerical Methods in Engineering*, 3, pp. 317-325, 1971.
108. Oden, J. T., and Kikuchi, H., "Finite element methods for constrained problems in elasticity," *International Journal for Numerical Methods in Engineering*, 18:5, pp. 701-725, 1982.
109. Oden, J. T., Kikuchi, N., and Song, Y. J., "Penalty-finite element methods for the analysis of Stokesian flows," *Computer Methods in Applied Mechanics and Engineering*, 31, pp. 297-329, 1982.

110. Oden, J. T., and Lee, J. K., "Theory of mixed and hybrid finite-element approximations in linear elasticity," in *Lecture Notes in Mathematics*, Dold, A. and Eckmann, B., ed., Springer-Verlag, 1975.
111. Oomens, C. W. J., and Van Campen, D. H., "In vitro compression of a soft tissue layer on a rigid foundation," *Journal of Biomechanics*, **20:10**, pp. 923-935, 1987.
112. Oomens, C. W. J., Van Campen, D. H., and Grootenboer, H. J., "A mixture approach to the mechanics of skin," *Journal of Biomechanics*, **20:9**, pp. 877-885, 1987.
113. Pian, T. H. H., "Derivation of element stiffness matrices by assumed stress distribution," *ALAA Journal*, **2:7**, pp. 1333-1336, 1964.
114. Pian, T. H. H., and Lee, S. W., "Notes on finite elements for nearly incompressible materials," *Journal of the American Institute for Aeronautics and Astronautics*, **14:6**, pp. 824-826, 1976.
115. Prevost, J. H., "Mechanics of continuous porous media," *International Journal of Engineering Science*, **18**, pp. 787-800, 1980.
116. Prevost, J. H., "Nonlinear transient phenomena in saturated porous media," *Computer Methods in Applied Mechanics and Engineering*, **20**, pp. 3-18, 1982.
117. Proctor, C. S., Schmidt, M. B., Whipple, R. R., Kelly, M. A., and Mow, V. C., "Material properties of the normal medial bovine meniscus," *Journal of Orthopaedic Research*, **7**, pp. 71-82, 1989.



118. Schreppers, G. J. M. A., Sauren, A. A. H. J., and Huson, A., "A numerical model of the load transmission in the tibio-femoral contact area," *Journal of Engineering in Medicine, Proc. Instn. Mech. Engrs.*, **204**, pp. 53-59, 1990.
119. Setton, L. A., Zhu, W. B., and Mow, V. C., "The biphasic poroviscoelastic behavior of articular cartilage: Role of the surface zone in governing the compressive behavior," *Journal of Biomechanics*, **26**, pp. 581-592, 1993.
120. Shephard, M. S., "Finite element modeling within an integrated geometric modeling environment: part 1 - mesh generation," *Engineering with Computers*, **1**, pp. 61-71, 1985.
121. Shephard, M. S., "The specification of physical attribute information for engineering analysis," *Engineering with Computers*, **4**, pp. 145-155, 1988.
122. Shephard, M. S., and Georges, M. K., "Automatic three-dimensional mesh generation by the finite octree technique," *International Journal for Numerical Methods in Engineering*, **32**, pp. 709-739, 1991.
123. Shephard, M. S., and Georges, M. K., "Reliability of automatic 3-D mesh generation," *Computer Methods in Applied Mechanics and Engineering*, **101**, pp. 443-462, 1992.
124. Shrive, N. G., Wilson, A. N., Van der Voet, F., Simbeya, H. W., Frank, C. B., and Schachar, N. S., "Micromechanical modelling of soft tissues using the finite element method," in *1993 Bioengineering Conference*, Langrana, N. A., Friedman, M. H. and Grood, E. S., ed., New York, ASME, pp. 642-645, 1993.

125. Simo, J. C., and Laursen, T. A., "An augmented Lagrangian treatment of contact problems involving friction," *Computers & Structures*, **42:1**, pp. 97-116, 1992.
126. Simo, J. C., Wriggers, P., and Taylor, R. L., "A perturbed Lagrangian formulation for the finite element solution of contact problems," *Computer Methods in Applied Mechanics and Engineering*, **50:2**, pp. 163-180, 1985.
127. Simon, B. R., and Gaballa, M., "Poroelastic finite element models for the spinal motion segment including ionic swelling," in *Computational methods in bioengineering*, Spilker, R. L. and Simon, B. R., ed., ASME, 1988.
128. Simon, B. R., Wu, J. S. S., Carlton, M. W., France, E. P., Evans, J. H., and Kazarian, L. E., "Structural models for human spinal motion segments based on a poroelastic view of the intervertebral disk.," *Journal of Biomechanical Engineering*, **107**, pp. 327-335, 1985.
129. Simon, B. R., Wu, J. S. S., and Zienkiewicz, O. C., "Evaluation of higher order, mixed, and hermitean finite element procedures for the dynamic analysis of saturated porous media using one-dimensional models," *International Journal for Numerical and Analytical Methods in Geomechanics*, **10**, pp. 461-482, 1986.
130. Simon, B. R., Wu, J. S. S., Zienkiewicz, O. C., and Paul, D. K., "Evaluation of U-W and U-P finite element methods for the dynamic response of saturated porous media using one-dimensional models," *International Journal for Numerical and Analytical Methods in Geomechanics*, **10**, pp. 483-499, 1986.

131. Simon, B. R., Zienkiewicz, O. C., and Paul, D. K., "An analytical solution for the transient response of saturated porous elastic solids," *International Journal for Numerical and Analytical Methods in Geomechanics*, 8, pp. 381-398, 1984.
132. Sokoloff, L., "Elasticity of aging cartilage," *Fed. Proc., Fed. Am. Soc. Exp. Biol.*, 25, pp. 1089-1095, 1966.
133. Soslowsky, L. J., "Studies on diarthrodial joint biomechanics with special reference to the shoulder," Ph. D. thesis, Department of Mechanical Engineering, Columbia University, 1991.
134. Soslowsky, L. J., Ateshian, G. A., and Mow, V. C., "Stereophotogrammetric determination of joint anatomy and contact areas," in *Biomechanics of Diarthrodial Joints*, Mow, V. C., Ratcliffe, T. A. and L-Y.Woo, S., ed., Springer-Verlag, pp. 243-268, 1990.
135. Soslowsky, L. J., Flatow, E. L., Bigliani, L. U., Pawluk, R. J., Ateshian, G. A., and Mow, V. C., "Quantitation of in situ contact areas at the glenohumeral joint: A biomechanical study," *Journal of Orthopaedic Research*, 10, pp. 524-534, 1992.
136. Spigle, M. R., *Mathematical Handbook of Formulas and Tables*, New York, McGraw-Hill, 1968.
137. Spilker, R. L., Almeida, E. S., Clutz, C., Shephard, M. S., Ateshian, G. A., and Donzelli, P. S., "Three dimensional automated biphasic finite element analysis of soft tissues from stereophotogrammetric data," in *1993 Advances in Bioengineering*, Tarbell, J. M., ed., New York, ASME, pp. 15-18, 1993.

138. Spilker, R. L., Donzelli, P. S., and Mow, V. C., "A transversely isotropic biphasic finite element model of the meniscus," *Journal of Biomechanics*, **25:9**, pp. 1027-1045, 1992.
139. Spilker, R. L., and Maxian, T. A., "A mixed-penalty finite element formulation of the linear biphasic theory for soft tissues," *International Journal for Numerical Methods in Engineering*, **30**, pp. 1063-1082, 1990.
140. Spilker, R. L., and Reed, K. W., Ed., "Hybrid and Mixed Finite Element Methods," New York, ASME, 1985.
141. Spilker, R. L., Shephard, M. S., Ateshian, G. A., Mow, V. C., Almeida, E. S., Donzelli, P. S., and Clutz, C. J., "Simulating the 3D biphasic response of soft tissues in diarthrodial joints using physiological data," in *Second World Congress of Biomechanics*, Blankevoort, L. and Kooloos, J. G. M., ed., Nijmegen, Stichting World Biomechanics, pp. 212, 1994.
142. Spilker, R. L., and Suh, J.-K., "Formulation and evaluation of a finite element model of soft hydrated tissue," *Computers and Structures*, **35:4**, pp. 425-439, 1990.
143. Spilker, R. L., Suh, J.-K., and Mow, V. C., "A finite element formulation of the linear biphasic representation of soft tissues," in *1987 Biomechanics Symposium*, Butler, D. L. and Torzilli, P. A., ed., New York, ASME, pp. 49-50, 1987.
144. Strang, G., and Fix, G. J., *An Analysis of the Finite Element Method*, Englewood Cliffs, NJ, Prentice-Hall, 1973.
145. Suh, J.-K., "A finite element formulation for nonlinear behavior of biphasic hydrated soft tissue under finite deformation," Ph.D. thesis, Department of

Mechanical Engineering, Aeronautical Engineering and Mechanics, Rensselaer Polytechnic Institute. 1989.

146. Suh, J.-K., Spilker, R. L., and Holmes, M. H., "A penalty finite element analysis for nonlinear mechanics of biphasic hydrated soft tissue under large deformation," *International Journal for Numerical Methods in Engineering*, **32**, pp. 1411-1439, 1991.
147. Takahashi, S., and Brebbia, C. A., "Validation of the boundary element flexibility approach for elastic contact analysis," *Computer Methods in Applied Mechanics and Engineering*, **93**, pp. 151-168, 1991.
148. Tissakht, M., Marchand, F., and Ahmed, A. M., "Non-linear finite element analysis of the knee menisci: a composite fiber-reinforced model," in *Transactions, 37th Orthopaedic Research Society Meeting*, pp. 294, 1991.
149. Tissakht, M., and Ahmed, A. M., "Effect of tibial axial rotation on knee meniscal stress: a finite element study," in *Transactions, 36th Orthopaedic Research Society*, pp. 243, 1990.
150. Tissakht, M., and Ahmed, A. M., "Parametric Study Using Different Elastic and Poroelastic Axisymmetric Models of the Femur-Meniscus-Tibia Unit," ASME Winter Annual Meeting, Anaheim, CA, ASME, 1992.
151. Torzilli, P. A., and Mow, V. C., "On the fundamental fluid transport mechanisms through normal and pathatlogical articular cartilage during function, I," *Journal of Biomechanics*, **9**, pp. 541-552, 1976.

152. Torzilli, P. A., and Mow, V. C., "On the fundamental fluid transport mechanisms through normal and pathatlogical articular cartilage during function, II," *Journal of Biomechanics*, 9, pp. 587-606, 1976.
153. Truesdell, C., and Noll, W., *The Non-linear Field Theories of Mechanics*, second Edition, Berlin, Springer-Verlag, 1992.
154. Tseng, J., and Olson, M. D., "The mixed finite element method applied to two-dimensional elastic contact problems," *International Journal for Numerical Methods in Engineering*, 17, pp. 991-1014, 1981.
155. Vermilyea, M. E., "A hybrid finite element formulation for linear biphasic 3-D analysis of soft hydrated tissue," Ph.D. thesis, Department of Mechanical Engineering, Aeronautical Engineering and Mechanics, Rensselaer Polytechnic Institute, 1990.
156. Vermilyea, M. E., and Spilker, R. L., "A hybrid finite element formulation of the linear biphasic equations for soft hydrated tissues," *International Journal for Numerical Methods in Engineering*, 33, pp. 567-594, 1992.
157. Vermilyea, M. E., and Spilker, R. L., "Hybrid and mixed-penalty finite elements for 3D analysis of soft hydrated tissue," *International Journal for Numerical Methods in Engineering*, 36, pp. 4223-4243, 1993.
158. Vijayakar, S., "A combined surface integral and finite element solution for a three-dimensional contact problem," *International Journal for Numerical Methods in Engineering*, 31, pp. 525-545, 1991.

159. Wayne, J. S., Woo, S. L.-Y., and Kwan, M. K., "Application of the u-P finite element method to the study of articular cartilage," *Journal of Biomechanical Engineering*, 113:4, pp. 397-403, 1991.
160. Weiler, K. J., "Topological structures for geometric modeling," PhD thesis, Department of Computer and Systems Engineering, Rensselaer Polytechnic Institute, 1986.
161. Weiss, J. A., Maker, B. N., and Greenwald, R. M., "Finite element implementation of incompressible, transversely isotropic hyperelasticity," in *Advances in Bioengineering 1994*, Askew, M. J., ed., New York, ASME, pp. 137-138, 1994.
162. Woo, S. L.-Y., Akeson, W. H., and Jemmott, G. F., "Measurements of nonhomogeneous, directional mechanical properties of articular cartilage in tension," *Journal of Biomechanics*, 9, pp. 785-791, 1976.
163. Woo, S. L.-Y., Simon, B. R., Kuei, S. C., and Akeson, W. H., "Quasi-linear viscoelastic properties of normal articular cartilage," *Journal of Biomechanical Engineering*, 102, pp. 85-90, 1980.
164. Wriggers, P., Van, T. V., and Stien, E., "Finite element formulation of large deformation impact-contact problems with friction," *Computers & Structures*, 37:3, pp. 319-331, 1990.
165. Zienkiewicz, O. C., and Taylor, R. L., *The Finite Element Method*, Vol. I, Fourth Edition, London, McGraw-Hill Book Company, 1989.

166. Zienkiewicz, O. C., and Zhu, J. Z., "The superconvergent patch recovery and a posteriori error estimates: I The recovery technique," *International Journal for Numerical Methods in Engineering*, **33**, pp. 1331-1364, 1992.



## Appendix A: Implicit Time Integration

In Chapter IV the generalized trapezoidal rule was used to integrate the semi-discretized finite element equations in time. The integration rule, Eq. (4.22), is repeated here for reference,

$$\mathbf{u} = \hat{\mathbf{u}} + \Delta t (1-\omega) \hat{\mathbf{v}} + \Delta t \omega \mathbf{v}. \quad (\text{A.1})$$

The integration parameter,  $\omega$ , is chosen in the range zero to one. A value of zero gives an explicit scheme; any other value produces an implicit scheme. When the parameter  $\omega$  is chosen to be 0.5, the method is Crank-Nicolson, and is second order accurate in time. Values of  $\omega$  greater than 0.5 produce schemes stable for any size time step. This choice reduces the time accuracy to only first order, however. Chapter eight of the text by Hughes [66] gives a complete analysis of this differencing method. For reasons of accuracy, then, it is desirable to use the Crank-Nicolson formula whenever possible. There are two cases where it is prudent to choose  $\omega$  other than 0.5: models where forces are prescribed, and cases with evolving contact.

In modeling a creep problem with the biphasic finite element codes, one often finds temporal oscillations of the primary variables. Referring again to Hughes, a modal analysis can be used to determine the stability of the time integration. The result is that the amplification factor for the scheme is the limit of a sequence indexed by time step. Figure A.1 shows this limit for various values of the integration parameter. This amplification factor is a function of both the time step and the eigenvalues of the assembled equations. Schemes for which the magnitude of the amplification factor is less than one are stable. In addition, those for which the amplification factor is positive are non-oscillatory. The fully implicit integration,  $\omega = 1$ , does not oscillate. Other choices of  $\omega$  will have some modes

which oscillate with decreasing amplitude in time. It is apparent from the figure that increasing the integration factor has the effect of increasing the numerical damping, and decreasing any oscillations.

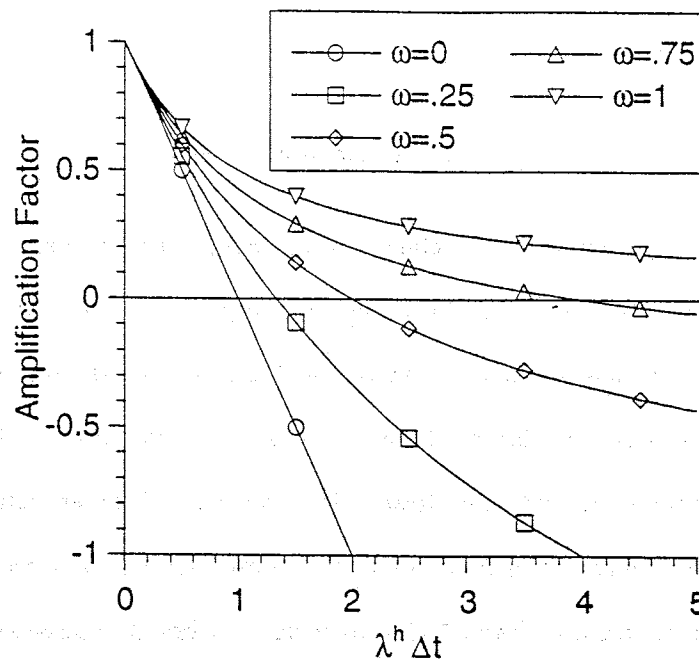


Fig. A.1. Amplification factor for the generalized trapezoidal rule for various values of the integration parameter,  $\omega$  (reproduced from [66]).

While it may be present, this oscillatory behaviour typically does not manifest itself for prescribed displacement boundary conditions. Several possibilities exist to improve the solution for creep problems. The most obvious is to choose a fully implicit integration, which will eliminate the oscillations, but revert the scheme to first order accuracy in time. A second option is to employ smaller time steps in the Crank-Nicolson scheme, which reduces the number of modes which contain an oscillatory component. For many examples, this limit on time step is too restrictive and adds considerably to the computational cost. An attractive approach would be dynamic modification of the time step

and/or the integration factor. This would allow the solution to proceed with second order accuracy where possible, but revert to first order if oscillations occur. Unfortunately, for the linear form of the biphasic finite element equations, this requires that the coefficient matrices be refactored during the solution stage. The effects of either storing these matrices or recomputing them would be quite costly.

For evolving contact, a separate difficulty arises. The kinematic contact boundary conditions, Eqns. (2.40a,b) are written in terms of displacement and reference position. This produces the necessary force terms to bring into contact points which were initially separated, and is required because of the possibility of material overlap and the positive tolerance parameter in the contact evaluation, Eq. (5.3). In the present formulation, displacement in the semi-discretized finite element equations, Eq. (4.20), is related to velocity by Eq. (A.1), leaving a system of equations written only in terms of velocity. Thus, when using a Lagrange multiplier approach, the effect of this boundary condition is to generate velocities which will bring points on opposing surfaces precisely into contact. These velocities, however, will not in general satisfy the conditions implied by the time derivatives of the kinematic boundary conditions. Recall from Chapter II that it is the corresponding velocity conditions that arise from first principles.

A simple example both illustrates this contradiction and offers a solution. Consider a rigid triangular body with a prescribed displacement at its top surface, as illustrated by Fig. A.2a. At the initial time, let it be in point contact with a deformable surface. As time progresses, assume that the deformable surface exactly conforms to the rigid body, but does not deform outside of the region of contact. This does not represent a solution to the equations of elastic equilibrium, but is analogous to the response dictated within the region of contact by the time-discretized form of the Lagrange multiplier contact

formulation. Physically one expects that the instant points come into contact they will have different velocities, but after that they will both have the constant velocity of the rigid body.

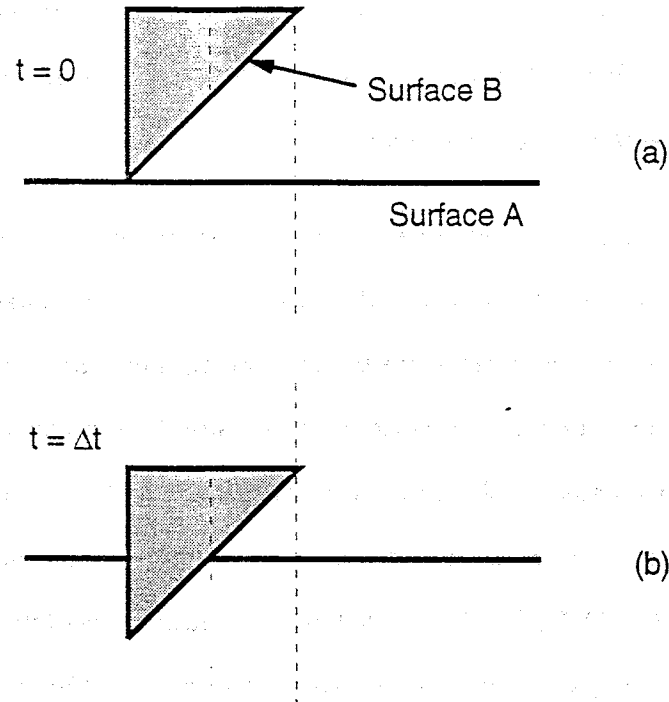


Fig. A.2. Illustration of a rigid block under displacement control penetrating a deformable surface.

The displacement of the rigid block is prescribed as a function of time, thus the velocity can also be calculated,

$$u^B(x,t) = -t, \quad (\text{A.2a})$$

$$v^B(x,t) = -1. \quad (\text{A.2b})$$

Using the assumptions above, the displacement and velocity of surface 'A' can be calculated,

$$u^A(x,t) = \begin{cases} x-t & 0 < x < t \\ 0 & x > t \end{cases}, \quad (\text{A.3a})$$

$$v^A(x,t) = \begin{cases} -1 & 0 < x < t \\ 0 & x > t \end{cases} \quad (\text{A.3b})$$

Now, with the knowledge that the biphasic contact equations will produce the correct surface deformation, let the displacement of surface 'A' follow Eq. (A.3a) and calculate the velocities from Eq. (A.1). At the first time step the velocity of surface 'A' will be

$$v^A(x,\Delta t) = \begin{cases} \frac{1}{\omega} \left( \frac{x}{\Delta t} - 1 \right) & 0 < x < \Delta t \\ 0 & x > \Delta t \end{cases}, \quad (\text{A.4})$$

where the values at the previous time step are taken as zero. Advancing to the second time step,

$$v^A(x,2\Delta t) = \begin{cases} \frac{1}{\omega} \left[ -1 - \left( \frac{1-\omega}{\omega} \right) \left( \frac{x}{\Delta t} - 1 \right) \right] & 0 < x < \Delta t \\ \frac{1}{\omega} \left( \frac{x}{\Delta t} - 2 \right) & \Delta t < x < 2\Delta t \\ 0 & x > 2\Delta t \end{cases} \quad (\text{A.5})$$

Examining Eq. (A.5) for  $\omega = 0.5$  illustrates how Crank-Nicolson gives undesirable results for the contact problem. As depicted in Fig. A.3, in the first spatial increment,  $0 < x < \Delta t$ , the velocity varies linearly from 0 to -2, then in the second increment, from -2 back to 0. Alternatively, when fully implicit integration is used,  $\omega = 1$ , the first increment has an uniform velocity of -1 and in the second increment it varies from -1 to 0. For later times, implicit integration continues this trend; each spatial increment has an uniform velocity of -1, except the last which varies linearly from -1 to 0. This can be interpreted as points in persistent contact having the correct velocity, but those which have come into contact in the present time step being assigned their average velocity during that time step. Thus, using a fully implicit integration with the contact equations produces a solution which more closely approximates both the displacement and velocity forms of the kinematic continuity relations.

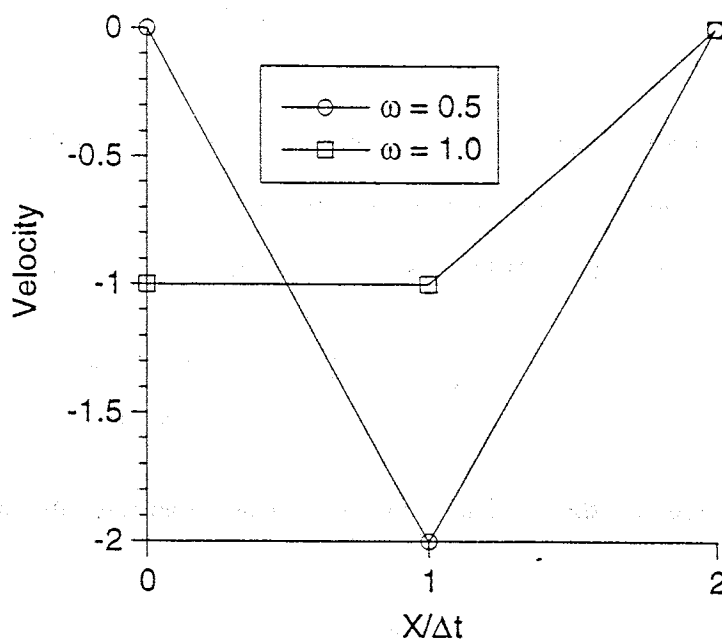
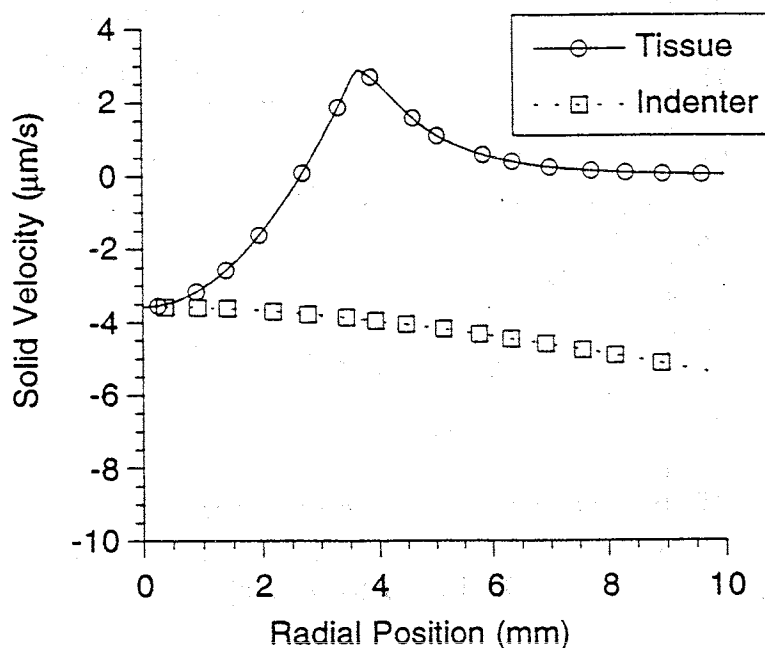


Fig. A.3. Velocity along surface A (Eq. (A.5)) for different values of the integration parameter.

The same conclusion can be reached by a different argument. When the integration parameter is set to one, the difference equation predicts that velocity is dependent only on the displacement history, and not the previous velocities. Since the contact formulation always produces the desired displacements on the contact surface, an implicit integration will produce velocities which are in agreement with the time history of the surface. In the finite element program this implies that points which were in contact at the last time step, and which remain in contact in this time step, will possess the correct continuity of velocity across the contact surface. Points added to the contact surface in the current time step, however, will not be required to have this velocity continuity. Physically, this is reasonable, since at the instant of impact, points must have different velocity.

This behaviour has been verified in the finite element code. As a demonstration, the biphasic indentation example from Chapter VI will be solved with the time integration parameter set to 0.5 and 1, respectively. Values of the normal components of solid velocity on the contact surface are presented in Fig A.4. Part (a) of the figure is given as a reference and depicts the solid velocity after the first time step for the fully implicit integration. Both methods of integration give the correct deformed configuration and stress distribution at this time. Observe that the contact radius is nearly 4mm, but that the velocities are different. Part (b) of the figure shows the same data after the second time step, and part (c) shows data after the second time step for Crank-Nicolson integration. Observe in (b) that the solid velocities are the same over the region that was in contact during the first time step, but that in (c) the results are completely non-physical.



(a)

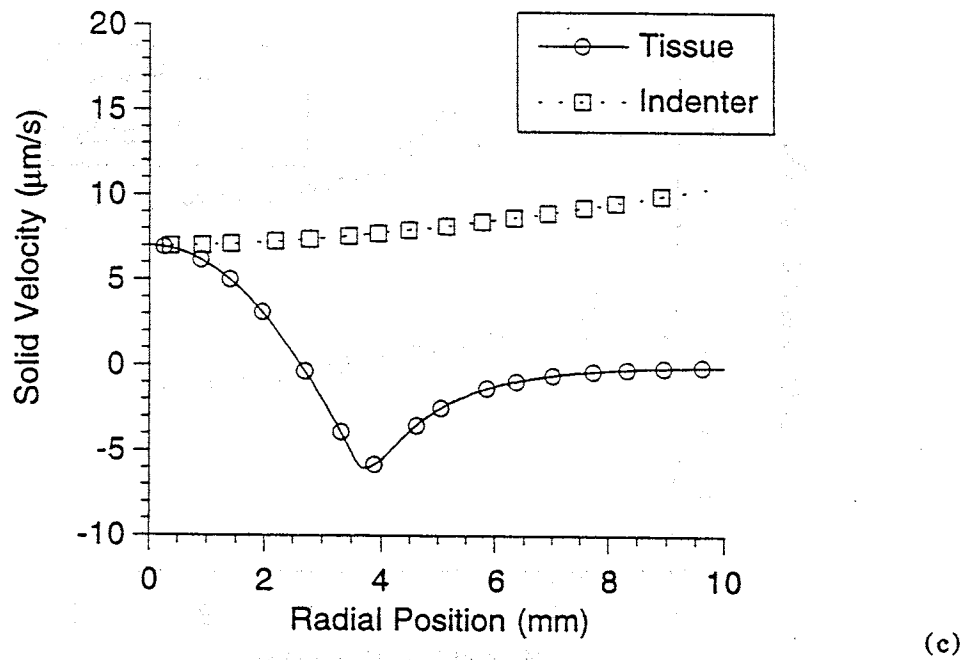
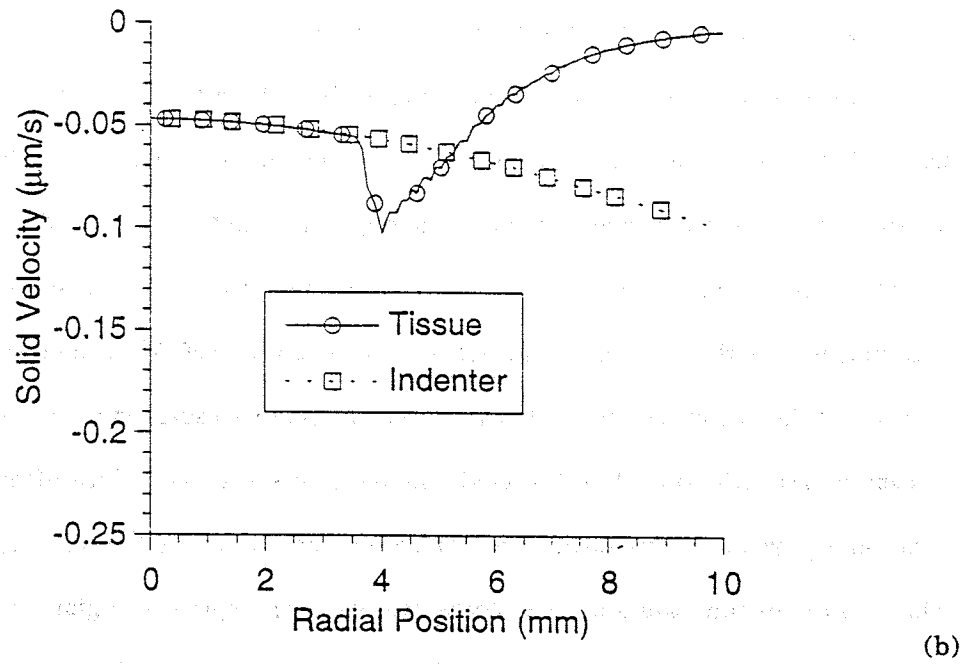


Fig. A.4. Normal solid velocity along the contact surface for the biphasic indentation problem: (a)  $t = \Delta t$ ,  $\omega = 1.0$ , (b)  $t = 2\Delta t$ ,  $\omega = 1.0$ , (c)  $t = 2\Delta t$ ,  $\omega = 0.5$ .



Similar results are obtained for later time steps, and for the fluid velocity. The solution with Crank-Nicolson integration will rapidly break down, however, because the non-physical velocities affect the pressure. Poor pressure in turn affects the stress and then the algorithm for releasing contact points. For the present choice of a family of time integrators, then, the biphasic contact finite element is limited to first order accuracy in time. In the future it may be possible to develop a second order accurate rule using only the displacement history, though this would undoubtedly be a multi-step rule and would entail greater storage requirements. If this element were coupled with a  $p$ -adaptive scheme for the spatial discretization, this issue becomes more significant, as even higher order accurate time integrators are required.



## Appendix B: Symbolic Elastic Contact Calculations

An important consideration in the performance of the contact element is the multipliers ( $\lambda^S$  and  $\lambda^F$ ), Eqns. (4.2-3), defined when constructing the weighted residual form of the problem. These are defined in such a way that one should recover  $C^0$  definitions of the solid and fluid interface tractions. Ideally, this could then be used as the criteria for release in the discretization algorithm. This is not true in all cases. When the contactor and target segments are aligned node-to-node, the multipliers do coincide with the finite element tractions. When there is no correspondence between the contactor and target nodes (as in most evolving contact meshes), or when there are extreme gradients in traction on the contact surface, one cannot rely on the interface traction variables to adequately represent the true traction. This observation in no way appears to limit the applicability of the biphasic contact element.

To further investigate this phenomena, the symbolic computation program MAPLE [31] was used for simplified finite element contact problems. Tests were performed with the three- and six-node triangular elasticity elements in MAPLE. A rectangular geometry one unit by two units was analyzed for both uniform and linearly varying displacements on the top surface. The meshes are given in Fig. B.1, where the node-to-node mesh depicts the uniform displacement and the node-to-element mesh depicts the linear displacement. A contact surface is placed at the half-height of the mesh. All of the x-degrees of freedom were constrained, and Poisson's ratio was zero.

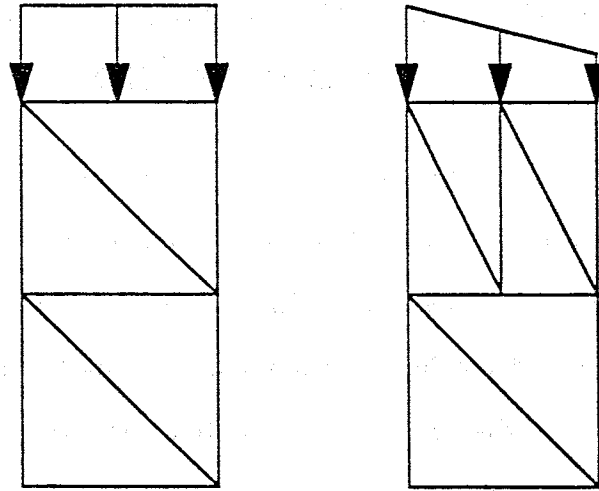


Fig. B.1. Node-to-node (left) and node-to-element (right) meshes used in MAPLE testing of contact elements.

MAPLE has the advantage of performing exact integrals for the element matrices, and can exactly solve the resulting global system of equations. This problem also provides an independent test of the contact formulation. The same methodology was used in deriving the finite element equations, and the contact matrix for elastic contact is equivalent to one quadrant of that for biphasic contact. The same meshes can be used for the biphasic finite element program, and direct comparisons can be made between terms in the contact matrices. A two-node contact element is used in conjunction with the linear triangle, and the three-node contact element with the quadratic triangle, which follows from the discussion of contact interpolations in Chapter IV.

Six problems were solved with the uniform displacement; three each with the three- and six-node elements. One expects a uniform stress in the material, and a displacement that varies linearly through the thickness. For the node-to-node mesh the problem is solved with the three- and six-node elements with and without contact, each time recovering the expected solution. For the node-to-element mesh only the contact solution is possible, and it

too recovers the exact answer for each element. For the cases solved with the contact elements, the values of the degrees of freedom corresponding to the Lagrange multipliers were exactly equal to the uniform stress in the material. Values for the displacement degrees of freedom all had the same value on the contact surface. An additional perturbation was made in the node-to-element mesh. In Fig. B.1 the top pairs of elements each have side lengths equal to one half on the contact surface. To examine the effect of disproportionately small contact elements, their lengths were made  $\frac{1}{100}$  and  $\frac{99}{100}$ . The exact solution is still obtained for all quantities, and no change in the Lagrange multipliers is observed.

The same six problems are solved for the linearly varying applied displacement. In the node-to-node mesh without contact the solutions are linear in the x-direction, as expected. While the solutions from the three- and six-node elements are not identical, it appears that the quadratic solution is a refinement of the linear solution. When this problem is solved with the contact elements, the kinematic and kinetic solutions are equal to the respective non-contact solutions. On the contact surface the expected kinematic continuity is exactly satisfied. Figure B.2 shows the normal (vertical) component of stress on the contact surface, compared with the multipliers for the node-to-node mesh of six-node elements; side 'A' is on the bottom of the geometry in Fig. B.1. The finite element stress is plotted two ways. First as the linear variation in the one element whose edge is on the contact surface, and second as the nodal averaged value of elements which share nodes on the contact surface. The multiplier is plotted as a straight line through its nodal values, even though it is quadratic. This variation in tractions from side 'A' to side 'B' exists even though the displacements possess the correct continuity on the contact surface.

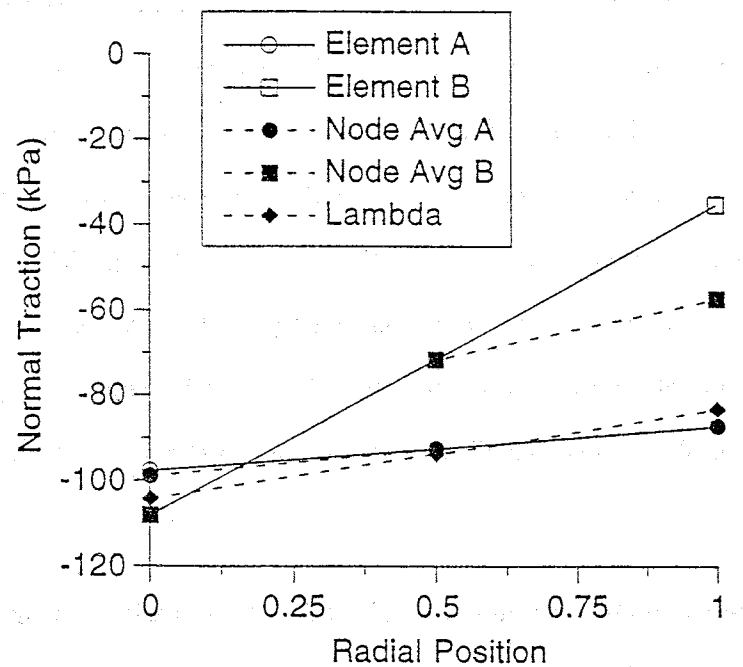


Fig. B.2. Normal tractions and Lagrange multipliers for a linearly varying displacement applied to the node-to-node mesh of six-node triangles.

For the node-to-element mesh there are similar observations. For both the three- and six-node elements, the solution is a refinement over the node-to-node mesh, as expected because of the greater number of degrees of freedom. Again the correct kinematic continuity is enforced across the contact surface. Figure B.3 is a result analogous to that in Fig. B.2. Here the finite element stresses are in better agreement across the contact surface (especially the nodal averaged values), but the multipliers show significant variations. Remember that the Lagrange multipliers are quadratic, but plotted as piecewise linear, so the variation may be more extreme.

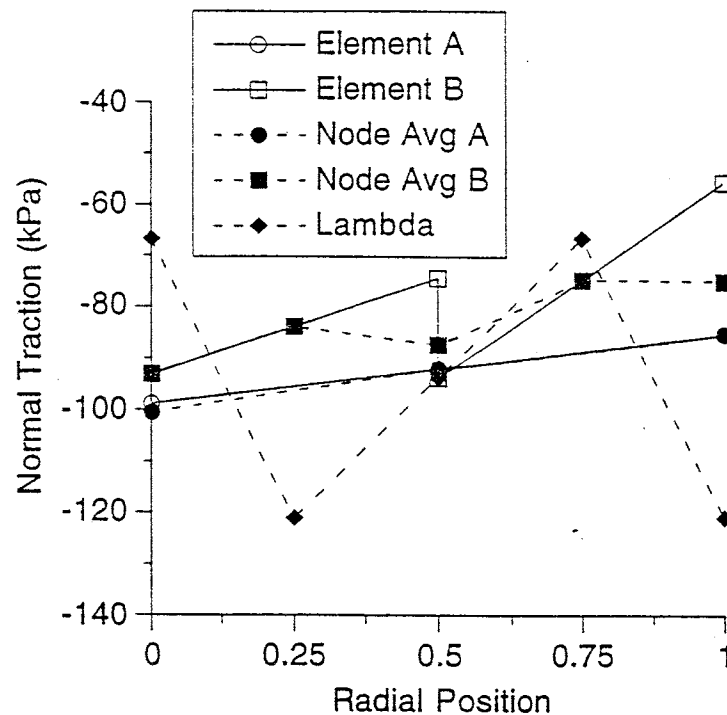


Fig. B.3. Normal tractions and Lagrange multipliers for a linear displacement applied to the node-to-element mesh of six-node triangles.

These results are in agreement with the assessments made in Chapter IV, that a quadratic interpolation for the multipliers will exactly enforce the kinematic constraint, but will allow some violation of the traction continuity. Results presented for the biphasic element in Chapter VI show that with more refined meshes, there is greater agreement between the tractions on either side of the contact surface. In addition, the multiplier approximates this traction more closely than in this simple example. Pointwise, though, there are locations where the approximation is poor, particularly the boundary between active and inactive contact segments. This is not a serious difficulty, as the finite elements tractions are always well behaved. It is these values that are used in the contact iterations to assess the release condition.

